Doctoral Dissertation

Experimental and theoretical investigations on the surface-enhanced Raman spectra of lanthanide-citrate complexes

Hao Jin

Supervisor: Yuko S. Yamamoto

Division of Advanced Science and Technology

Japan Advanced Institute of Science and Technology

Doctor of Philosophy in Materials Science

September 2025

Abstract

The works of this thesis present a series of studies focusing on the surface-enhanced Raman spectroscopy (SERS) measurement, spectral analysis, and density functional theory (DFT)-based SERS simulation of lanthanide (Ln)–citrate complexes. Due to their unique 4f electronic configurations, Ln^{3+} ions exhibit exceptional physical properties, such as luminescence and magnetism. Thus, they are important in functional material field. However, their chemical properties remain extremely similar, making their identification and classification challenging. This difficulty highlights the need for advanced spectroscopic techniques, which forms the core motivation of this thesis.

To address this issue, a stable SERS measurement method was first developed using citrate capped silver nanoparticles (citrate@AgNPs), enabling the detection of Ln-citrate complexes at concentrations as low as 10^{-4} M. Simultaneously, we optimized a DFT-based approach for simulating SERS spectra and assigning vibrational modes. Using this integrated method, we systematically studied the SERS spectral features of seven representative Ln-citrate complexes (Ln = La, Ce, Pr, Nd, Sm, Eu, Gd) and proposed possible mechanisms for the observed spectral variations. To our knowledge, this is the first systematic SERS investigation of Ln-molecular complexes.

In the initial study, La-citrate and Gd–citrate complexes were measured and compared. Although both exhibited similar SERS peak positions, The relative intensities of peaks around 1065, 1315 and 1495 cm^{-1} were differed significantly. DFT simulations revealed that these SERS signals from vibrational modes localized in the coordination region. The intensity ratio of the peaks around 1065 and 1315 cm^{-1}

(I_{1065}/I_{1315}) was found to be approximately 1 for La^{3+} and around 0.55 for Gd^{3+}, providing a qualitative means of distinguishing the two ions.

Further, the SERS spectra of all seven Ln-citrate complexes (Ln = La, Ce, Pr, Nd, Sm, Eu, Gd) were collected under 488, 532, and 660 nm excitations. All showed three prominent peaks near 1065, 1315, and 1485 cm^{-1}. The intensity ratios I_{1065}/I_{1315} and I_{1485}/I_{1315} varied systematically with the Ln^{3+} species, but remained nearly constant across excitation wavelengths. DFT results indicated that as the number of unpaired 4f electrons increases, the attraction between Ln^{3+} and oxygen strengthens, reducing the dipole moment and vibrational symmetry of the C–O bonds. These insights provide a theoretical foundation for understanding the indirectly influence of 4f electronic configurations on SERS spectral behavior.

In the appendix, we describe preliminary results from a complementary spin-based study using nitrogen-vacancy (NV) centers in diamond to measure the T_1 relaxation times of La-citrate and Gd-citrate complexes. Significant T_1 shortening was observed in Gd^{3+}-coated regions due to magnetic fluctuations from its seven unpaired 4f electrons, while La^{3+}-coated regions showed minimal change, consistent with its non-magnetic $4f^0$ configuration. This provides experimental validation of their distinct spin properties.

Final, these findings in above works contribute a novel approach for some Ln^{3+} identification based on vibrational and spin characteristics and also laying the groundwork for future Ln-selective detection and studies of SERS variations response to Ln^{3+}.

Keywords: Surface-enhanced Raman scattering, lanthanide, Raman, DFT, Rare earth

Content

List of figures

Chapter 1: General Introduction

1.1 Research background and academic significance

Lanthanide (Ln) elements, comprising 15 elements from La to Lu, possess highly similar chemical properties and unique physical characteristics such as spectral and magnetic behaviors[1]. These arise from their distinctive 4f electronic configurations. For trivalent lanthanide ions (Ln^{3+}), the electronic configuration is $[Xe]4f^n$ (n = 0-14)[2].

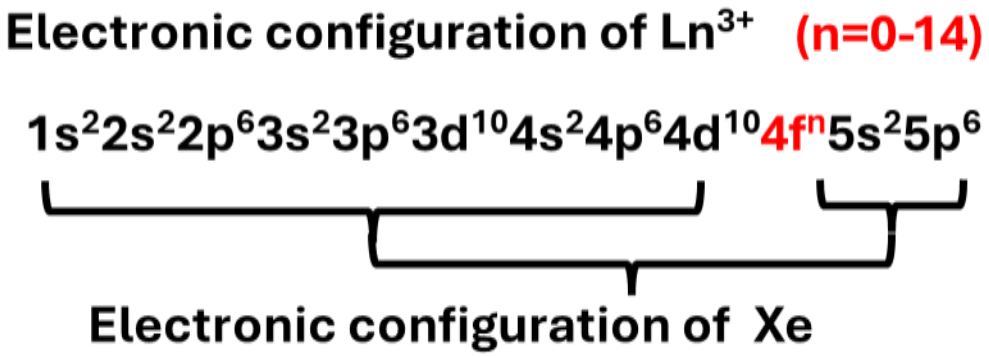

Figure 1.1. Electronic configuration of Ln^{3+}

Due to the shielding effect of the outer 5p and 5s orbitals, the 4f orbitals are not directly involved in chemical bonding, rendering the physical properties of Ln^{3+} ions relatively insensitive to environmental changes[1]. This stability contributes to the difficulty of separating lanthanides while enabling their widespread use in magnetic and luminescent materials, especially in biomedical applications such as magnetic resonance imaging (MRI) contrast agents[2] and fluorescent probes[4-6].

However, the toxicity and residue issues of such materials pose challenges for their detection, highlighting the urgent need for ultrasensitive and non-destructive analytical techniques for lanthanides. Raman spectroscopy is a non-destructive method that provides stable molecular fingerprint information. When target molecules are adsorbed

onto noble metal nanostructures, their Raman signals can be significantly enhanced—a phenomenon known as surface-enhanced Raman scattering (SERS)[7,8]. The SERS enhancement arises mainly from electromagnetic (EM) enhancement[7,8] and chemical enhancement mechanisms, such as charge transfer (CT)[7-9]. The synergy of these mechanisms enables SERS to reach single-molecule detection sensitivity[7,8].

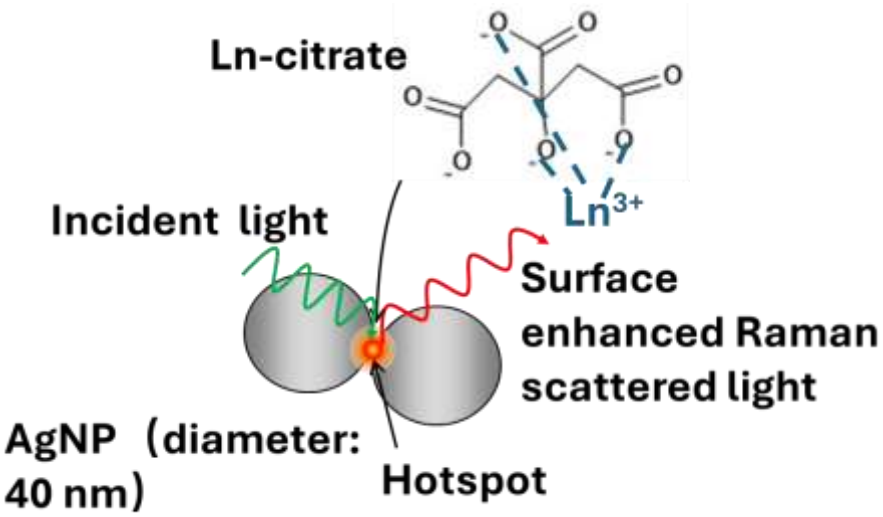

Figure 1.2. SERS measurement of Ln-citrate

To address the challenge of detecting and classifying chemically similar Ln^{3+} ions, we first developed a stable SERS measurement method using citrate capped silver nanoparticles (citrate@AgNPs), which enabled the detection of Ln-citrate complexes at concentrations as low as 10^{-4} M. In parallel, a DFT-based computational approach was optimized to simulate SERS spectra and assign vibrational modes. By combining experimental and theoretical techniques, we systematically investigated the SERS spectral features of seven representative Ln-citrate complexes (Ln = La, Ce, Pr, Nd, Sm, Eu, and Gd), and proposed possible mechanisms underlying the observed spectral variations. This work represents the first systematic SERS investigation of Ln-

molecular complexes, providing new insights into their vibrational behavior and coordination-dependent enhancement effects. In addition, to experimentally validate the spin differences of Ln^{3+} ions, we performed preliminary T_1 relaxation time measurements of La-citrate and Gd-citrate complexes using nitrogen-vacancy (NV) centers in diamond [10] in appendix section.

1.2 Innovative aspects and structure of this thesis

This thesis systematically investigates the SERS signatures of seven prototypical Ln-citrate complexes (Ln = La, Ce, Pr, Nd, Sm, Eu, Gd) and proposes mechanisms that explain their spectral differences. The results suggest a new strategy for detecting otherwise hard-to-distinguish Ln^{3+} ions and open the door to SERS studies on a wide range of Ln-molecular complexes. The innovations of this work can be distilled into four major contributions:

The first innovation is the creation of a robust experimental platform: citrate capped silver-nanoparticle colloids that yield highly reproducible SERS spectra for lanthanide–citrate complexes at concentrations as low as 10^{-4} M. This platform overcomes long-standing instability problems and provides the solid experimental footing on which all later discoveries rest.

The second innovation is an integrated theory–experiment framework. A optimized DFT simulation method employing effective-core potentials(ECP) was developed to simulate the SERS spectra of Ln-citrate, assign vibrational modes to help the analysis of experimental SERS spectra.

The third innovation is the systematically investigates the SERS signatures of

seven prototypical Ln-citrate complexes. The results demonstration that SERS can serve as a practical tool for ion classification. Using the new platform, La^{3+} and Gd^{3+} were distinguished by the relative intensities of their coordination-region SERS peaks. Extending this approach to seven ions (La, Ce, Pr, Nd, Sm, Eu, Gd) revealed SERS relative intensity ratios that track the growing number of unpaired 4f electrons, thereby exposing a indirect link between electronic configurations and SERS variations.

The fourth innovation brings experimental spin response data to support the theoretical spin-state of Ln-citrate. Preliminary NV center measurements of T_1 relaxation times showed dramatic shortening for Gd-citrate films but no significant change for La-citrate, providing a spin-difference confirmation of Ln-citrate complexes.

The structure of this thesis is organized to logically guide the reader from the research motivation and theoretical background to experimental implementation, analysis, and future perspectives.

Chapter 1 outlines the research background, objectives, and highlights the key innovations that motivated this work—particularly the need for sensitive and selective detection methods for chemically similar lanthanide ions.

Chapter 2 introduces the theoretical foundation necessary to understand the study. It covers the fundamentals of lanthanide chemistry, principles of Raman and SERS, as well as the methodologies and limitations of DFT calculations. Additional sections describe supplementary spectroscopic techniques and data processing methods used throughout the thesis.

Chapter 3 presents the development of a stable SERS detection method for La^{3+}

and Gd^{3+} citrate complexes. It includes experimental design, spectral reproducibility verification, DFT-based spectral simulations, vibrational mode assignments, and an analysis of spectral differences. A qualitative classification scheme based on SERS features is proposed, along with a mechanistic interpretation of the observed trends.

Chapter 4 expands the study to a broader range of lanthanide ions, analyzing seven Ln-citrate complexes in total. This chapter explores the dependence of SERS spectral characteristics on the type of Ln^{3+} ion, supported by improved DFT simulations. Potential enhancement mechanisms are discussed, offering insight into how 4f electron configurations influence vibrational signatures.

Chapter 5 summarizes the major findings of the thesis and discusses the broader implications of the research. It also outlines future directions for extending SERS-based techniques to other lanthanide systems and exploring new applications in analytical and materials chemistry.

Appendix introduces a complementary spin-sensitive approach by applying NV centers in diamond to characterize the spin states of lanthanide complexes. Preliminary T_1 relaxation measurements of La-citrate and Gd-citrate films are reported, providing experimental evidence that supports the spin-based differentiation of lanthanide ions.

As the experimental work presented in this dissertation was conducted over the period from 2022 to 2025, the focus and content of each research phase varied accordingly. To ensure completeness and clarity, each chapter is written as a self-contained unit, with full explanations of terminology, experimental procedures, and relevant references provided independently within each chapter.

1.3 References

(1) Cotton, S. *Lanthanide and Actinide Chemistry*; John Wiley & Sons, Ltd: Chichester, 2006; pp 9–102.

(2) Yin, N.; Wang, Y.; Cao, Y.; Huang, Y.; Jin, L.; Zhang, S.; et al. A Biodegradable Nanocapsule for Through-Skull NIR-II Fluorescence Imaging/Magnetic Resonance Imaging and Selectively Enhanced Radio-Chemotherapy for Orthotopic Glioma. *Nano Today* 2022, 46, 101619.

(3) Wang, G.; Peng, Q.; Li, Y. Lanthanide-Doped Nanocrystals: Synthesis, Optical-Magnetic Properties, and Applications. *Acc. Chem. Res.* 2011, 44 (5), 322–332.

(4) Yin, N.; Wang, Y.; Huang, Y.; Cao, Y.; Jin, L.; Liu, J.; et al. Modulating Nanozyme-Based Nanomachines via Microenvironmental Feedback for Differential Photothermal Therapy of Orthotopic Gliomas. *Adv. Sci.* 2023, 10 (3), 2204937.

(5) Pei, P.; Chen, Y.; Chen, X.; Zhang, F.; Liu, X.; Wang, J. W. Optothermal-Stimulated Persistent Luminescence Imaging and Therapy (OSPLIT). *Adv. Mater.* 2025, Early View, 2500769.

(6) Eliseeva, S. V.; Bünzli, J.-C. G. Lanthanide Luminescence for Functional Materials and Bio-Sciences. *Chem. Soc. Rev.* 2010, 39 (1), 189–227.

(7) Itoh, T.; Procházka, M.; Dong, Z.-C.; Ji, W.; Yamamoto, Y. S.; Zhang, Y.; Ozaki, Y. Toward a New Era of SERS and TERS at the Nanometer Scale: From Fundamentals to Innovative Applications. *Chem. Rev.* 2023, 123 (4), 1552–1634.

(8) Yamamoto, Y. S.; Itoh, T. Why and How Do the Shapes of Surface-Enhanced Raman Scattering Spectra Change? Recent Progress from Mechanistic Studies. *J. Raman Spectrosc.* 2016, 47 (1), 78–88.

(9) Albrecht, A. C. On the Theory of Raman Intensities. *J. Chem. Phys.* 1961, 34 (5), 1476–1484.

(10) Schirhagl, Romana, et al. Nitrogen-vacancy centers in diamond: nanoscale sensors for physics and biology. *Annual review of physical chemistry* 2014, 65.1: 83-105.

Chapter 2: Background and Methodological Overview

2.1 Introduction to rare earth elements and lanthanide's properties

Rare earth (RE) elements refer to a group of 17 elements, including 15 lanthanides (atomic numbers 57-71) and two transition metals: scandium (Sc, atomic number 21) and yttrium (Y, atomic number 39) [1-3].

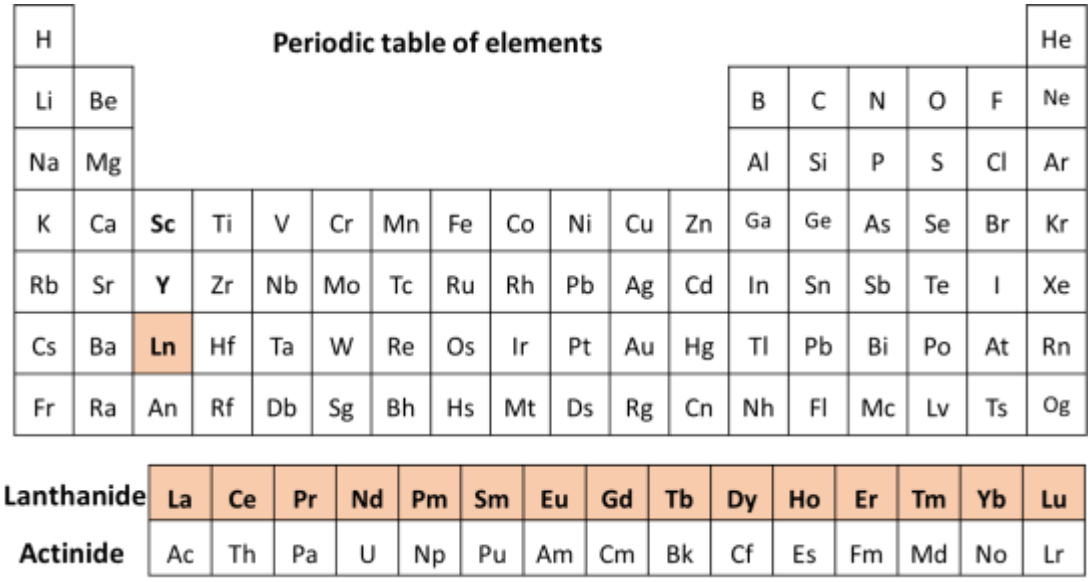

Figure 2.1 Rare earth element in periodic table.

The discovery of RE elements began in the late 18th century. It took nearly 150 years to complete the identification of all RE elements, with promethium (Pm, atomic number 61) being the last one isolated in the 1940s from spent nuclear fuel [1-3].

Among RE elements, the lanthanide (Ln) elements are the most important group. Their physical and chemical properties are largely determined by their special 4f electronic configurations. The atomic and ionic electronic configurations of lanthanides

in different valence states are shown in Table 2.1 [1-3].

Table 2.1. The atomic and ionic electronic configurations of lanthanides in different valence states

Lanthanide	Atom	Ln^{2+}	Ln^{3+}	Ln^{4+}
La	$[Xe]5d^{1}6s^{2}$		[Xe]	
Ce	$[Xe]4f^{1}5d^{1}6s^{2}$		$[Xe]4f^{1}$	[Xe]
Pr	$[Xe]4f^{3}6s^{2}$		$[Xe]4f^{2}$	$[Xe]4f^{1}$
Nd	$[Xe]4f^{4}6s^{2}$	$[Xe]4f^{4}$	$[Xe]4f^{3}$	$[Xe]4f^{2}$
Pm	$[Xe]4f^{5}6s^{2}$		$[Xe]4f^{4}$	
Sm	$[Xe]4f^{6}6s^{2}$	$[Xe]4f^{6}$	$[Xe]4f^{5}$	
Eu	$[Xe]4f^{7}6s^{2}$	$[Xe]4f^{7}$	$[Xe]4f^{6}$	
Gd	$[Xe]4f^{7}5d^{1}6s^{2}$		$[Xe]4f^{7}$	
Tb	$[Xe]4f^{9}6s^{2}$		$[Xe]4f^{8}$	$[Xe]4f^{7}$
Dy	$[Xe]4f^{10}6s^{2}$	$[Xe]4f^{10}$	$[Xe]4f^{9}$	$[Xe]4f^{8}$
Ho	$[Xe]4f^{11}6s^{2}$		$[Xe]4f^{10}$	
Er	$[Xe]4f^{12}6s^{2}$		$[Xe]4f^{11}$	
Tm	$[Xe]4f^{13}6s^{2}$	$[Xe]4f^{13}$	$[Xe]4f^{12}$	
Yb	$[Xe]4f^{14}6s^{2}$	$[Xe]4f^{14}$	$[Xe]4f^{13}$	
Lu	$[Xe]4f^{14}5d^{1}6s^{2}$		$[Xe]4f^{14}$	

According to Table 2.1, the 4f orbitals are gradually filled from lanthanum (La) to lutetium (Lu). The most common oxidation state is +3, and only a few lanthanides form stable +2 or +4 ions. The 4f orbitals are located inside the 5s and 5p shells and are shielded by the outer 6s and 5d orbitals. Therefore, 4f electrons have low chemical

reactivity, and their participation in bonding is limited. This leads to very similar chemical properties among lanthanides and makes them difficult to separate [1-3]. Additionally, due to the localized nature of the 4f orbitals and weak coupling with external ligand fields, their spectroscopic and magnetic properties are generally stable [1-3].

The atomic masses [4], atomic radii [1], and ionic radii [1] of lanthanides are summarized in Table 2.2. Except for europium (Eu) and ytterbium (Yb), the atomic radii decrease gradually from La to Lu. The sudden increase in radius for Eu and Yb is due to their half-filled and fully filled 4f electronic configurations. These configurations are energetically stable and provide stronger shielding of the nuclear charge, resulting in reduced effective nuclear charge and increased atomic radius. For trivalent lanthanide ions (Ln^{3+}), as the atomic number increases, the nuclear charge increases and the attraction to 4f electrons becomes stronger. Because the shielding between 4f electrons is weak, the effective nuclear charge increases, causing a gradual decrease in ionic radius. This phenomenon is known as the lanthanide contraction [1-3]. Some Ln^{3+} ions have very similar electronic configurations and ionic radii. For example, Pr^{3+} and Nd^{3+} differ in atomic mass by 3.3, but their ionic radii differ by only 0.7 pm. Considering that the mass of electrons is negligible, the mass of Ln^{3+} ions is almost equal to the atomic mass of the corresponding neutral atoms. Therefore, detection methods that are sensitive to mass differences may offer potential for distinguishing between different Ln^{3+} ions.

Table 2.2. Basic information of lanthanides

Ln atom	Atomic mass	Atomic radii (pm)	Ln^{3+} ion	Ionic radii (pm)
La	138.9	187.7	La^{3+}	103.2
Ce	140.1	182.5	Ce^{3+}	101.0
Pr	140.9	182.8	Pr^{3+}	99.0
Nd	144.2	182.1	Nd^{3+}	98.3
Pm	145	181.0	Pm^{3+}	97.0
Sm	150.4	180.2	Sm^{3+}	95.8
Eu	152	204.2	Eu^{3+}	94.7
Gd	157.3	180.2	Gd^{3+}	93.8
Tb	158.9	178.2	Tb^{3+}	92.3
Dy	162.5	177.3	Dy^{3+}	91.2
Ho	164.9	176.6	Ho^{3+}	90.1
Er	167.3	175.7	Er^{3+}	89.0
Tm	168.9	174.6	Tm^{3+}	88.0
Yb	173	194.0	Yb^{3+}	86.8
Lu	175	173.4	Lu^{3+}	86.1

2.2 Quantum numbers and energy levels of lanthanide ions

The unique 4f electronic structures of lanthanides also determine their optical and magnetic properties. In a multi-electron atom, each electron is defined by four quantum numbers:

- Principal quantum number **n**: determines energy level (for 4f orbitals, **n**=4);
- Angular momentum quantum number $\boldsymbol{l}$: defines orbital type ($\boldsymbol{l}$=3 for f orbitals);
- Magnetic quantum number $\mathbf{m}_{\boldsymbol{l}}$: ranges from $-\boldsymbol{l}$ to $+\boldsymbol{l}$, giving $2\boldsymbol{l}+1 = 7$ orientations;
- Spin quantum number $\mathbf{m}_s$: ±1/2.

The total quantum numbers of lanthanide ions can be calculated based on the Russell-Saunders coupling scheme [5]. Their total orbital angular momentum **L**, total spin **S**, and total angular momentum **J**, as well as the ground-state spectroscopic term $^{2S+1}\mathbf{L}_J$, are determined by the number of 4f electrons [2], as shown in Table 2.3.

Based on Table 1.3, a plot of **S, L, J,** and the number of 4f electrons is shown in Figure 2.2.

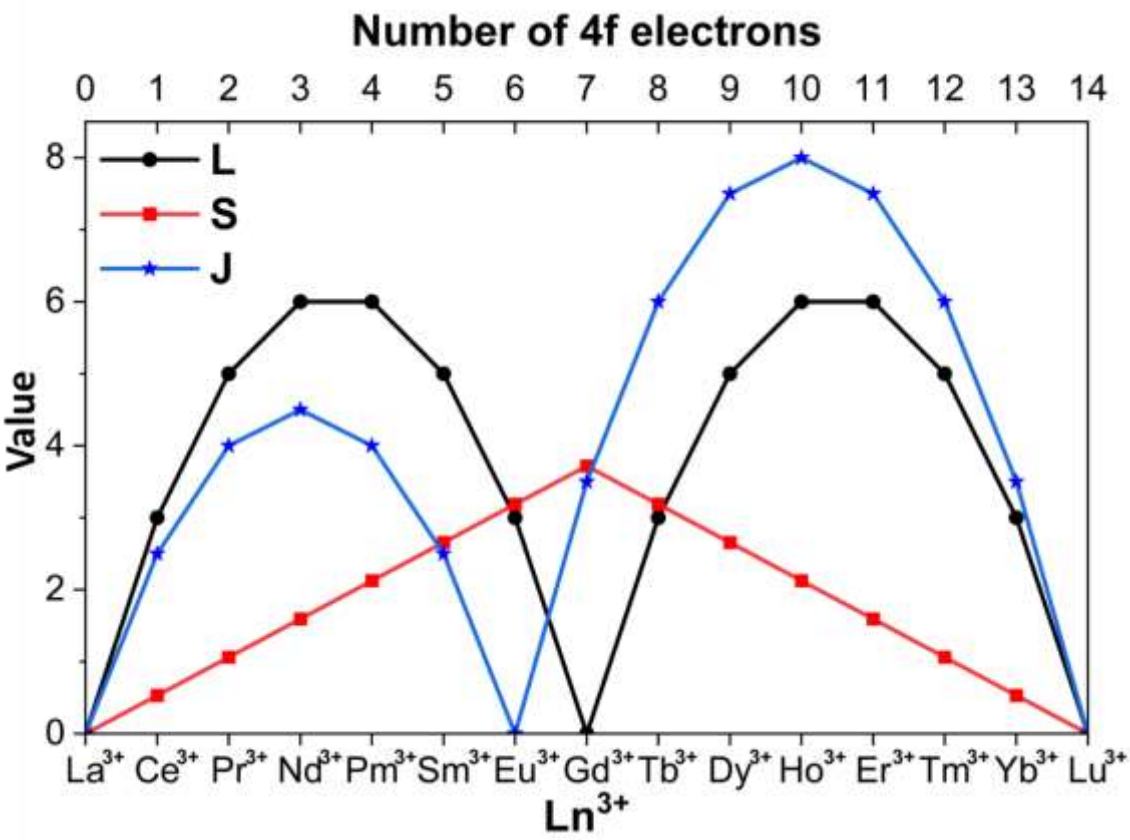

Figure 2.2. **L**, **S**, **J**, and the number of 4f electrons of Ln^{3+}

Figure 2.2 illustrates the variation trends of the total spin quantum number **S**, total orbital angular momentum quantum number **L**, and total angular momentum quantum number **J** of Ln^{3+} ions as a function of the number of 4f electrons.

The total spin quantum number **S** increases with the number of unpaired 4f electrons and reaches a maximum at $Gd^{3+}(4f^7)$, where the 4f orbital is half-filled. Specifically, from $La^{3+}(4f^0)$ to $Gd^{3+}(4f^7)$, the number of unpaired electrons increases, resulting in an increasing trend in **S**. From $Gd^{3+}(4f^7)$ to $Lu^{3+}(4f^{14})$, the number of unpaired electrons decreases, leading to a decrease in **S**. **L** exhibit a periodic variation

with two symmetric peaks centered around Gd^{3+}. This reflects the symmetry of electron filling around the half-filled 4f shell. For **J**, the coupling rule follows **J=L+S** when the number of 4f electrons is less than 7, and **J=L−S** when the number is equal to or greater than 7. As a result, the transition point between the two peaks of **J** lies in $Eu^{3+}(4f^6)$.

The patterns of quantum numbers shown in Table 2.3 and Figure 2.2 explain the trends in spectroscopic, magnetic, and chemical properties of lanthanides. They also lead to the complex energy level structures of these ions, as illustrated in the well-known Dieke diagram [6], as shown in Figure 2.3.

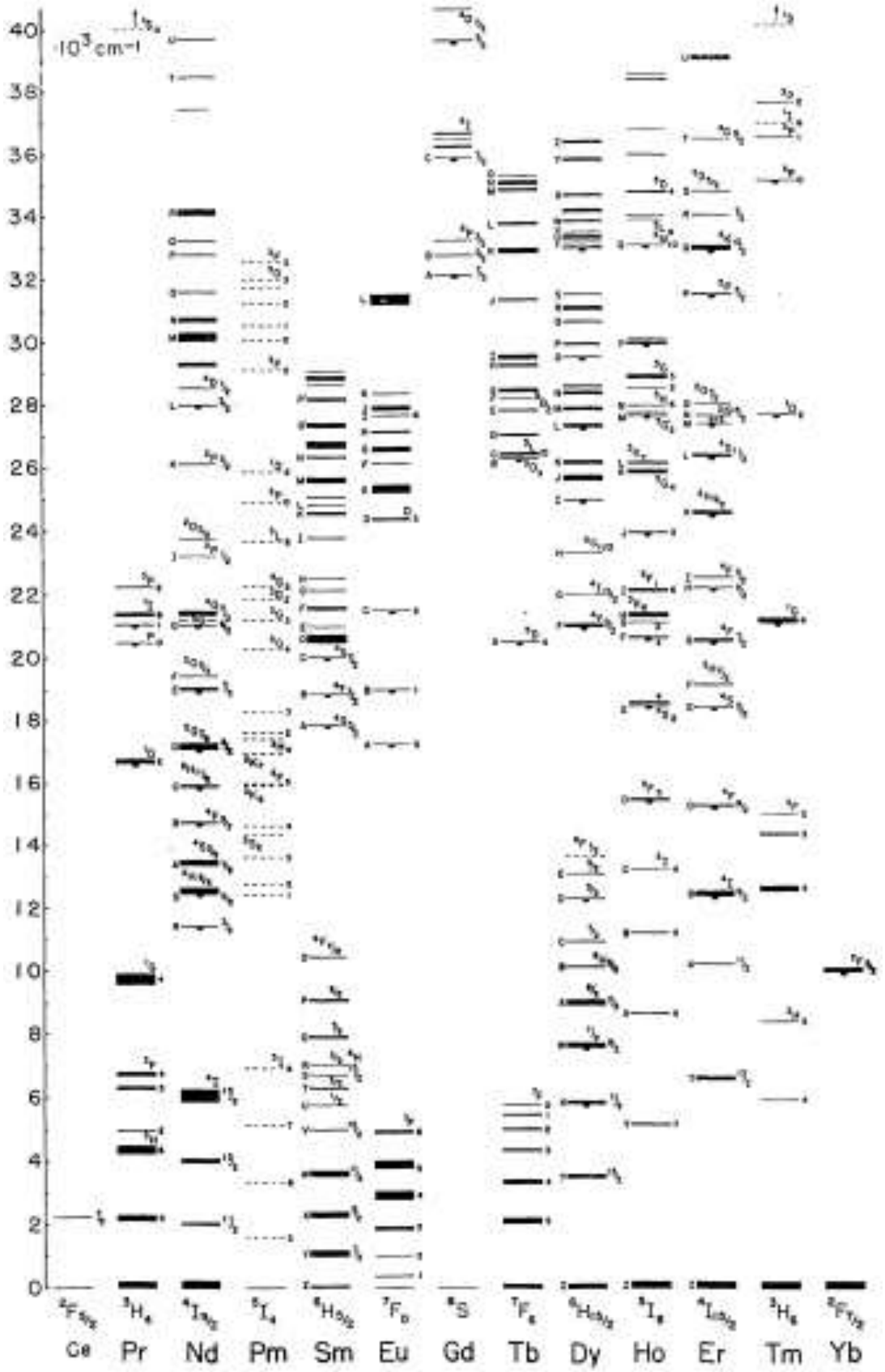

Figure 2.3. Dieke diagram, cited from ref.6

Table 2.3 **L**, **S**, **J** information of Ln^{3+}

Ln^{3+} ion	Atomic number	Number of 4f electrons	Number of magnetic quantum number in 4f orbital							L	S	J	$^{2S+1}L_J$
			3	2	1	0	-1	-2	-3				
La^{3+}	57	0								0	0	0	$^1S_0$
Ce^{3+}	58	1	↑							3	1/2	5/2	$^2F_{5/2}$
Pr^{3+}	59	2	↑	↑						5	1	4	$^3H_4$
Nd^{3+}	60	3	↑	↑	↑					6	3/2	9/2	$^4I_{9/2}$
Pm^{3+}	61	4	↑	↑	↑	↑				6	2	4	$^5I_4$
Sm^{3+}	62	5	↑	↑	↑	↑	↑			5	5/2	5/2	$^6H_{5/2}$
Eu^{3+}	63	6	↑	↑	↑	↑	↑	↑		3	3	0	$^7F_0$
Gd^{3+}	64	7	↑	↑	↑	↑	↑	↑	↑	0	7/2	7/2	$^8S_{7/2}$
Tb^{3+}	65	8	↑↓	↑	↑	↑	↑	↑	↑	3	3	6	$^7F_6$
Dy^{3+}	66	9	↑↓	↑↓	↑	↑	↑	↑	↑	5	5/2	15/2	$^6H_{5/2}$
Ho^{3+}	67	10	↑↓	↑↓	↑↓	↑	↑	↑	↑	6	2	8	$^5I_8$
Er^{3+}	68	11	↑↓	↑↓	↑↓	↑↓	↑	↑	↑	6	3/2	15/2	$^4H_{15/2}$
Tm^{3+}	69	12	↑↓	↑↓	↑↓	↑↓	↑↓	↑	↑	5	1	6	$^3H_6$
Yb^{3+}	70	13	↑↓	↑↓	↑↓	↑↓	↑↓	↑↓	↑	3	1/2	7/2	$^2F_{7/2}$
Lu^{3+}	71	14	↑↓	↑↓	↑↓	↑↓	↑↓	↑↓	↑↓	0	0	0	$^1S_0$

2.3 Applications and problems of lanthanide

Because of these special properties, lanthanide elements are widely used in the design of functional materials [7-12]. In biomedical fields, they are applied in fluorescent probes [7-9], magnetic resonance imaging (MRI) contrast agents [10-12], photothermal therapy nanomedicines [13-15], and scintillators in medical devices [16]. In the energy sector, they are used in phosphors [17] and solid-state hydrogen storage materials [18]. In emerging fields, they also show potential in quantum computing [19].

However, their similar chemical properties make it very difficult to separate them. In biomedical applications, detecting residual Ln^{3+} ions and studying their toxicity has become increasingly important [20,21]. Therefore, there is a growing need to develop highly sensitive detection methods that can identify individual lanthanide ions based on their unique characteristics. Ln^{3+} have rich energy levels, which give them many absorption and emission lines. This makes them useful in functional materials, especially in luminescent applications. However, it also creates problems for their detection. For example, some Ln^{3+} ions have overlapping absorption spectra, making them difficult to distinguish, especially at high concentrations. In other cases, their fluorescence emission ranges overlap, which makes classification based on fluorescence spectra challenging. Moreover, some Ln^{3+} ions, such as La^{3+} and Gd^{3+}, do not exhibit any optical signals in the visible range. As a result, it is difficult to collect characteristic signals for all Ln^{3+} ions using fluorescence or absorption spectroscopy alone. It is valuable for developing sensitive vibrational spectroscopy-based techniques for detecting the spectral characteristics of different Ln^{3+} ions.

2.4 Raman and surface-enhanced Raman spectroscopy (SERS)

To address the issue in detection of Ln^{3+}. We started the new detection method development based on Raman spectroscopy. Raman spectroscopy is one type of vibrational spectroscopy based on light scattering. When photons interact with molecules, most undergo elastic scattering (Rayleigh scattering), while a small portion couples with molecular vibrations and undergoes energy exchange, resulting in photons with slightly different energies. This inelastic scattering is called Raman scattering [22].

The energy difference corresponds to the vibrational energy levels of the molecule and is expressed as the Raman shift in wavenumbers (cm^{-1}). When the scattered photon loses energy, it is called Stokes scattering; when it gains energy, it is called anti-Stokes scattering. Figure 2.4 shows the different types of scattering processes.

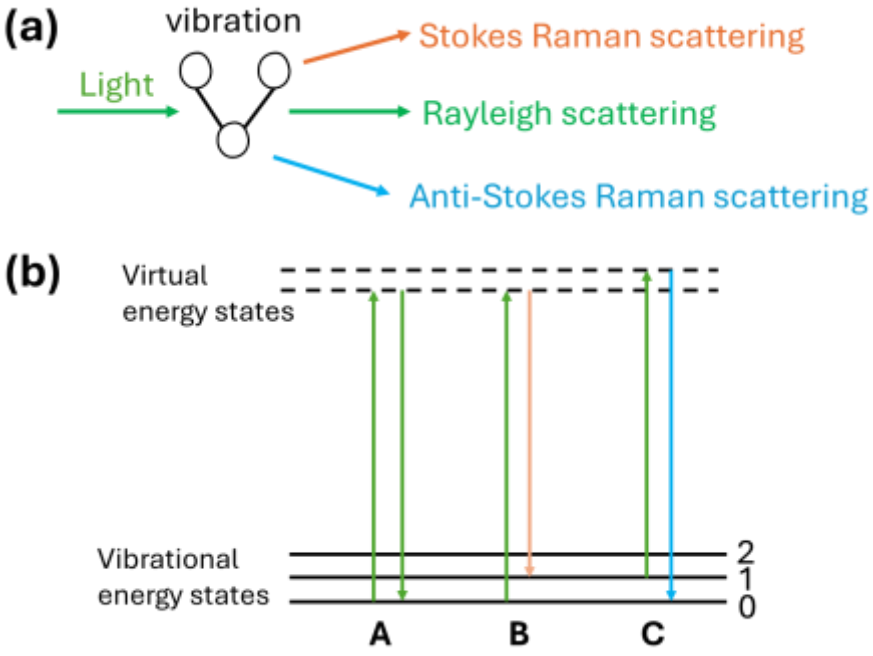

Figure 2.4. (a)Schematic of different scattering processes; (b)schematic of different scattering processes. **A**: Rayleigh scattering; **B**: Stokes Raman scattering; **C**: Anti-Stokes Raman scattering.

In classical mechanics, Raman scattering is explained as an inelastic light scattering process caused by the time-dependent variation of the induced electric dipole moment under an external electromagnetic field[22]. When a molecule is irradiated by an incident laser field E, the electronic cloud is distorted, resulting in an induced dipole moment μ, which is proportional to the molecular polarizability α. It is expressed as:

$$\mu = \alpha E \qquad (2.1)$$

During molecular vibration, the polarizability α changes with the vibrational coordinate Q, which can be expressed as:

$$\alpha = \alpha_0 + \left(\frac{d\alpha}{dQ}\right) Q \qquad (2.2)$$

Where α_0 is the non-vibrational polarizability. Thus, according to equation, Raman scattering occurs only when the derivative $\left(\frac{d\alpha}{dQ}\right) \neq 0$, which constitutes the fundamental condition for Raman activity. The intensity of scattered light is proportional to the square of the second time derivative of the dipole moment. Therefore, the Raman scattering intensity is proportional to the square of $\left(\frac{d\alpha}{dQ}\right)$:

$$I_{Raman} \propto \left(\frac{d\alpha}{dQ}\right)^2 \qquad (2.3)$$

Quantum mechanically, Raman scattering involves a two-photon process where a molecule is first excited to a virtual energy level and then returns to a vibrational excited state, emitting a scattered photon with shifted energy. The Raman scattering intensity I_{mn}, corresponding to the transition from state m to state n, is described by the following equations[22-24]:

$$I_{mn} = \frac{128\pi^5}{9C^4} (v_i \pm v_{mn})^4 I_i \sum_{p\sigma} \left|(\alpha_{\rho\sigma})_{mn}\right|^2 \qquad (2.4)$$

$$\left(\alpha_{\rho\sigma}\right)_{mn} = \frac{1}{h}\sum_e \left[\frac{\langle m|\mu_\sigma|e\rangle\langle e|\mu_\rho|n\rangle}{v_{em}-v_i+\mathrm{i}\Gamma_e} + \frac{\langle m|\mu_\rho|e\rangle\langle e|\mu_\sigma|n\rangle}{v_{en}+v_i+\mathrm{i}\Gamma_e}\right] \quad (2.5)$$

Where, I_i is the intensity of the incident light with frequency v_i. v_{mn}represents the Raman shift. $\alpha_{\rho\sigma}$denotes the component $\rho\sigma$of the Raman scattering tensor. The summation e includes all quantum mechanical eigenstates of the molecule. v_{em} and v_{en} are the transition frequencies from state m to e and from state e to n, respectively. The terms $\langle m|\mu_\sigma|e\rangle$, $\langle e|\mu_\rho|n\rangle$, $\langle m|\mu_\rho|e\rangle$ and $\langle e|\mu_\sigma|n\rangle$ represent the components of the transition electric dipole moment. μ_σ and μ_ρ are the electric dipole moment operators in the σ (Raman excitation) and ρ (Raman scattering) direction, respectively. Γ_e denotes the damping constant of the state. Equation (2.4) indicates that the Raman scattering intensity is proportional to the fourth power of the scattered light frequency $v_i \pm v_{mn}$. As $v_i \gg v_{mn}$, the Raman scattering intensity is considered proportional to the fourth power of the incident light frequency v_i.

When the excitation light frequency is close to or matches an electronic transition of the molecule, the Raman signal is strongly enhanced. This is called resonance Raman scattering[22].

Generally, Raman scattering is a weak effect, making molecular Raman signals challenging to detect. However, when molecules are adsorbed onto the surface of nanostructured noble metals, the Raman signal can be significantly enhanced[25-27]. This phenomenon is called surface-enhanced Raman scattering (SERS), first reported in 1974 by Fleischmann[28].This enhancement is primarily attributed to two mechanisms:

- **Electromagnetic enhancement**: due to the local field enhancement caused by

localized surface plasmon resonance (LSPR)[25,26];

- **Chemical enhancement**: caused by resonance effect, charge transfer (CT) effect, and adsorption effect between the molecule and the metal surface[25,26].

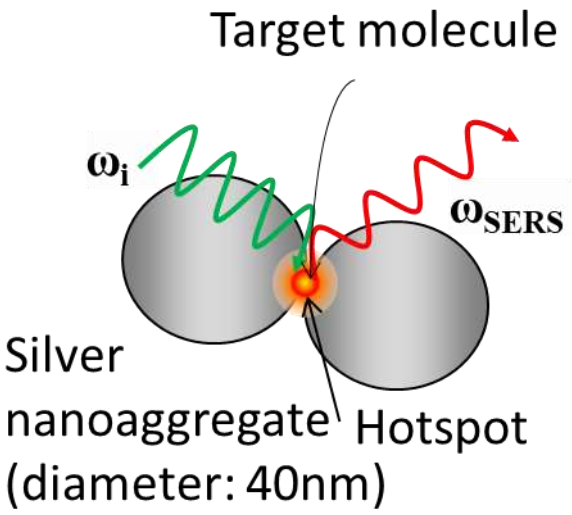

Figure 2.5 SERS process

SERS is a powerful spectroscopic technique capable of detecting Raman signals from low-concentration analytes, even down to the single-molecule level[27]. This remarkable sensitivity arises primarily from the electromagnetic (EM) enhancement mechanism, which is dominant in most SERS systems[25,26]. The EM effect originates from the LSPR generated in nanoscale regions of intense electromagnetic field, commonly referred to as “hot spots”, formed by the aggregation or specific geometry of metal nanoparticles[25,26].

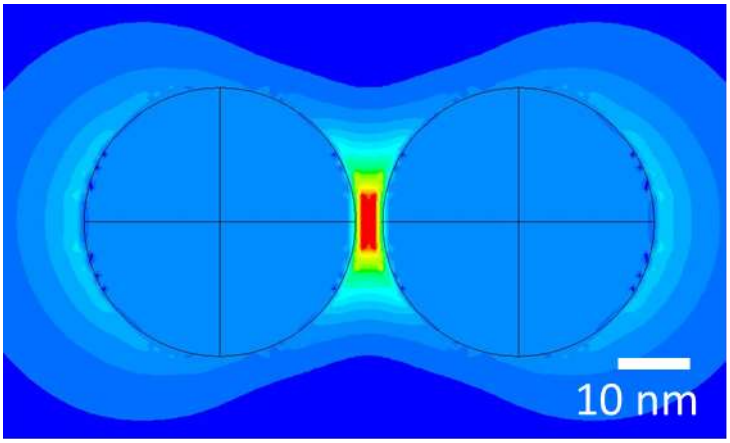

Figure 2.6. Simulation of hotspot

According to previous studies by Itoh et al[26,29]., the strength and spatial distribution of LSPR, and thus the EM enhancement are governed by several key factors, including the size, shape, and dielectric properties of the metal nanostructures, as well as the refractive index of the surrounding medium[30]. The SERS spectral profile is strongly influenced by the spatial overlap between the LSPR distribution and the region of molecular adsorption: only in areas of high plasmonic intensity do significant SERS signals emerge[25-27,29]. Notably, the position of the LSPR peak remains relatively fixed, while the position of the Raman scattering depends on the excitation laser wavelength[26,29]. This mismatch can lead to observable variations in the SERS spectral shape when tuning the excitation wavelength.

In addition to EM enhancement, SERS also involves a more complex chemical enhancement (CE) mechanism, which comprises three major contributions[26]:

(a) enhancement due to ground-state chemical interactions between the adsorbed molecule and the nanoparticle, independent of photon excitation;

(b) resonance Raman enhancement arising from molecular electronic transitions; and

(c) charge-transfer (CT) resonance enhancement involving electronic transitions between the nanoparticle and the molecule.

The CT mechanism can induce a shift from non-resonant to resonant Raman behavior through the formation of CT complexes[26]. This effect introduces vibronic coupling which are absent in conventional non-resonant Raman spectra[31]. These features provide unique spectroscopic fingerprints that reflect the molecule–substrate interaction at the electronic level[25,26].

Although it has been shown that SERS can be used for detecting Ln^{3+} ions, achieving this in early experiments was very difficult. Because vibrational spectroscopy relies on the vibrations of chemical bonds, individual ions or atoms cannot be directly detected. At first, we tried to adsorb Ln–DTPA complexes onto the surface of AgNPs, but this approach failed. The reason was that the surface of AgNPs was already coated with citrate, and Ln–DTPA could not replace it.

Later, we considered that citrate contains carboxyl and hydroxyl groups, which can coordinate with Ln^{3+} ions. Therefore, we directly added Ln^{3+} ions into the AgNP colloid. As the citrate on the surface coordinated with the Ln^{3+} ions, Ln-citrate complexes were formed in situ on the surface of AgNPs. This allowed us to detect the SERS signals of Ln-citrate complexes and investigate the effects of different Ln^{3+} ions through their spectral features. Using this idea, we conducted the first systematic SERS study of seven Ln–citrate complexes, where Ln^{3+} ions range from La to Gd (excluding Pm). In this series, the spin quantum number (**S**) of Ln^{3+} ions increases gradually from 0 to 7/2, showing a regular trend. The details of this investigation are discussed in

Chapters 3 and 4.

2.5 DFT calculations and Raman spectrum simulation

Assigning peaks in experimental Raman and SERS spectra is challenging. To assist in peak assignment, quantum chemical simulation methods have been widely employed, with density functional theory (DFT) being one of the most commonly used approaches[32]. DFT is a first-principles method for calculating ground-state properties of multi-electron systems. It can simulate vibrational spectra[32-35], including Raman and infrared (IR) spectra, and provide insight into electronic structures and related physical parameters.

The theoretical model for Raman simulations using DFT is based on the approach proposed by P. L. Polavarapu [36]. In this model, polarizability tensors are calculated under static electric fields [36], which differ from the dynamic electromagnetic nature of incident light [22-26,29,30]. Since Raman intensity is proportional to the square of the change in polarizability with respect to the normal mode displacement[22-24], the relative intensities of simulated spectra often differ from experimental results. Furthermore, the simulated Raman intensity *I* should be converted from the Raman scattering activity of each vibrational mode using the following equation [37].

$$I_i = \frac{C(v_0 - v_i)^4 S_i}{v_i B_i}; B_i = 1 - \exp\left(-\frac{hv_i C}{k_B T}\right) \quad (2.6)$$

where *i* is the vibrational mode, C is the normalization factor that can be arbitrarily chosen, *v* is the vibrational frequency, v_0 is the frequency of incident light. *S* is Raman activity calculated by quantum chemistry packages, e.g., Gaussian 16. h, c, k_B, and T

are Planck constant, light speed, Boltzmann constant, and temperature, respectively. In the present work, the values of v_0 and T were chosen to be 532 nm and 298.15K, respectively, to match the experimental conditions.

DFT calculations of vibrational frequencies are performed under the harmonic oscillator approximation[33], which neglects real molecular effects such as anharmonicity, solvent interactions, functional limitations, and basis set incompleteness[32-35]. As a result, DFT-predicted frequencies are typically higher than experimental values. To address this, scaling factors are commonly applied to the calculated frequencies[33-35]. The appropriate scaling factor depends on the chosen functional and basis set[33-35].

Reliable simulations require the careful selection of functionals, basis sets, and solvent models [33-35]. In particular, polarizability calculations demand basis sets that include diffuse functions [38]. For certain metal elements such as lanthanides, additional considerations are required due to relativistic effects[2], multiple spin states[1-3], and the strongly localized nature of 4f orbitals[1-3].

The results of DFT calculations can be visualized as 3D molecular structures. In this thesis, these 3D structures are presented as 2D projections from specific viewing angles. It is important to note that due to the projection from 3D to 2D, the scale bar in the 2D images cannot accurately represent the full dimensions of the original 3D structure. Therefore, in this thesis, the scale bars for the structural illustrations are defined based on constant reference distances. For the structures used in SERS simulations, where most silver atoms in the Ag cluster are fixed at specific intervals,

the scale bar is set using the distance between two adjacent Ag atoms. In contrast, for the spin population analysis of the Ln-citrate complexes, the scale bar is defined using the bond length between the oxygen atom of a hydroxyl group and the coordinated Ln^{3+} ion.

2.6 Basis sets and pseudopotentials for lanthanide ions

DFT simulations of lanthanides are challenging for several reasons[1-3,39]:

1. **Strong relativistic effects**: Lanthanides exhibit significant scalar and spin-orbit relativistic interactions.
2. **Highly localized 4f orbitals**: These orbitals contribute minimally to bonding but significantly to magnetic and optical properties.
3. **Complex multi-electron states**: Multiple low-lying spin states complicate convergence and accuracy.

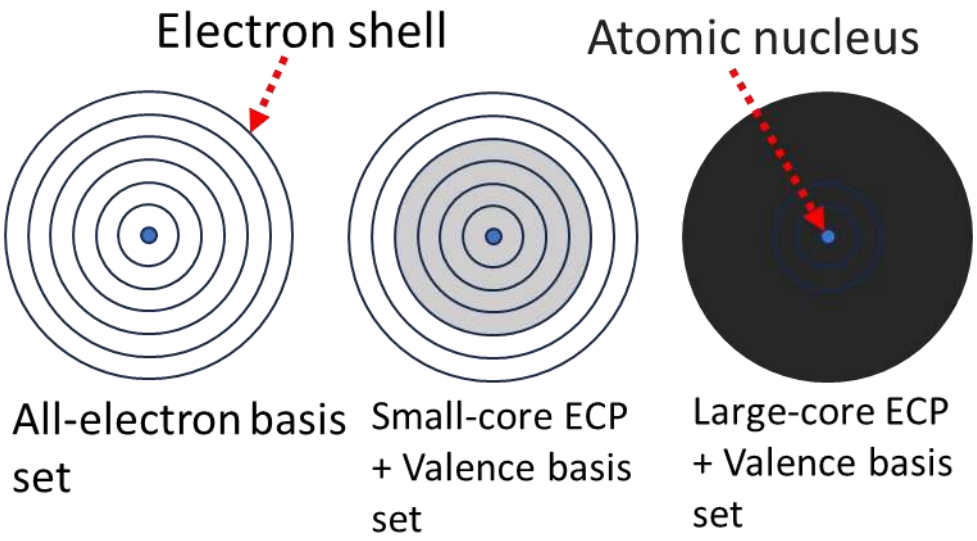

Figure 2.7. Different basis sets for Ln^{3+}

Lanthanides have multiple options for basis sets and core electron treatment[39]:

- **All-electron basis sets**: Treat all electrons explicitly. These are accurate but computationally expensive and are not available for all lanthanides. They are suitable for high-precision studies of energy levels and spectroscopic transitions.
- **Small-core pseudopotentials**: Replace inner core electrons (e.g., 1s-3d) by effective core potentials (ECP), retaining 4f, 5s, 5p, 5d, and 6s as valence electrons. This method balances accuracy and efficiency and is suitable for structure optimization and vibrational simulations.
- **Large-core pseudopotentials**: Even 1s-4f electrons are replaced by ECPs, and only 5s, 5p, 6s, and higher are treated explicitly. These are computationally efficient but unsuitable for 4f electron-based studies, as they ignore the influence of 4f orbitals.

In principle, all-electron methods provide the most accurate description. However, due to limitations in computational cost and availability, different pseudopotentials (or called as ECPs) combined with triple-zeta basis sets are typically used for lanthanide-related simulations in this work.

2.7 Limitations of SERS simulations

As shown in Figure 2.8, small molecule-metal cluster adsorption models are used to approximate molecule–metal interactions in SERS simulations.

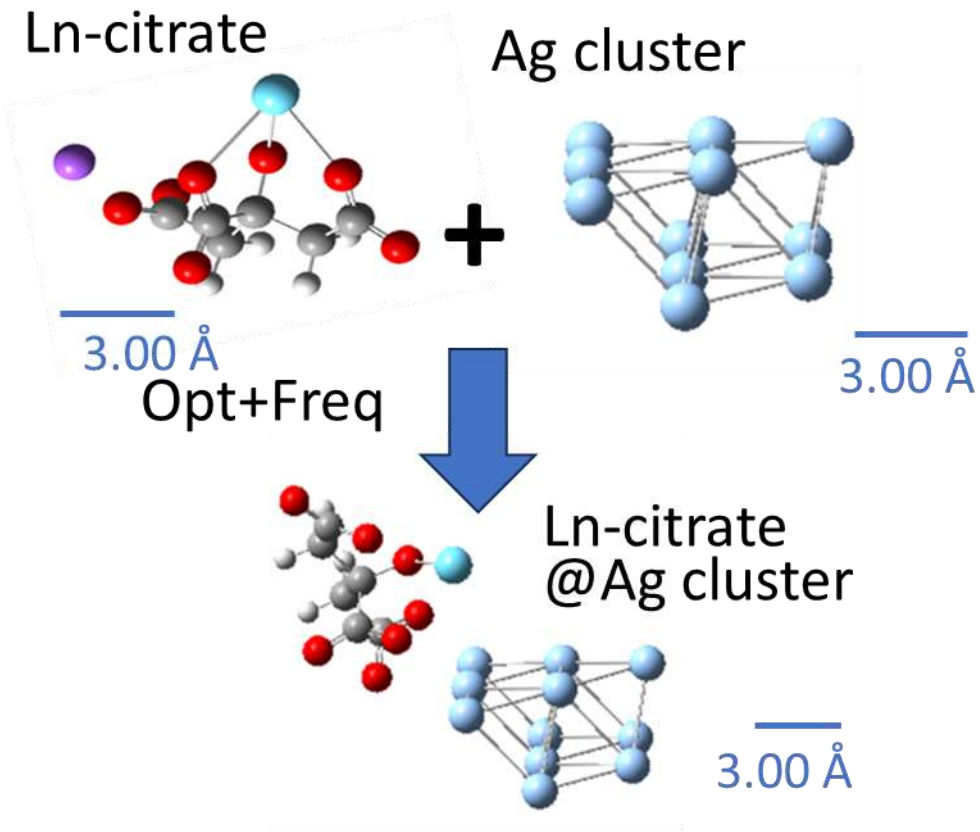

Figure 2.8 SERS simulation method

However, due to the limited size of the metal clusters, plasmonic effects cannot be directly represented. As a result, DFT-based SERS simulations reflect only chemical enhancement mechanisms, and discrepancies in spectral intensity compared to experimental results are also observed. Nevertheless, after applying frequency corrections, DFT-calculated spectra remain highly valuable for peak assignment and vibrational mode interpretation, both of which are essential for understanding how different lanthanide ions influence SERS signals.

2.8 Other spectroscopic methods and data preprocessing

In addition to Raman and SERS spectra, UV-Vis absorption and extinction

spectroscopy[40] were also employed in this study. These techniques provide insight into the electronic transitions and resonance regions of Ln-molecule complexes, assisting in the selection of appropriate excitation wavelengths for SERS and in the interpretation of possible enhancement mechanisms. A brief explanation is provided here.

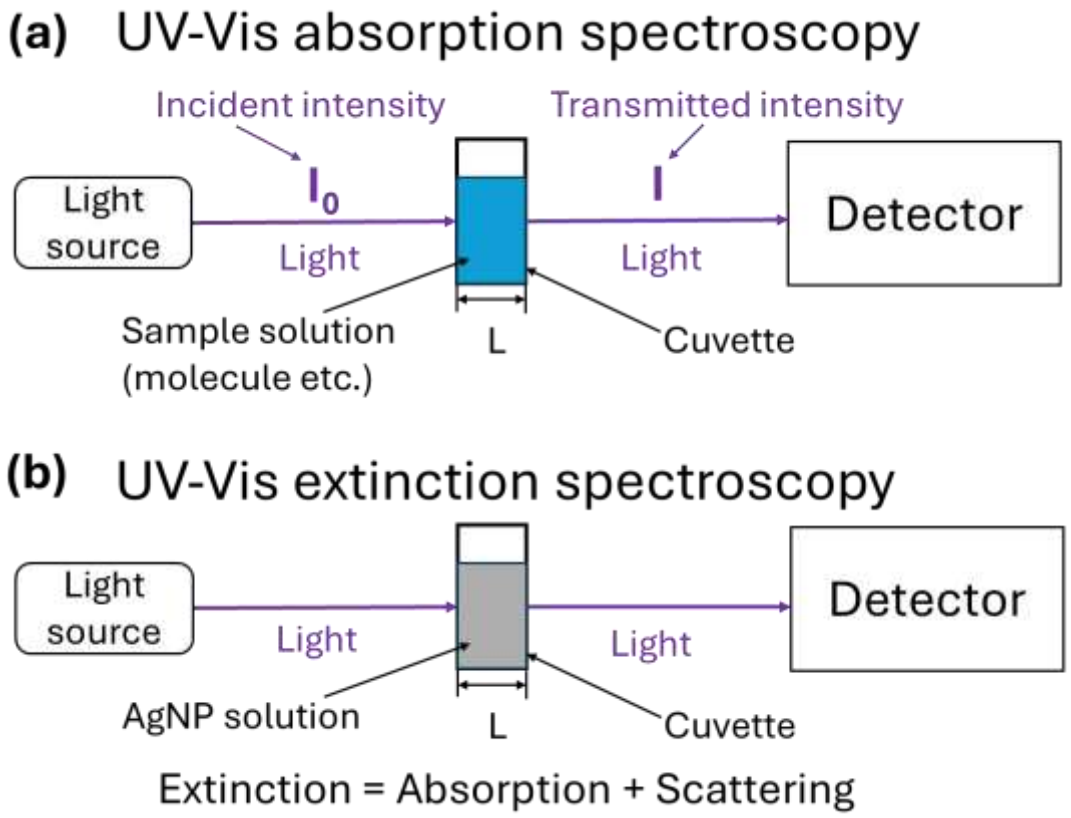

Figure 2.9 (a)UV-Vis absorption spectroscopy;(b)UV-Vis extinction spectroscopy

The UV-Vis absorption spectrum reflects how a sample absorbs incident light across the ultraviolet–visible range (200–800 nm), and is commonly used to investigate electronic transitions within molecules[40,41]. In contrast, the UV-Vis extinction spectrum measures the total loss of light energy as it passes through a sample, which includes both absorption and scattering[40]. For SERS samples, strong absorption and scattering are typically caused by LSPR[25]. Therefore, the UV-Vis extinction spectrum

serves as an important tool for characterizing the LSPR features of SERS samples.

Raman and SERS spectra are influenced by various sources of interference, including instrumental noise, baseline drift, fluorescence background, laser instability, and sample inhomogeneity. These factors degrade the signal-to-noise ratio (SNR), distort spectral features, and hinder accurate peak identification.

To ensure reliable qualitative and quantitative analysis, raw spectral data must undergo appropriate preprocessing. In this study, the preprocessing steps are as follow: First, baseline correction was carried out manually to achieve precise removal of background drift, which is caused by fluorescence or instrument instability. Next, noise reduction was performed using the Savitzky–Golay (SG) method[42]. This smoothing technique fits successive subsets of adjacent data points with low-degree polynomials, effectively eliminating high-frequency noise while maintaining the original shape and position of spectral peaks. This is particularly important for SERS spectra, where small peak differences are critical for ion classification. After noise reduction, the spectra were normalized to minimize signal variations caused by differences among measurement points. Normalization was performed using characteristic peak intensity ratios, which helped ensure consistent comparison across different measurements. Finally, to evaluate reproducibility and detect meaningful spectral variations, comparisons were made across multiple independent measurements under the same experimental conditions. This step confirmed the stability of the peak positions and intensity ratios, which are essential for subsequent analysis of lanthanide-specific SERS features. Raman shifts of all spectra were fixed by indene to avoid errors from the

instrument.

2.9 References

(1) Cotton, S. *Lanthanide and Actinide Chemistry*; John Wiley & Sons, Ltd: Chichester, 2006; pp 9–102.

(2) Hong, G. *Introduction to Rare Earth Chemistry*; Science Press: Beijing, 2014.

(3) Adachi, G. *Science of Rare Earth Elements*; Kagaku Dojin: Kyoto, 1999.

(4) Linstrom, P. *NIST Chemistry WebBook, NIST Standard Reference Database 69*; National Institute of Standards and Technology: Gaithersburg, MD, 1997.

(5) Russell, H. N.; Saunders, F. A. New Regularities in the Spectra of the Alkaline Earths. *Astrophys. J.* 1925, 61, 38.

(6) Dieke, G. H.; Crosswhite, H. M. The Spectra of the Doubly and Triply Ionized Rare Earths. *Appl. Opt*. 1963, 2 (7), 675–686.

(7) Wang, G.; Peng, Q.; Li, Y. Lanthanide-Doped Nanocrystals: Synthesis, Optical-Magnetic Properties, and Applications. *Acc. Chem. Res.* 2011, 44 (5), 322–332.

(8) Eliseeva, S. V.; Bünzli, J.-C. G. Lanthanide Luminescence for Functional Materials and Bio-Sciences. *Chem. Soc. Rev.* 2010, 39 (1), 189–227.

(9) Kotyk, C. M.; Weber, J. E.; Hyre, A. S.; McNeely, J.; Monteiro, J. H. S. K.; Domin, M.; Balaich, G. J.; Rheingold, A. L.; de Bettencourt-Dias, A.; Doerrer, L. H. Luminescence of Lanthanide Complexes with Perfluorinated Alkoxide Ligands. *Inorg. Chem.* 2020, 59 (14), 9807–9823.

(10) Lee, H. Y.; Jee, H. W.; Seo, S. M.; Kwak, B. K.; Khang, G.; Cho, S. H.

Diethylenetriaminepentaacetic Acid−Gadolinium (DTPA-Gd)-Conjugated Polysuccinimide Derivatives as Magnetic Resonance Imaging Contrast Agents. *Bioconjugate Chem.* 2006, 17 (3), 700–706.

(11) Yin, N.; Wang, Y.; Cao, Y.; Huang, Y.; Jin, L.; Zhang, S.; et al. A Biodegradable Nanocapsule for Through-Skull NIR-II Fluorescence Imaging/Magnetic Resonance Imaging and Selectively Enhanced Radio-Chemotherapy for Orthotopic Glioma. *Nano Today* 2022, 46, 101619.

(12) Lv, Z.; Jin, L.; Cao, Y.; Zhang, H.; Xue, D.; Yin, N.; et al. A Nanotheranostic Agent Based on Nd^{3+}-Doped YVO_4 with Blood-Brain-Barrier Permeability for NIR-II Fluorescence Imaging/Magnetic Resonance Imaging and Boosted Sonodynamic Therapy of Orthotopic Glioma. *Light: Sci. Appl.* 2022, 11 (1), 116.

(13) Zhao, Z.; et al. Engineering the Infrared Luminescence and Photothermal Properties of Double-Shelled Rare-Earth-Doped Nanoparticles for Biomedical Applications. *ACS Biomater. Sci. Eng.* 2019, 5 (8), 4089–4101.

(14) Yin, N.; Wang, Y.; Huang, Y.; Cao, Y.; Jin, L.; Liu, J.; et al. Modulating Nanozyme-Based Nanomachines via Microenvironmental Feedback for Differential Photothermal Therapy of Orthotopic Gliomas. *Adv. Sci.* 2023, 10 (3), 2204937.

(15) Pei, P.; Chen, Y.; Chen, X.; Zhang, F.; Liu, X.; Wang, J. W. Optothermal-Stimulated Persistent Luminescence Imaging and Therapy (OSPLIT). *Adv. Mater.* 2025, Early View, 2500769.

(16) Ruan, G.; Ye, L.; Ke, J.; et al. All-In-One Gadolinium–Doxorubicin Nanoassemblies for Spatial Delivery and Chemoresistance Reversal in Tumor

Microenvironments. *ACS Appl. Mater. Interfaces* 2025, 17 (13), 19348–19366.

(17) Wang, X.; Liu, Q.; Bu, Y.; Liu, C. S.; Liu, T.; Yan, X. Optical Temperature Sensing of Rare-Earth Ion Doped Phosphors. *RSC Adv.* 2015, 5 (105), 86219–86236.

(18) Luo, L.; Han, H.; Feng, D.; Lv, W.; Chen, L.; Li, L.; et al. Nanocrystalline High Entropy Alloys with Ultrafast Kinetics and High Storage Capacity for Large-Scale Room-Temperature-Applicable Hydrogen Storage. *Renewables* 2024, 2 (2), 138–149.

(19) Serrano, D.; Kuppusamy, S. K.; Heinrich, B.; Fuhr, O.; Hunger, D.; Ruben, M.; Goldner, P. Ultra-Narrow Optical Linewidths in Rare-Earth Molecular Crystals. *Nature* 2022, 603 (7900), 241–246.

(20) Huang, L.; Ming, J.; Wang, Z.; Wu, J.; Yun, B.; Liang, A.; et al. Noninvasively Real-Time Monitoring In-Vivo Immune Cell and Tumor Cell Interaction by NIR-II Nanosensor. *Adv. Mater.* 2025, Early View, 2420329.

(21) Pagano, G.; Guida, M.; Tommasi, F.; Oral, R. Health Effects and Toxicity Mechanisms of Rare Earth Elements—Knowledge Gaps and Research Prospects. Ecotoxicol. *Environ. Saf.* 2015, 115, 40–48.

(22) Hamaguchi, H.; Iwata, K. *Raman Spectroscopy*; Kodansha: Tokyo, 2015.

(23) Udagawa, Y.; Mikami, N.; Kaya, K.; Ito, M. Absolute Intensity Ratios of Raman Lines of Benzene and Ethylene Derivatives with 5145 Å and 3371 Å Excitation. *J. Raman Spectrosc.* 1973, 1 (4), 341–346.

(24) Albrecht, A. C.; Hutley, M. C. On the Dependence of Vibrational Raman Intensity on the Wavelength of Incident Light. *J. Chem. Phys.* 1971, 55 (9), 4438–4443.

(25) Itoh, T.; Procházka, M.; Dong, Z.-C.; Ji, W.; Yamamoto, Y. S.; Zhang, Y.; Ozaki,

Y. Toward a New Era of SERS and TERS at the Nanometer Scale: From Fundamentals to Innovative Applications. *Chem. Rev.* 2023, 123 (4), 1552–1634.

(26) Yamamoto, Y. S.; Itoh, T. Why and How Do the Shapes of Surface-Enhanced Raman Scattering Spectra Change? Recent Progress from Mechanistic Studies. *J. Raman Spectrosc.* 2016, 47 (1), 78–88.

(27) Nie, S.; Emory, S. R. Probing Single Molecules and Single Nanoparticles by Surface-Enhanced Raman Scattering. *Science* 1997, 275 (5303), 1102–1106.

(28) Fleischmann, M.; Hendra, P. J.; McQuillan, A. J. Raman Spectra of Pyridine Adsorbed at a Silver Electrode. *Chem. Phys. Lett.* 1974, 26 (2), 163–166.

(29) Itoh, T.; Yoshida, K.; Biju, V.; Kikkawa, Y.; Ishikawa, M.; Ozaki, Y. Second Enhancement in Surface-Enhanced Resonance Raman Scattering Revealed by an Analysis of Anti-Stokes and Stokes Raman Spectra. *Phys. Rev. B* 2007, 76 (8), 085405.

(30) Yoshida, K. I.; Itoh, T.; Tamaru, H.; Biju, V.; Ishikawa, M.; Ozaki, Y. Quantitative Evaluation of Electromagnetic Enhancement in Surface-Enhanced Resonance Raman Scattering from Plasmonic Properties and Morphologies of Individual Ag Nanostructures. *Phys. Rev. B* 2010, 81 (11), 115406.

(31) Albrecht, A. C. On the Theory of Raman Intensities. *J. Chem. Phys.* 1961, 34 (5), 1476–1484.

(32) Kesharwani, M. K.; Brauer, B.; Martin, J. M. L. Frequency and Zero-Point Vibrational Energy Scale Factors for Double-Hybrid Density Functionals (and Other Selected Methods): Can Anharmonic Force Fields Be Avoided? *J. Phys. Chem. A* 2014, 119 (9), 1701–1714.

(33) Kashinski, D. O.; Chase, G. M.; Nelson, R. G.; Di Nallo, O. E.; Scales, A. N.; VanderLey, D. L.; Byrd, E. F. C. Harmonic Vibrational Frequencies: Approximate Global Scaling Factors for TPSS, M06, and M11 Functional Families Using Several Common Basis Sets. *J. Phys. Chem. A* 2017, 121 (11), 2265–2273.

(34) Leonard, J.; Haddad, A.; Green, O.; Birke, R. L.; Kubic, T.; Kocak, A.; Lombardi, J. R. SERS, Raman, and DFT Analyses of Fentanyl and Carfentanil: Toward Detection of Trace Samples. *J. Raman Spectrosc.* 2017, 48 (10), 1323–1329.

(35) Ahuja, T.; Chaudhari, K.; Paramasivam, G.; Ragupathy, G.; Mohanty, J. S.; Pradeep, T. Toward Vibrational Tomography of Citrate on Dynamically Changing Individual Silver Nanoparticles. *J. Phys. Chem. C* 2021, 125 (6), 3553–3566.

(36) Polavarapu, P. L. Ab Initio Vibrational Raman and Raman Optical Activity Spectra. *J. Phys. Chem.* 1990, 94 (21), 8106–8112.

(37) Liu, Z.; Lu, T.; Chen, Q. Vibrational Spectra and Molecular Vibrational Behaviors of All-Carboatomic Rings, Cyclo[18]Carbon and Its Analogues. *Chem. Asian J.* 2020, 16 (1), 56–63.

(38) Cheeseman, J. R.; Frisch, M. J. Basis Set Dependence of Vibrational Raman and Raman Optical Activity Intensities. *J. Chem. Theory Comput.* 2011, 7 (10), 3323–3334.

(39) Dolg, M.; Cao, X. Relativistic Pseudopotentials: Their Development and Scope of Applications. *Chem. Rev.* 2011, 112 (1), 403–480.

(40) Grand, J.; Auguié, B.; Le Ru, E. C. Combined Extinction and Absorption UV–Visible Spectroscopy as a Method for Revealing Shape Imperfections of Metallic Nanoparticles. *Anal. Chem.* 2019, 91 (22), 14639–14648.

(41) *The Spectroscopy of the Visible and Ultraviolet Regions*; The Spectroscopic Society of Japan (Ed.); Kodansha: Tokyo, 2009.

(42) Savitzky, A.; Golay, M. J. E. Smoothing and Differentiation of Data by Simplified Least Squares Procedures. *Anal. Chem.* 1964, 36 (8), 1627–1639.

Chapter 3: SERS-Based classification of La^{3+} and Gd^{3+} Ions

3.1 Chapter overview

In this study, surface-enhanced Raman scattering (SERS) spectra of different lanthanide (Ln) ion-citrate complexes were investigated for the first time for the qualitative classification of Ln^{3+} ions. With the addition of Ln^{3+} ions to citrate-capped silver nanoparticles in aqueous solutions, the Raman signals of Ln-citrate complexes were enhanced, and characteristic peaks appeared near 1065 cm^{-1} and 1315 cm^{-1}. The I_{1065}/I_{1315} ratios of La-citrate and Gd-citrate were approximately 1 and 0.55, respectively. Thus, different Ln^{3+} ions were classified based on the ratio of characteristic SERS peaks near 1065 cm^{-1} and 1315 cm^{-1}. In addition, the effects of Ln^{3+} ions in the Ln-citrate complexes were analyzed based on density functional theory (DFT) calculations. Calculation results show that these characteristic peaks are attributed to the coordination of the C-O bond and COO^- groups of citrates with the Ln^{3+} ions, suggesting that these are spin-state-related bands of these two Ln-citrate complexes.

3.2 Background and research objectives

Owing to their unique 4f electronic configuration, lanthanide (Ln) elements show similar chemical properties, although they have unique physical properties, e.g. spin, electric, and optical characteristics [1]. When Ln^{3+} ions are combined with small molecules to form complexes, these complexes also exhibit such properties, showing differences in luminescence [2-4] and magnetism [3-4], therefore, Ln^{3+} ion-molecule

complexes have a wide range of applications such as phosphors[5], contrast agents[6], single-molecule magnets[7], and bio-probes for theranostics [8]. They can also be used to produce light-matter interfaces at the quantum level to archive quantum calculations[9]. Standard analytical techniques like NMR spectroscopy, ESR spectroscopy, fluorescence spectroscopy, and multi-modality theranostics are powerful methods for studying the function and action of Ln^{3+} ion-molecule complexes[2-10]; however, these methods are inextricably linked to complex sample preparation processes and it is difficult to measure specific characteristic signals when the sample is mixed with different Ln^{3+} ions[10]. Raman spectroscopy is a nondestructive analytical detection technique by which one can obtain stable molecular fingerprint features, such as molecular structure information[11] and spin information[12][13]. The use of noble metal nanostructures as Raman substrates significantly enhances the Raman signal, enabling the detection of analytes at low concentrations ($<10^{-5}$M) even in single-molecule detection in aqueous solutions[14]. This phenomenon is called surface-enhanced Raman scattering (SERS)[15-17]. In the SERS process, the enhancement of the Raman signal is mainly due to localized surface plasmon resonance (LSPR), which is generated by collective oscillations of conduction electrons in noble metal nanoparticles[18][19]. Furthermore, charge transfer between the noble metal and molecules attached to the metal is also an important mechanism of SERS enhancement, known as the chemical mechanism[20]. Thus, SERS has the potential to be used to study Ln-molecule complex systems in terms of Ln^{3+} ion detection, functional characterization of complexes, and optical signal modulation.

However, SERS studies of Ln^{3+} ions remain challenging because of the similarities in the chemical properties of Ln^{3+} ions. Researches on Ln^{3+} ions in the field of SERS have focused on studying the effects of individual Ln^{3+} ions rather than identifying Ln elements, such as adding Nd^{3+} ions to study the enhancement mechanism of semiconductor SERS substrates[21], fabricating Gd-fluorescent complexes for MRI-SERS multimodal detection[22], and exploring the fluorescence enhancement mechanisms of individual Ln elements[23][24]. SERS studies of Ln's effect remain limited owing to the difficulty of Ln^{3+} ion measurements; for example, the addition of Gd^{3+} ions to the SERS substrate produces a stronger SERS signal[25], but it is not certain whether the addition of other Ln^{3+} ions also results in a stronger SERS signal. Moreover, the fluorescence background of some Ln^{3+} ions e.g. Pr^{3+}, Sm^{3+}, and Eu^{3+} [26], may interfere with the SERS signals; therefore, extracting the characteristic signals which are related to the special physical properties of Ln^{3+} ions from the SERS spectra of Ln-molecule complexes is also challenging. Moreover, the mechanism by which spin-state differences affect the SERS spectra is not clear. Although some previous studies [12][13] have achieved building the spin-state effects model for SERS/Raman of metmyoglobin complex including Fe^{2+} or Fe^{3+} ions, this process appears to be influenced by the coordination conditions of the ligand and metmyoglobin, therefore, the core mechanisms underlying the spin-state properties should be further investigated.

In this study, we selected two non-fluorescent Ln^{3+} ions, La^{3+} and Gd^{3+}, to investigate the spin-state effect of Ln^{3+} ions on the enhancement and characteristic

differences of SERS spectra. The advantage of this Ln-citrate system is that La^{3+} and Gd^{3+} do not exhibit absorption and fluorescence in the visible light region[26],enabling us to realize conventional SERS effect, not surface-enhanced resonance Raman scattering (SERRS). Ln-citrate complexes were evaluated by SERS using citrate-capped silver nanoparticles (citrate@AgNPs), which are well-known SERS substrates for application in the visible-light region[27] then we found the SERS spectral differences that enabled the identification of La^{3+} and Gd^{3+}. These differences in SERS spectra may be attributed to the spin state differences of La^{3+} and Gd^{3+} because the chemical properties of La^{3+} and Gd^{3+} are similar but La^{3+} has no spin, and Gd^{3+} has the highest spin state due to their special 4f electronic configurations, i.e., 0 and 7 electrons in 4f orbital, respectively. These results will be beneficial for future studies on the identification of Ln elements by SERS, and potentially provide new insights into the effect of 4f electronic configuration differences in Ln elements on SERS spectra.

3.3 Experimental and computational methods

Solvent and chemicals. Ultrapure water produced on a Direct-Q® UV 3 system (Millipore, USA) was used as the solvent. A HNO_3 (1.38g/mL, Kanto Chemical Co., Inc, Japan) solution was used to prepare 1 M HNO_3 solution. 0.2 M $Ln(NO_3)_3$ (Ln: La, Gd) solutions were obtained by dissolving an appropriate amount of Ln oxides, i.e., La_2O_3 and Gd_2O_3 (≥99.9%, FUJIFILM Wako Pure Chemical Corporation, Japan) using 1 M HNO_3 solution by heating at 100 ℃, and 2×10^{-3}M $Ln(NO_3)_3$ solutions were obtained by diluting 0.2 M $Ln(NO_3)_3$ solutions with ultrapure water. Citrate@AgNPs were prepared using the Lee & Meisel method[28] with slight improvements. Briefly,

0.03 g of silver nitrate (FUJIFILM Wako Pure Chemical Corporation, Japan) and 0.03 g of trisodium citrate (FUJIFILM Wako Pure Chemical Corporation, Japan) were added to 150 mL of boiling ultrapure water, heated, and stirred at 150 °C in the oil bath for an hour. When the solution turned gray-green, heating was stopped, and the solution was allowed to cool naturally to room temperature to obtain a solution of citrate@AgNPs. The citrate@AgNPs solution was stored away from light in a refrigerator at 4°C.

Characterization. Raman samples were prepared by heating and dissolving 0.01 g of trisodium citrate in 50 mL of water, and then mixing trisodium citrate solution (7.75×10^{-4}M, 1 mL), and $Ln(NO_3)_3$ solution (2×10^{-3}M, 50 μL) to prepare a 10^{-4} M Ln-citrate solution. Samples for SERS measurements were obtained by adding 50 μL of 2×10^{-3}M $Ln(NO_3)_3$ solutions to separate 1 mL solutions of citrate@AgNPs. The concentrations of Ln-citrate complexes were 1×10^{-4}M for each Ln-citrate@AgNPs sample. The original citrate@AgNP colloidal solution without any ions or salt addition was also used for the SERS measurement as a blank experiment to analyze the potential effect of Ln^{3+} ions on the SERS substrate. Note that the original citrate@AgNP solution is considered to contain independent AgNPs without aggregations, therefore SERS signal obtained was weaker than other samples due to the lack of SERS hotspots. All samples' pH was measured using pH test strips (REF 92150 and REF 92140; MACHERY-NAGEL, USA), and their pH was approximately 7.0. All sample solutions were stored at room temperature for 12 hours prior to spectroscopic measurements.

For UV-Vis measurements, ultrapure water was added to each SERS sample to obtain a 10-fold dilution of the sample solutions then the UV-Vis measurements were

performed using a V-770 spectrometer (JASCO, Japan) with a polystyrene cuvette having a light path of 1 cm. Ultrapure water was used as the blank to measure the UV-Vis spectra.

For Raman and SERS measurements, a clean soda glass capillary was used to hold the sample solution for Raman and SERS spectroscopic measurements which were performed using a T64000 Raman spectrometer (Horiba Scientific, Japan). Under this process, the measurements were conducted on multiple AgNPs, i.e., multi-particle SERS. The consistency of the SERS measurements at each measuring point was checked by comparing three independent SERS measurements. All Raman and SERS spectra were collected using lasers at wavelengths of 488 nm and 532 nm with a power level of 50 mW and a 90× objective (0.75 N.A.) that when characterizing the samples with 488 nm and 532 nm lasers, the energy powers at the sampling point were 101 and 85 mW μm^{-2}, respectively. To avoid damage to the sample by high-power laser exposure and to obtain reproducible spectra, the exposure time of Raman and SERS measurements was 30 seconds and the accumulation was 2. Raman shift was corrected by indene.

To perform spectra fitting and baseline subtraction for all experimental spectra, the OriginPro 2022 (OriginLab Corporation, Northampton, MA, USA.) software was used. First, a cubic function was employed for the baseline subtraction process. After baseline subtraction, the Savitzky-Golay method was used for noise reduction twice with setting as 11 points of windows and polynomial order was 1. After completing the noise reduction, we removed the baseline again using minimum constant mode from

the denoised data.

Computational Methods and Details The SERS simulations of Ln-citrate complexes on the silver surface were performed using the following simplified model: according to Ref 29, the structures of Ln-citrate complexes were modeled as $LnCit^-$ based on the structure of trisodium citrate which was downloaded from the Cambridge Crystallographic Data Centre (CCDC, http://www.ccdc.cam.ac.uk). An appropriate-sized Ag surface formed by 11 Ag atoms was cut from a bulk Ag crystal along the (111) plane[30] to mimic the facets of the silver surface, whose size is close to $LnCit^-$.

Further, geometry optimization and vibrational spectra calculations were performed based on density functional theory (DFT) using Gaussian 16 software (Revision C.01, Gaussian, Inc., Wallingford CT, USA). The commonly used B3LYP functional is not suitable for describing transition metals[31]. Therefore, the PBE0 functional[32] was used with the addition of DFT-D3(BJ) dispersion correction[33] for all calculations to better describe the 4f electronic configuration of Ln elements[34][35]. The solvent was considered as water using SMD model to match the experimental parameters. The aug-cc-pvdz [36] basis set was adopted C, H, O, and Na. In contrast, Ag and Ln elements were described by the def2svpd[37] and def2tzvpd[38][39] basis sets, respectively, and all were associated by relativistic pseudopotentials[40] to correct relativistic effect during calculations. The scaling factors for PBE0-D3(BJ)/aug-cc-pvdz and PBE0-D3(BJ)/def2tzvpd; were 0.956 and 0.971, respectively, as obtained from the literatures[41][42]. The calculation results of SERS spectra in the region of $1000 - 1700\ cm^{-1}$ were scaled by scaling factor 0.956 and in the region of $1000 - 1250$

cm^{-1}, spectra were scaled by scaling factor 0.971 again to scale Ln^{3+} ions' effect. The widths of all simulated SERS spectra were set to 50 cm^{-1} to approximate the experimental spectra. All energy calculations of the Ln-citrate complexes were performed at the PBE0-D3(BJ)/def2tzvpp[43] level. All calculation results were analyzed using the Multimfn software[44], including Raman analysis and spin analysis. Gaussian 16 directly calculates the Raman activity of each vibrational mode. The distribution of unpaired electrons can be described by spin population analysis by using Multimfn. The Visual Molecular Dynamics (VMD) software [45] was used to observe the structure and spin distribution.

3.4 Data processing of experimental and simulated results

For the spectral fitting and baseline subtraction of all experimental spectra, we systematically utilized OriginPro 2022 software from OriginLab Corporation, U.S.A. Initially, we removed the baseline from the raw experimental data, then performed noise reduction and finally removed the baseline again. For the first baseline removal, we manually selected appropriate points to ensure that the starting and ending points of all broadband spectra were at a consistently relative intensity, as shown in Figure 3.1(a). A cubic function was chosen for the baseline subtraction process. To reduce noise, we applied the Savitzky-Golay smoothing method twice, using a 11-point window and a 1-order polynomial. After the noise reduction, we removed the baseline again using the minimum constant mode from the denoised data as required, as shown in Figure 3.1(b).

Then, Raman shifts of all spectra were fixed by indene.

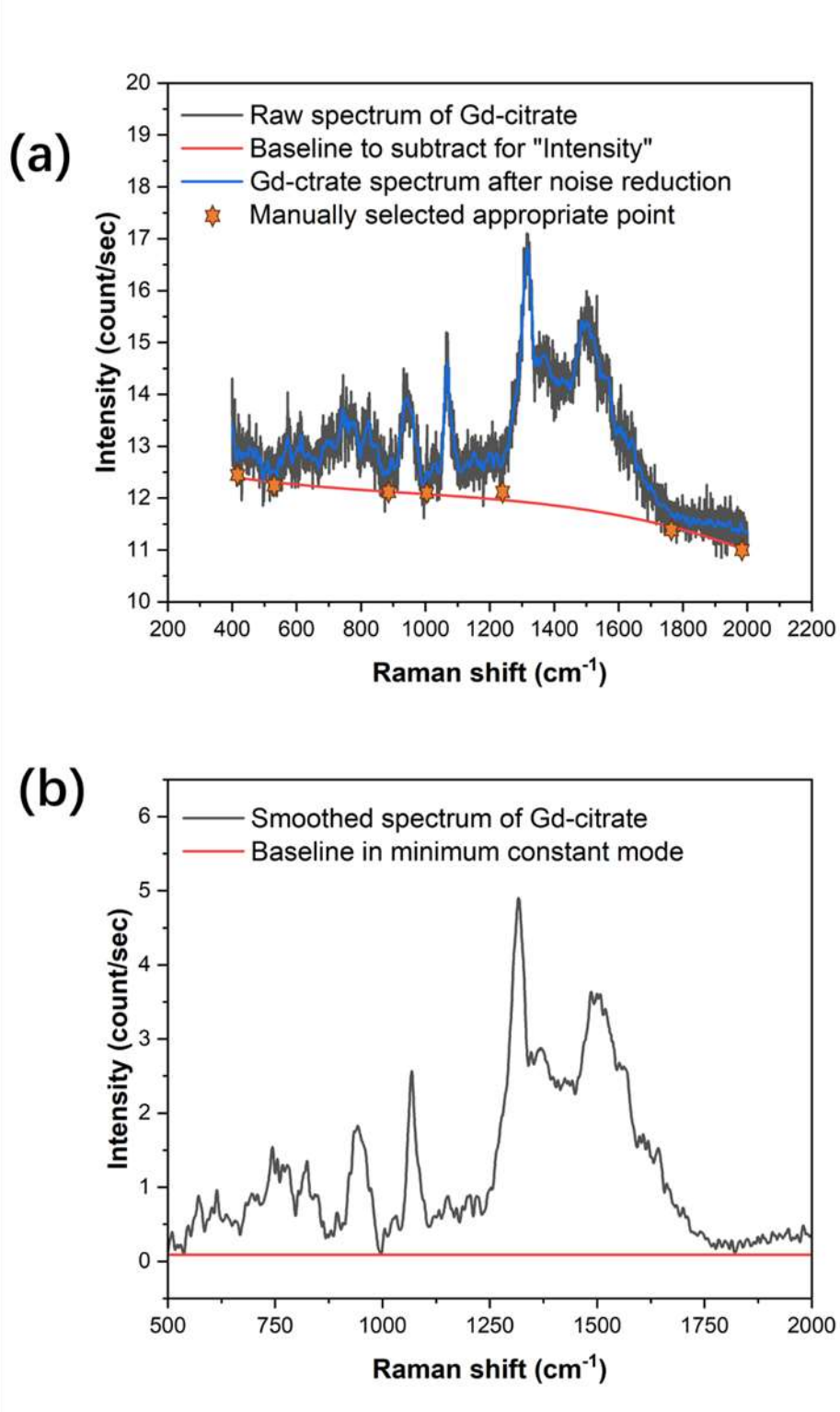

Figure 3.1. (a) Raw spectrum of Gd-citrate (black line), its baseline (red line) and Gd-citrate spectrum after noise reduction (blue line). The orange stars are manually selected as the minimum points of the spectrum used for creating the baseline. (b) Smoothed spectrum of Gd-citrate and baseline in the minimum constant mode.

3.5 Trial of improving the quality of the spectra

In our present study, the low signal-noise ratio of our experimental data is the issue. To address this, we have made efforts to employ the longer exposure time to reduce the noise level as shown in Figures 3.2 and 3.3 in hopes of enhancing the quality of the spectra obtained.

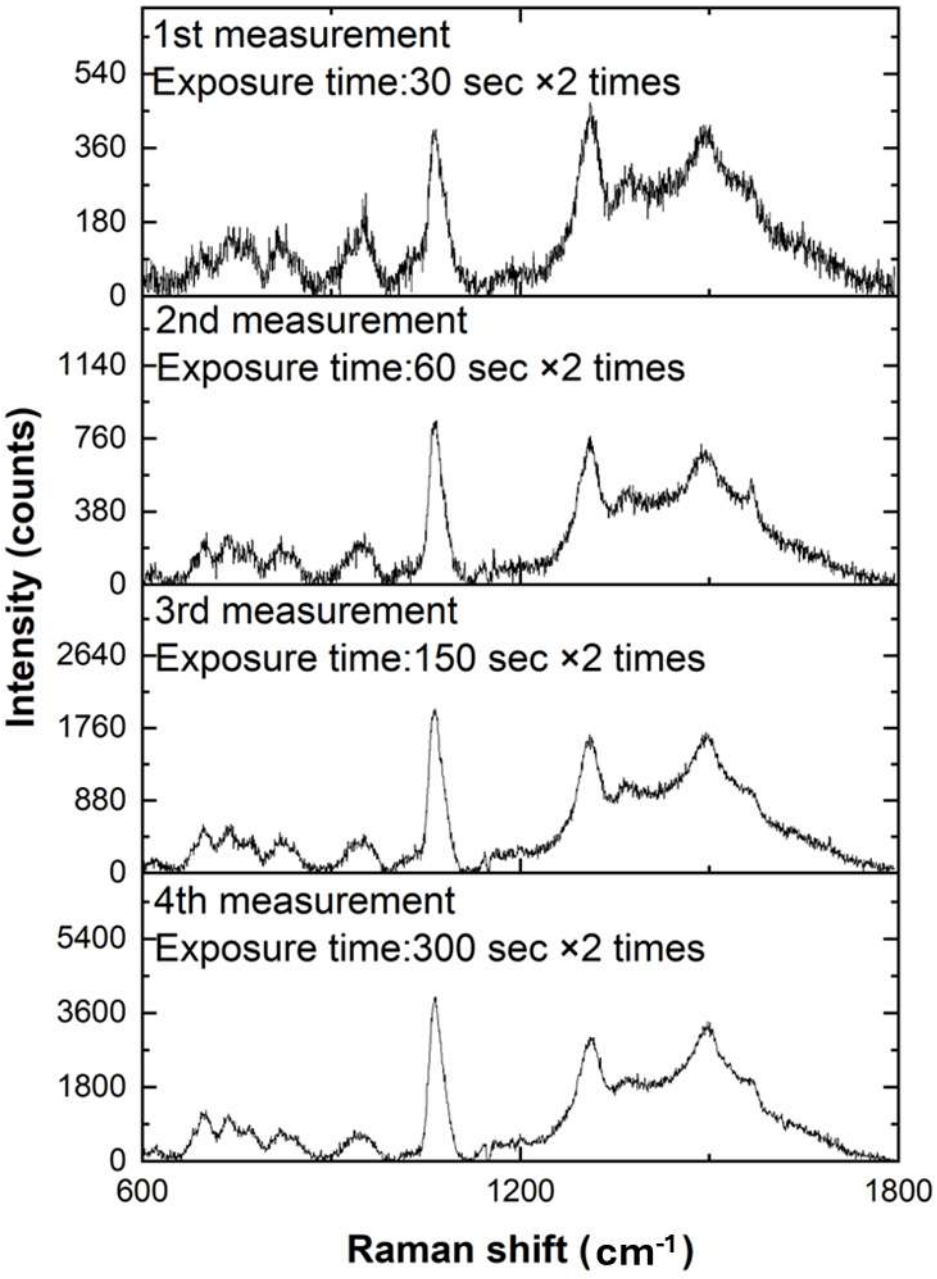

Figure 3.2 SERS measurement of La-citrate with different exposure time

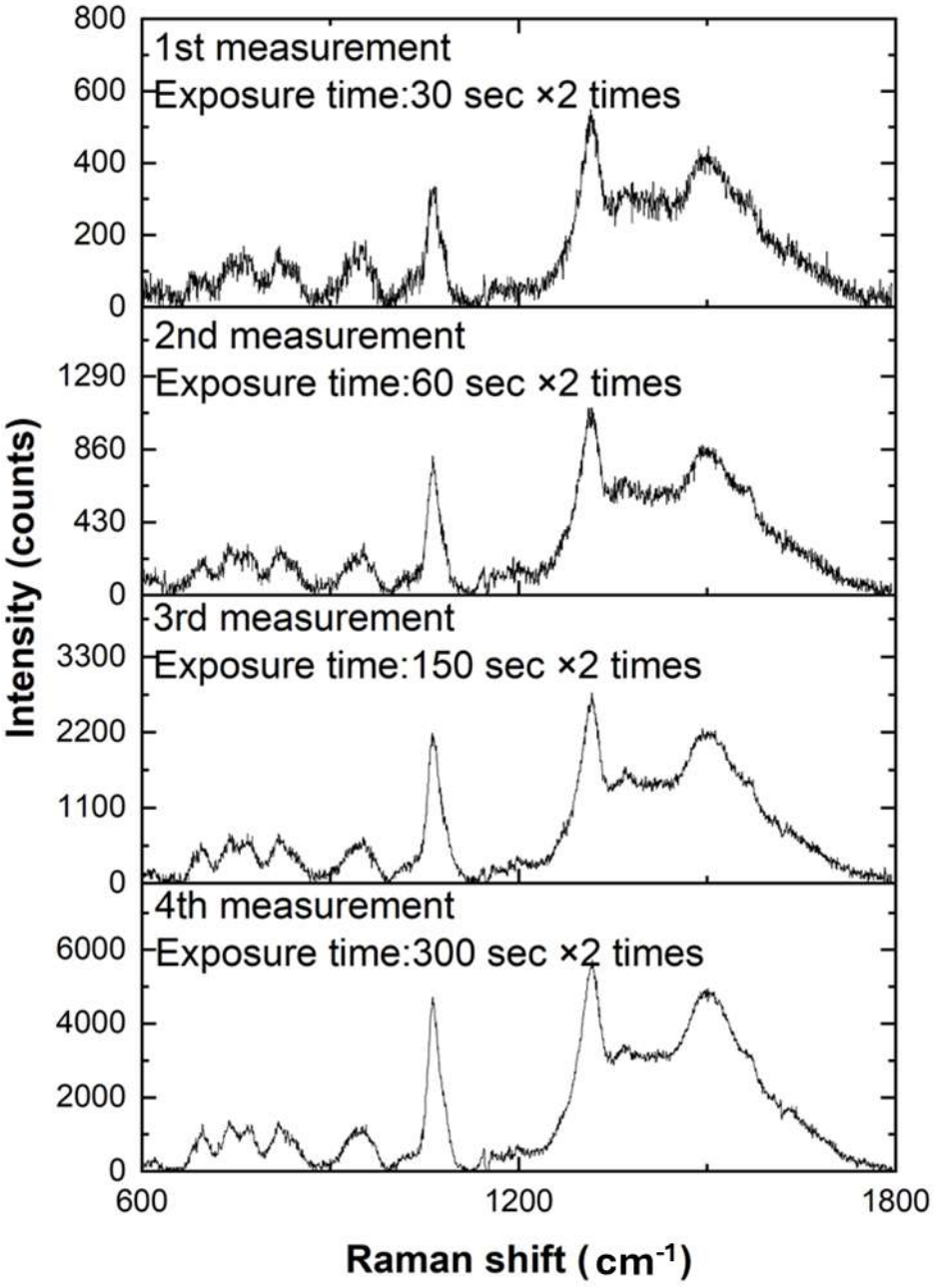

Figure 3.3 SERS measurement of Gd-citrate with different exposure time

Our initial conditions were set with an exposure time of 30 seconds and an accumulation of 2. Upon extending the exposure time to 60, 150, and 300 seconds, we were able to achieve a better signal-to-noise ratio. However, this adjustment led to a

discrepancy in the relative intensity ratio between the peaks at approximately 1065 cm^{-1} and 1315 cm^{-1} compared to those at the original settings of 30 seconds exposure with two accumulations. This observation suggests that prolonged exposure times can influence the Ln-citrate@AgNP system. Therefore, we have determined that the data captured under the original conditions are currently the most accurate for our analysis.

3.6 Peak assignment of Ln-citrate using DFT

We analyzed the simulated SERS spectra of selected Ln-citrate (Ln: La and Gd) to assign the SERS peaks based on each vibrational mode (Tables 3.1 and 3.2). All tables used the same symbols for peak assignment: ν indicates stretching, ν_{sym} is symmetric stretching, ν_{asym} is asymmetric stretching, δ is in-plane bending and rocking, and γ is out-of-plane wagging and twisting. The calculated SERS frequencies were scaled by using scaling factors.

Table 3.1 The vibrational modes contained in each simulated SERS peak of La-citrate

Simulated SERS peak (cm^{-1})	Vibrational mode	Frequency (cm^{-1})	Assignment
629	ν_{629}	629	$\delta(COO^-)$
681	ν_{681}	681	$\delta(COO^-)$
712	ν_{712}	712	$\delta(COO^-)+ \gamma(COO^-)$
745	ν_{745}	745	$\delta(COO^-)+ \gamma(COO^-)$
840	ν_{840}	840	ν(CCCC-O)
	ν_{842}	842	ν(CCCC-O)
920	ν_{917}	917	$\nu(C\text{-}COO^-)$
938	ν_{934}	934	$\delta(CH_2)$
	ν_{939}	939	$\delta(CH_2)$
970	ν_{970}	970	$\nu(C\text{-}COO^-)$
1100	ν_{1096}	1096	$\gamma(CH_2)$
	ν_{1102}	1102	ν(C-O···La)
1171	ν_{1170}	1170	$\gamma(CH_2)$
	ν_{1187}	1187	$\gamma(CH_2)$
1211	ν_{1211}	1211	$\gamma(CH_2)$
1327,1344	ν_{1320}	1320	$\delta(CH_2)$
	ν_{1327}	1327	$\nu_{sym}(COO^-)$, $\delta(CH_2)$
	ν_{1347}	1347	$\nu_{sym}(COO^-)$, $\delta(CH_2)$
	ν_{1365}	1365	$\nu_{sym}(COO^-)$, $\delta(CH_2)$
1375	ν_{1375}	1375	$\nu_{sym}(COO^-)$, $\delta(CH_2)$
1473	ν_{1463}	1463	$\nu_{asym}(COO^-)$, $\gamma(CH_2)$
	ν_{1474}	1474	$\nu_{asym}(COO^-)$, $\gamma(CH_2)$
	ν_{1492}	1492	$\nu_{asym}(COO^-)$, $\gamma(CH_2)$

Table 3.2 The vibrational modes contained in each simulated SERS peak of Gd-citrate

Simulated SERS peak (cm^{-1})	Vibrational mode	Frequency (cm^{-1})	Assignment
635	v_{635}	635	$\delta(COO^-)$
684	v_{684}	684	$\delta(COO^-)$
716	v_{716}	716	$\delta(COO^-)+ \gamma(COO^-)$
747	v_{747}	747	$\delta(COO^-)+ \gamma(COO^-)$
844	v_{840}	840	ν(CCCC-O)
	v_{845}	845	ν(CCCC-O)
928	v_{925}	925	$\nu(C\text{-}COO^-)$
	v_{935}	935	$\delta(CH_2)$
	v_{940}	940	$\delta(CH_2)$
975	v_{975}	975	$\nu(C\text{-}COO^-)$
1109	v_{1104}	1104	$\gamma(CH_2)$
	v_{1115}	1115	ν(C-O···Gd)
1174	v_{1174}	1174	$\gamma(CH_2)$
	v_{1197}	1197	$\gamma(CH_2)$
1339	v_{1319}	1319	$\nu_{sym}(COO^-)$, $\delta(CH_2)$
	v_{1334}	1334	$\nu_{sym}(COO^-)$, $\delta(CH_2)$
	v_{1339}	1339	$\nu_{sym}(COO^-)$, $\delta(CH_2)$
	v_{1356}	1356	$\nu_{sym}(COO^-)$, $\delta(CH_2)$
1382	v_{1382}	1382	$\nu_{sym}(COO^-)$, $\delta(CH_2)$
1488	v_{1482}	1482	$\nu_{asym}(COO^-)$, $\gamma(CH_2)$
	v_{1493}	1493	$\nu_{asym}(COO^-)$, $\gamma(CH_2)$
	v_{1523}	1523	$\nu_{asym}(COO^-)$, $\gamma(CH_2)$

3.7 Experimental Raman and SERS spectra of citrate

3.7.1 Spectral features analysis

Figure 3.4 shows a schematic representation of the interaction of Ln^{3+} (Ln: La, Gd) ions with the surfaces of the citrate@AgNPs.

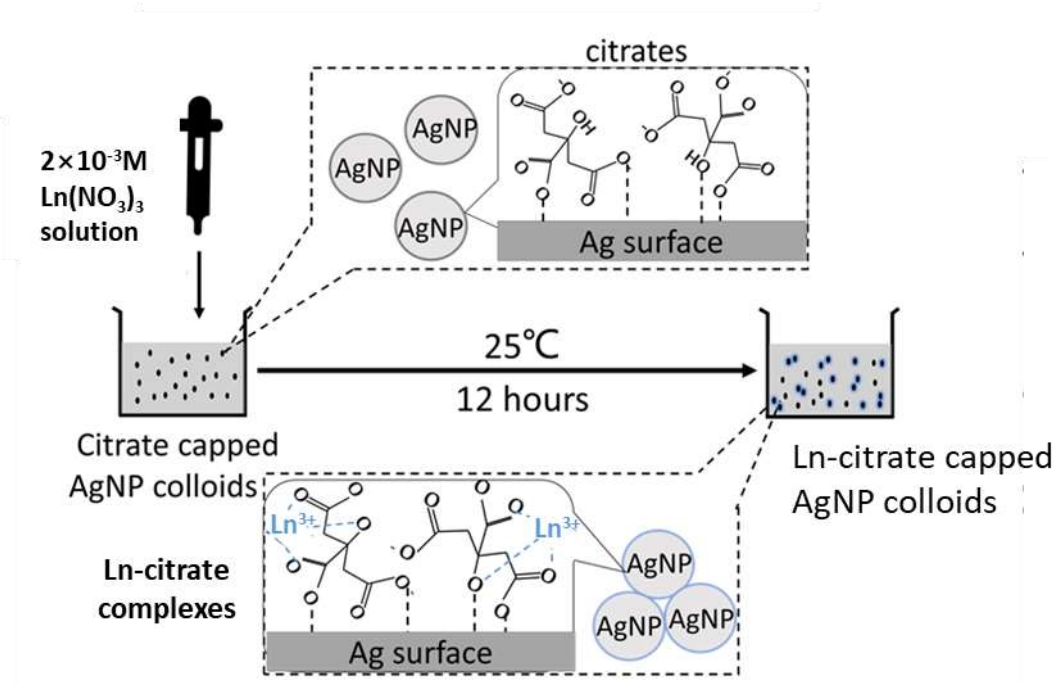

Figure 3.4. A schematic representation of the interaction of Ln^{3+} (Ln: La, Gd) ions with the surfaces of citrate-capped sliver nanoparticles (citrate@AgNPs).

A citrate@AgNPs solution was synthesized by Lee & Meisel method using citrate molecules as a reducing agent[28]; thus, all the AgNP surfaces were covered by citrate molecules[27][46][47]. Therefore, in this manuscript, we refer to AgNPs as citrate-capped AgNPs, namely citrate@AgNPs. Additionally, it's important to note that Ln^{3+} ions typically coordinate with both the hydroxyl and carboxyl groups in citrate to form complexes[29][48]. However, in the formation of $LnCit^{-}$ complexes, the hydroxyl group in citrate releases its hydrogen atom[29]. This leaves solely the C-O bond and COO^{-}

groups available for coordination with the Ln^{3+} ions.

Figure 3.5 shows the differences between the UV-visible extinction spectra of citrate@AgNP colloidal solutions collected before and after the addition of the different $Ln(NO_3)_3$ aqueous solutions.

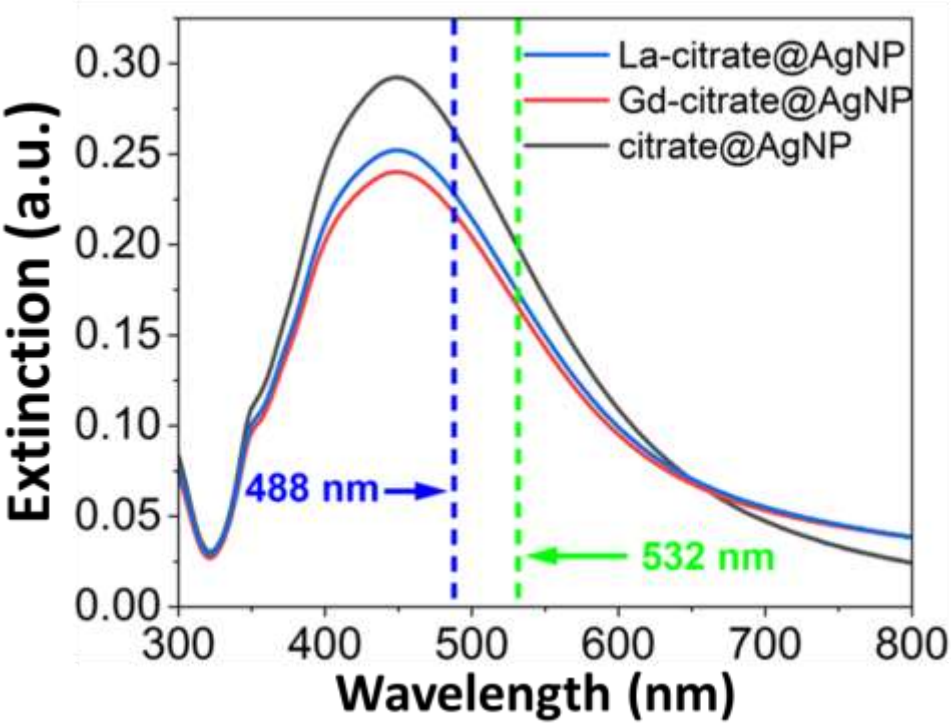

Figure 3.5. UV-Visible extinction spectra of La-citrate@AgNPs, Gd-citrate@AgNPs and citrate@AgNPs.

In this process, Ln^{3+} ions are adsorbed by the citrate on the silver surface and coordinate with the C-O bond and COO^- groups of citrate[29][48] to form a 1:1 Ln-citrate complex[49] at pH=7.0 as main structure as $LnCit^-$[29], possibly resulting in the fabrication of AgNPs aggregates. Usually, the junction of AgNPs aggregates generates a strong electromagnetic field under laser excitation, namely hotspots[50][51]; therefore, we can expect a much stronger Raman signal of Ln-citrate complexes at hotspots between the AgNPs.

As shown in Figure 3.5, on the addition of different Ln^{3+} ions to separate citrate@AgNP colloidal solutions, the UV-visible extinction spectra of the mixtures do not show the change in their peak positions; however, the peak heights are decreased, showing that AgNPs aggregates are fabricated upon addition of Ln^{3+} ions. The extinction peaks of the three samples were all around 450 nm, indicating that the addition of Ln^{3+} ions did not affect the location of the main absorption peaks, and therefore in this study, we chose 488 nm and 532 nm laser light, respectively, as Raman and SERS laser light sources for higher SERS enhancement. A measurement system for Raman and SERS spectra is shown in Figure 3.6, where the data obtained with and without citrate@AgNPs samples at the same measurement parameters are comparable for evaluating the enhancement effect, laser wavelength effects and ions' effects.

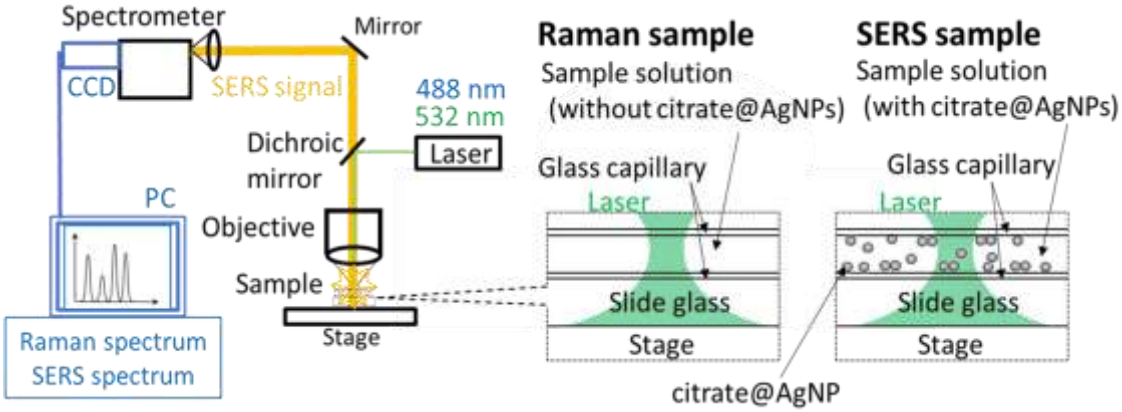

Figure 3.6. A schematic of measurement system for Raman and SERS spectroscopy. Raman and SERS samples were enclosed in a glass capillary, and then their Raman and SERS spectra were measured using 488 nm and 532 nm laser lights, respectively. Here, we defined that Raman samples are solutions without citrate@AgNPs, and SERS samples are those with citrate@AgNP, respectively.

Figures 3.7-3.10 show representative Raman and SERS spectra of the La-citrate and Gd-citrate sample solutions excited at 488 nm or 532 nm, respectively. The Raman

spectra of the samples were collected without citrate@AgNPs in the sample inserted into the glass capillary, while the SERS spectra of the samples were collected with citrate@AgNPs. Without citrate@AgNP, the Raman signals of the Ln-citrate solutions at the same concentration were very weak with no significant signal peaks. Upon addition of citrate@AgNPs in the Ln-citrate solution, the Raman signal collected was stronger than that without citrate@AgNPs, indicating that the existence of citrate@AgNPs enhanced the Raman signal of the Ln-citrate solution, i.e. SERS occurred. For the peak assignments, DFT calculations were introduced along with the results of previous analyses of the literatures [27][52] and were summarized in Tables 3.1-3.3

Table 3.3. Peak assignment for SERS spectrum of La-citrate and Gd-citrate

SERS of La-citrate			SERS of Gd-citrate		
Raman shift (cm^{-1})		Assignment	Raman shift (cm^{-1})		Assignment
Experimental	Simulated		Experimental	Simulated	
617, 697	629, 681	$\delta(COO^-)$	622, 696	635, 684	$\delta(COO^-)$
736, 737, 769, 775	712, 745	$\delta(COO^-)$, $\gamma(COO^-)$	737, 742, 776, 772	716, 747	$\delta(COO^-)$, $\gamma(COO^-)$
822, 825	840	ν(CCCC-O)	818, 822	844	ν(CCCC-O)
937，945	920, 938, 975	$\nu(C\text{-}COO^-)$, $\delta(CH_2)$	937	928, 975	$\nu(C\text{-}COO^-)$, $\delta(CH_2)$
1065，1066	1100	ν(C-O···La), $\gamma(CH_2)$	1065，1066	1109	ν(C-O···Gd), $\gamma(CH_2)$
1309，1314	1327, 1344	$\nu_{sym}(COO^-)$, $\delta(CH_2)$	1313，1315	1339	$\nu_{sym}(COO^-)$, $\delta(CH_2)$
1496, 1500	1473	$\nu_{asym}(COO^-)$, $\gamma(CH_2)$	1495, 1498	1488	$\nu_{asym}(COO^-)$, $\gamma(CH_2)$

Table 3.4. Peak assignment for SERS spectrum of citrate from literatures [27] [52]

Raman Shift (cm^{-1})	Assignment
670[27]	$\delta(COO^-)$
845[52]	ν(CCCC-O)
933[27], 956[52]	$\nu(C\text{-}COO^-)$
1025[27]	ν(C-OH)
1390[27], 1400 [52], 1415[52]	$\nu_{sym}(COO^-)$
1580[52]	$\nu_{asym}(COO^-)$

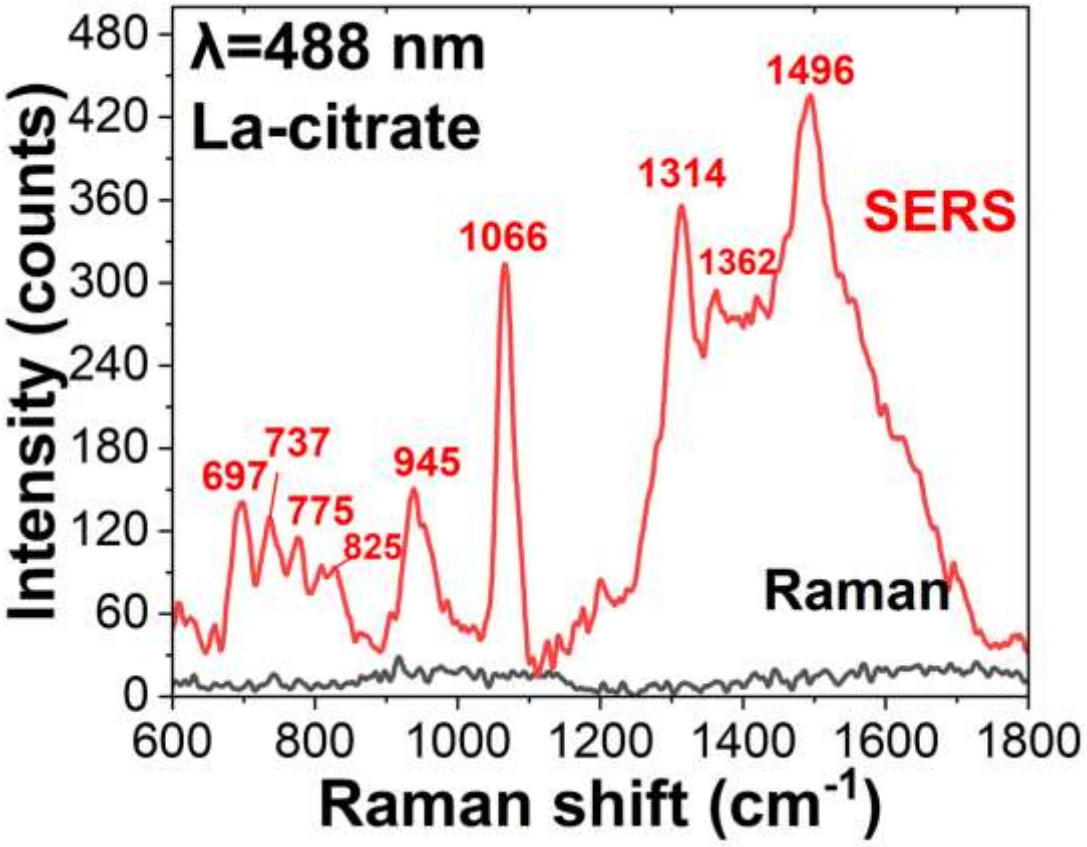

Figure 3.7. Raman (black line) and SERS (red line) spectra of La-citrate excited at 488 nm

In the SERS spectrum of Figure 3.7, there were several inconspicuous peaks between 690 and 900 cm^{-1}, such as peaks at 697, 737, and 775 cm^{-1}, which corresponded to different $\delta(COO^-)$, $\delta(COO^-) + \gamma(COO^-)$ and $\delta(COO^-) + \gamma(COO^-)$. Some inconspicuous peaks near 825 cm^{-1} corresponded to ν(CCCC-O) with lower relative intensities than the peak at 775 cm^{-1}. The peaks at 737 and 775 cm^{-1} exhibited similar relative intensities and were both lower than the peak at 697 cm^{-1}. While other significant Raman peaks appeared at 945, 1066, 1314, and 1496 cm^{-1}, which can in turn be assigned as ν(C-COO^-), ν(C-O···La) + $\gamma(CH_2)$, $\nu_{sym}(COO^-) + \delta(CH_2)$, and $\nu_{asym}(COO^-) + \gamma(CH_2)$.

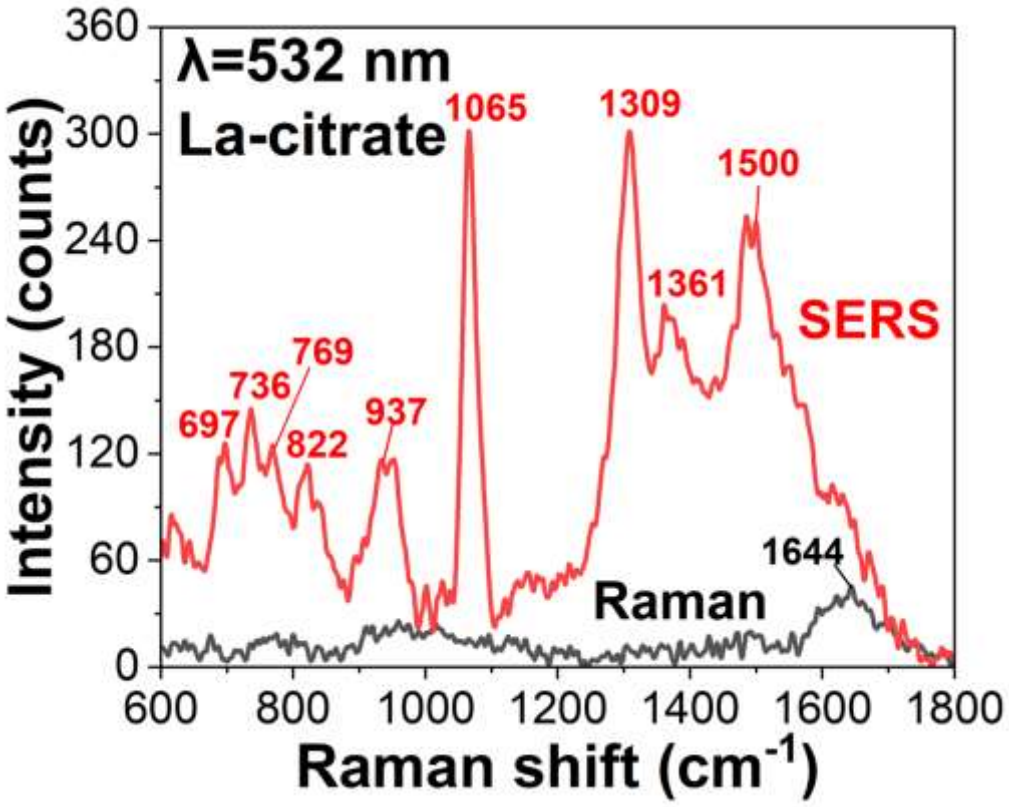

Figure 3.8. Raman (black line) and SERS (red line) spectra of La-citrate excited at 532 nm

Figure 3.8 shows the Raman and SERS spectra of the La-citrate solution excited at 532 nm. The Raman signal of the La-citrate solution collected using the 532 nm laser has one significant Raman peak at 1644 cm^{-1}, potentially exhibiting acetoacetic acid Raman peak due to the thermal decomposition of citrate[27][53]. In the SERS spectrum, the slight difference of some vibration bands compared to the La-citrate's SERS spectrum excited by the 488 nm laser may be related to the signal noise and the influence of laser wavelength. The peaks at 697, 736, and 769 cm^{-1} corresponded to $\delta(COO^-)$ and different $\delta(COO^-) + \gamma(COO^-)$. The peak at 822 cm^{-1} corresponded to ν(CCCC-O) and its relative intensity was close to that of the peak at 937 cm^{-1} but lower than that of peaks at 697, 736, and 769 cm^{-1}. The significant Raman peaks appeared at 937, 1065, and 1309 cm^{-1}, which can in turn be assigned as $\nu(C\text{-}COO^-) + \delta(CH_2)$, $\nu(C\text{-}O\cdots La) + \gamma(CH_2)$ and $\nu_{sym}(COO^-) + \delta(CH_2)$. respectively. The band contains

$\nu_{asym}(COO^-) + \gamma(CH_2)$ was wide and detected around 1500 cm^{-1}.

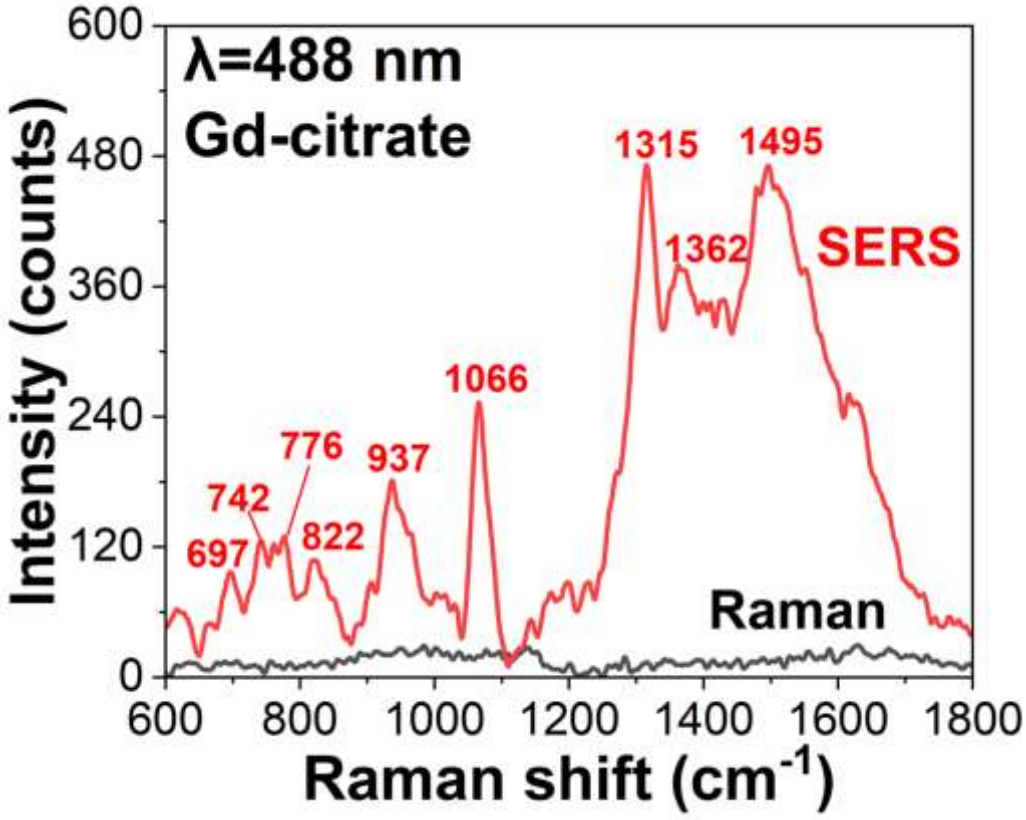

Figure 3.9. Raman (black line) and SERS (red line) spectra of Gd-citrate excited at 488 nm

Figure 3.9 shows representative Raman and SERS spectra of the Gd-citrate solution excited at 488 nm. Similar to the case of La-citrate, when Gd-citrate was used without citrate@AgNPs, the Raman signal was very weak. However, when Gd^{3+} ions were added to citrate@ AgNPs to form Gd-citrate on the surface of the AgNPs, the SERS signal occurred. In the SERS spectrum, several inconspicuous peaks appeared at 697, 742, 776, and 822 cm^{-1}, corresponding $\delta(COO^-)$, $\delta(COO^-) + \gamma(COO^-)$, $\delta(COO^-) + \gamma(COO^-)$ and ν(CCCC-O). The relative intensities of these peaks were lower than the intensities of the peaks near 937 cm^{-1}. And the relative intensities of peaks that appeared at 742 and 776 cm^{-1} were similar. Four significant characteristic peaks were observed at 937, 1066, 1315, and 1495 cm^{-1}, which can in turn be assigned as $\nu(C\text{-}COO^-)$ +

$\delta(CH_2)$, $\nu(C\text{-}O\cdots Gd) + \gamma(CH_2)$, $\nu_{sym}(COO^-) + \delta(CH_2)$, and $\nu_{asym}(COO^-) + \gamma(CH_2)$, respectively. The small differences in positions of each vibration band can be explained by Ln^{3+} ion's differences.

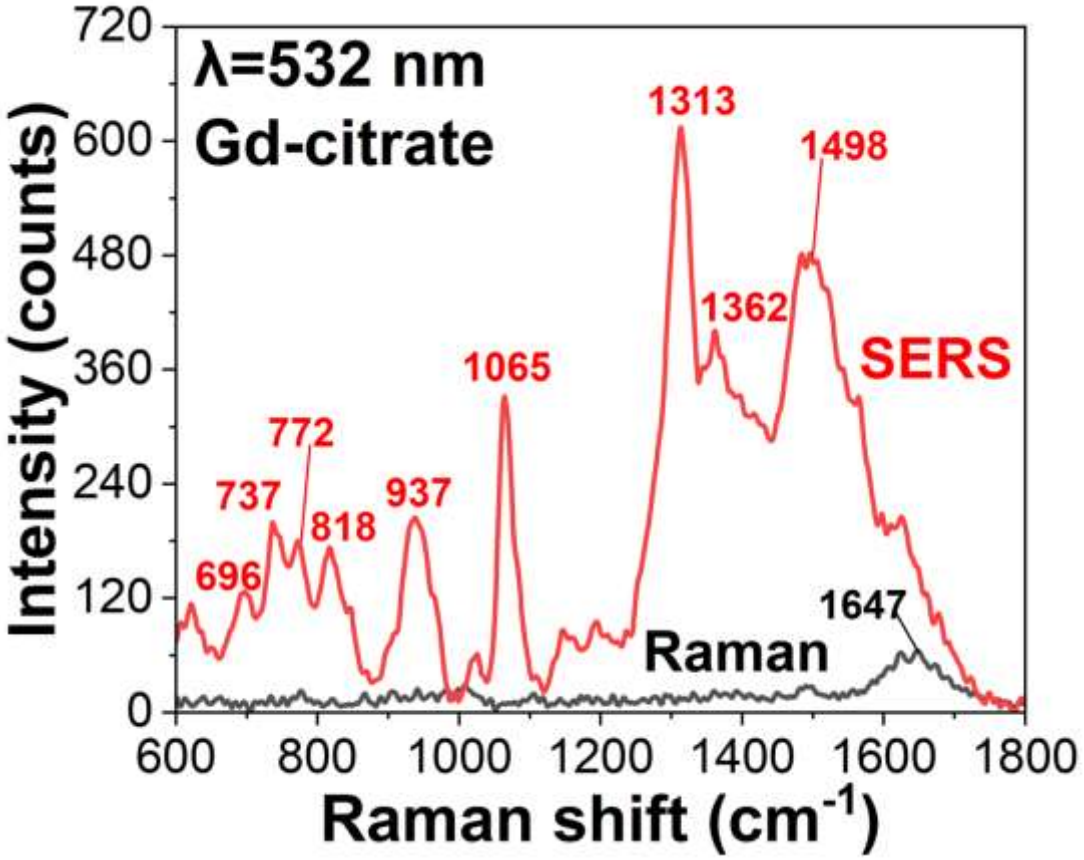

Figure 3.10. Raman (black line) and SERS (red line) spectra of Gd-citrate excited at 488 nm

Figure 3.10 shows the Raman and SERS spectra of Gd-citrate excited at 532 nm. One significant Raman peak was observed at 1647 cm^{-1} and this peak was not observed in the SERS spectrum significantly. In the SERS spectrum, the peaks between 690 and 900 cm^{-1} were observed at 696, 737, 772, and 818 cm^{-1}, respectively. In addition, the intensity of the peak at 737 cm^{-1} was higher than that of the peak at 772 cm^{-1} since these two peaks corresponded to different $\delta(COO^-) + \gamma(COO^-)$. The peak at 818 cm^{-1} was assigned as ν(CCCC-O). Compared with the peak at 937 cm^{-1}, the relative intensities of these three peaks were lower. Other significant SERS characteristic peaks over this

region were observed at 937, 1065, 1313, and 1495 cm^{-1}, assigned as ν(C-COO^-) + $\delta(CH_2)$, ν(C-O···Gd) + $\gamma(CH_2)$, $\nu_{sym}(COO^-)$ + $\delta(CH_2)$, and $\nu_{asym}(COO^-)$ + $\gamma(CH_2)$, respectively.

Notably, compared with the evaluation of the enhancement in the citrate solution without Ln^{3+} ions (Figures 3.11 and 3.12), the Raman signals of citrate solutions with Ln^{3+} ions were significantly enhanced by citrate@AgNPs when the target samples contained Ln^{3+} ions.

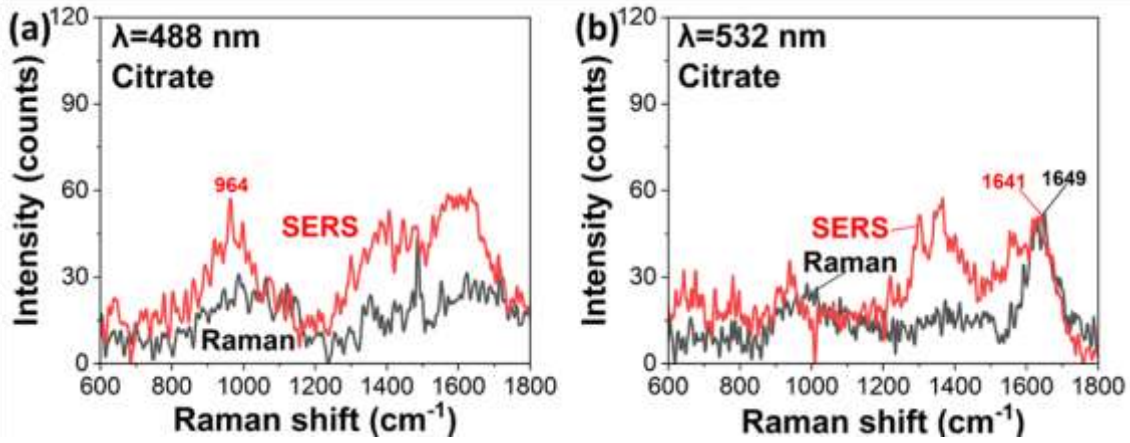

Figure 3.11. Raman (black line) and SERS (red line) spectra of citrate (7.75×10^{-4}M) excited at (a) 488 nm and (b) 532 nm.

Figures 3.11 (a) and (b) show Raman and SERS spectra of citrate excited at 488 nm and 532 nm lasers, respectively. In the SERS spectra of citrate@AgNP, Raman signals of citrate in the region of 800 − 1150 cm^{-1} and 1250 − 1750 cm^{-1} were enhanced under the excitation of 488 nm laser. Under the excitation of 532 nm laser, only the Raman signal of citrate in the region of 1250 − 1750 cm^{-1} was enhanced and some new peaks appeared. Around 1641 cm^{-1}, both Raman and SERS of citrate have an obvious peak.

Figures 3.12(a)-(c) show the dark field images of different SERS samples. Comparing the dark field images of these SERS samples, Ln-citrate@AgNP possessed

larger size particles, indicating that AgNPs aggregated upon the addition of Ln^{3+} ions (Ln: La, Gd). This aggregation creates hotspot regions, significantly enhancing Raman signals. As shown in Figures 3.7-3.11, when target molecules were in the sample solutions at the same concentration, the Raman enhancement of citrate was weak compared to that of Ln-citrate complexes. This difference in Raman enhancement is because citrate@AgNPs do not aggregate sufficiently to form hotspots, which are essential for enhancing Raman signals.

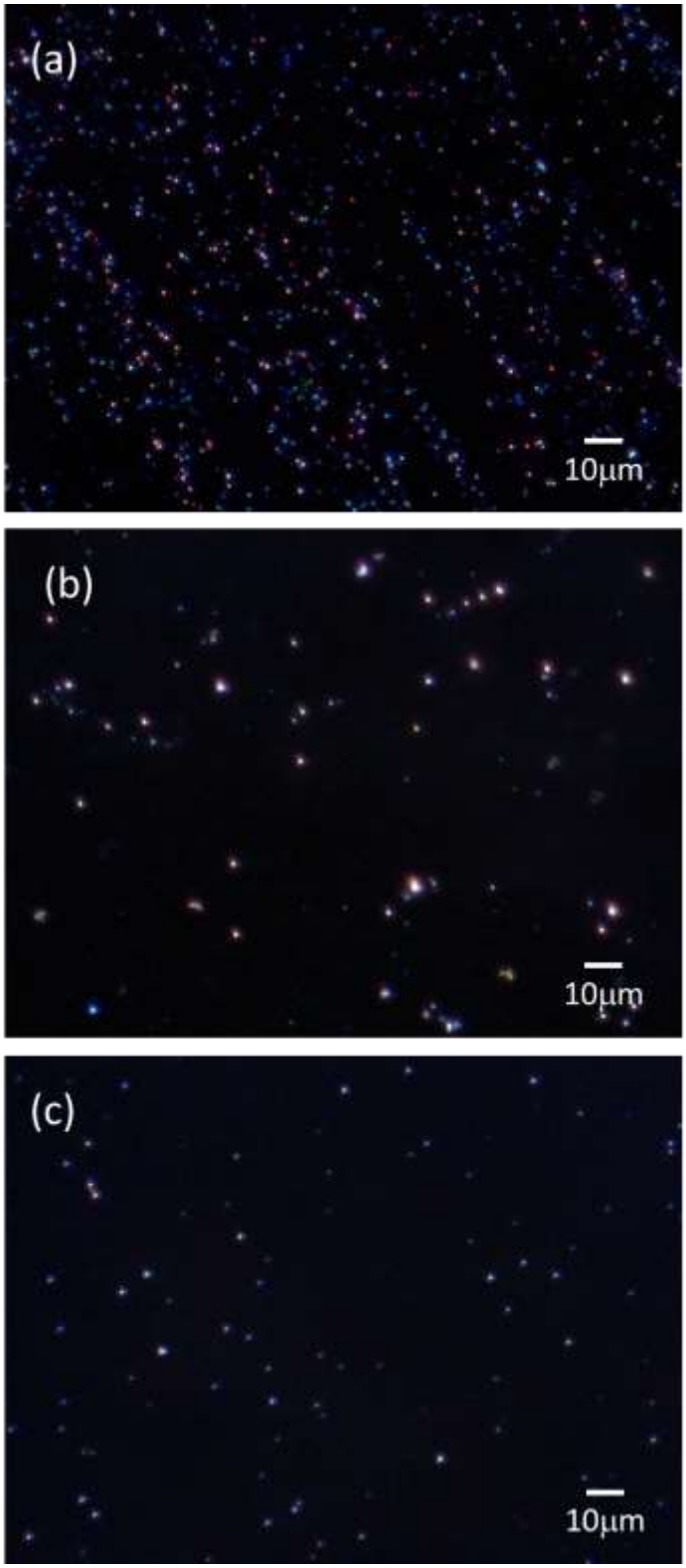

Figure 3.12. Dark field images of (a) citrate@AgNPs, (b) La-citrate@AgNPs and (c) Gd-citrate@AgNPs.

Thus, when comparing the Raman spectrum of citrate with the same concentration and the Raman spectrum of original citrate@AgNPs without adding any ions or salts

(SERS spectrum of citrate), the Raman signal was not significantly enhanced and resulted in almost no SERS peaks in Figure 3.13 were observed. This is due to a lack of aggregation of silver nanoparticles, which could not generate enough hotspots. Therefore, the SERS peak assignment of citrate (citrate@AgNP sample) were done by Raman shift of both Raman and SERS spectra of citrate from literature [27,52].

In addition, peak shifts observed in Figures 3.7-3.10 can be explained by the second enhancement effect in the electromagnetic effect, and the chemical effect[19]. Plasmon resonance variations in the second enhancement effect cause peak positions to fluctuate due to the combined impact of different vibration intensities. In the chemical effect, the resonance effect, mainly from charge transfer (CT) in the chemical bond's orientation, causes variations in SERS spectra, including peak shifts.

3.7.2 Classification of La^{3+} and Gd^{3+}

Further analysis of the experimental SERS spectra in the region of 600 − 1800 cm^{-1} was shown in Figure 3.13 (a) and (b).

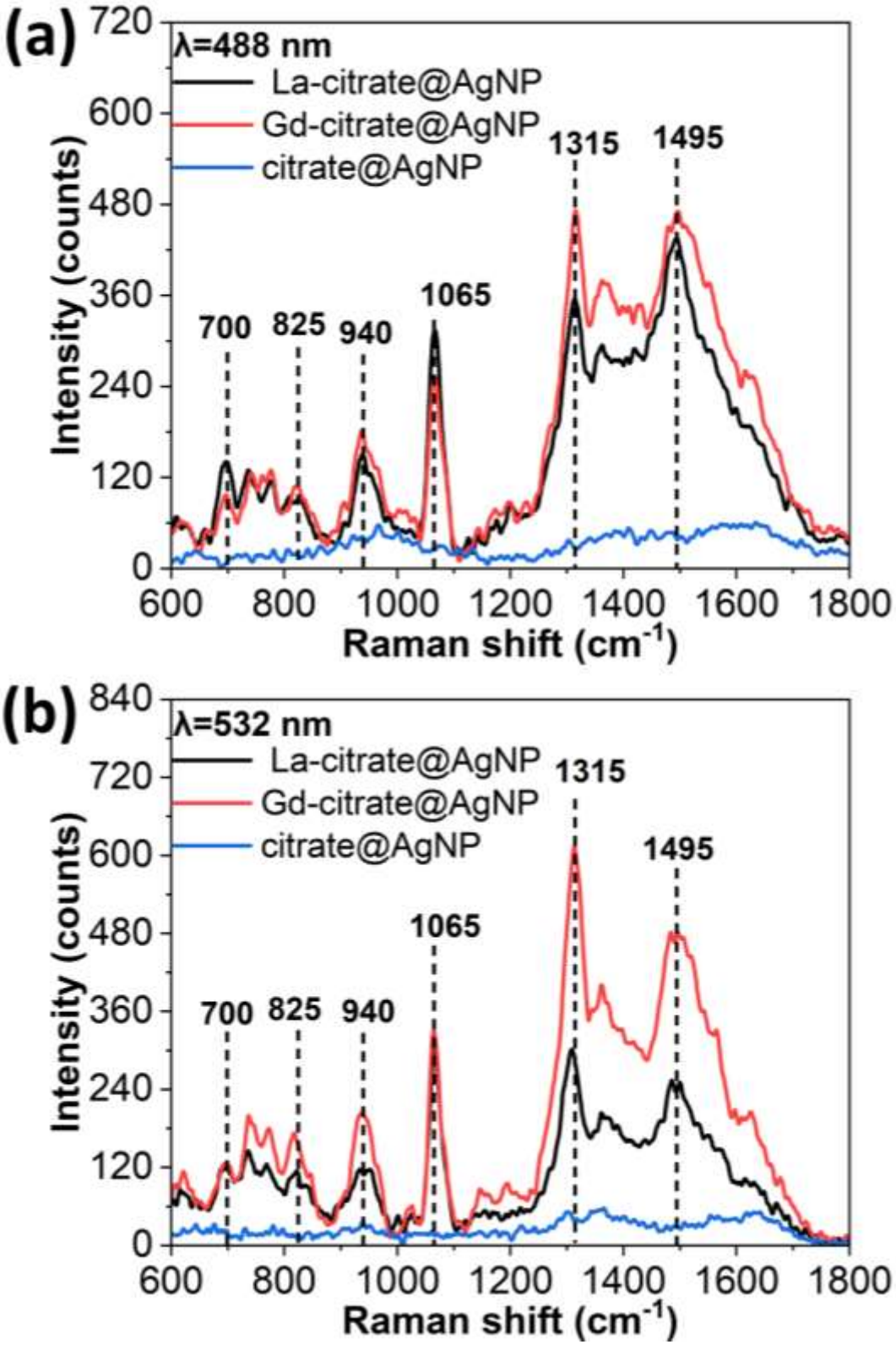

Figure 3.13. SERS spectra of La-citrate (black line), Gd-citrate (red line) and citrate (blue line) excited at (a) 488 nm and (b) 532 nm. Peak assignments are shown in Table 1.

The SERS intensity of Ln-citrates was several times higher than that of citrate due to the hotspot regions formed after adding Ln^{3+} ions. The characteristic peak positions in the SERS spectrum obtained by Ln-citrate were close to each other corresponding to the same vibrational model that was analyzed by DFT simulation (Tables 3.1 and 3.2). Thus, approximate position classifications were made based on vibration bands of SERS characteristic peaks, which were marked with a black dotted line. In comparison with the SERS spectrum without Ln^{3+} ions (blue line), the characteristic peaks in the SERS spectra with La^{3+} ions (black line) and Gd^{3+} ions (red line), inconspicuous peaks appeared in the region of 700 − 825 cm^{-1}, and significant peaks were at 940, 1065, 1315 and 1495 cm^{-1}, respectively. We mainly analyzed the relative intensities of peaks in the interval from 1000 cm^{-1} to 1800 cm^{-1} in Figure 3.13. We observed that the relationship between the relative intensities of the peaks near 1065 and 1315 cm^{-1} was determined by the type of Ln^{3+} ions, independent of the laser wavelength. For La-citrate, the relative intensities of these two SERS peaks were almost identical. On the other hand, for Gd-citrate, the intensity of the SERS peak near 1065 cm^{-1} was almost half of the SERS peak intensity at 1315 cm^{-1}. However, when the laser wavelength was changed, the peaks' relative intensities of peaks at 1315 and 1495 cm^{-1} in SERS spectra of La-citrate and Gd-citrate were significantly changed. Only when the laser wavelength was 532 nm, the intensities of peaks near 1315 cm^{-1} were higher than the intensities of peaks near 1495 cm^{-1}. Therefore, we focused on the analysis of these three SERS peaks that correspond to the C-O bond and two COO^- groups of citrates coordinated with Ln^{3+}.

Figures 3.14 (a) and (b) show the changes in the SERS spectra in the region of 1000 − 1400 cm^{-1} upon the addition of La^{3+} and Gd^{3+} ions to citrate@AgNPs under laser excitation at different wavelengths.

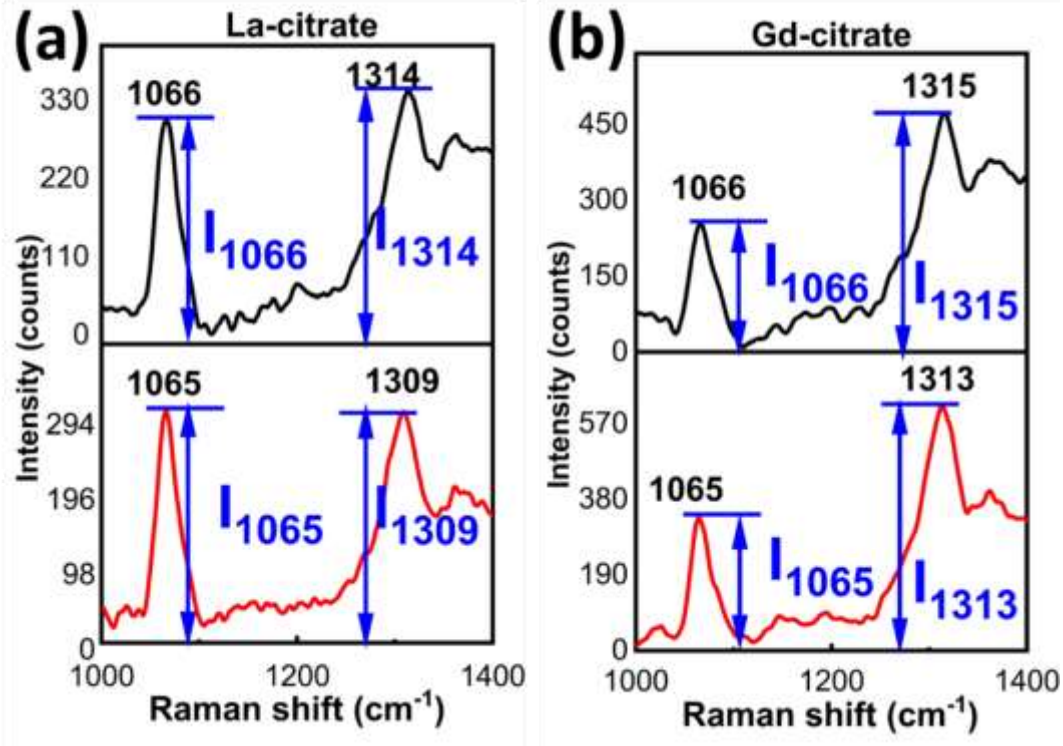

Figure 3.14. SERS spectra in the region of 1000 − 1400 cm^{-1} excited at 488 nm (black line) and 532 nm (red line) of (a) La-citrate and (b) Gd-citrate. The blue line shows the method to obtain the intensities of characteristic peaks.

With the addition of La^{3+} ions, the intensities of the characteristic peaks around 1065 cm^{-1} remain basically the same as the intensities of the characteristic peaks around 1315 cm^{-1}. When Gd^{3+} ions were added, the intensities of the characteristic peaks at approximately 1065 cm^{-1} were significantly weaker than those at approximately 1315 cm^{-1}, and this relative SERS intensity relationship was not affected by the laser wavelength.

Figure 3.15 shows the relative intensity ratios of these two characteristic peaks around 1065 and 1315 cm^{-1} under laser excitation at different wavelengths.

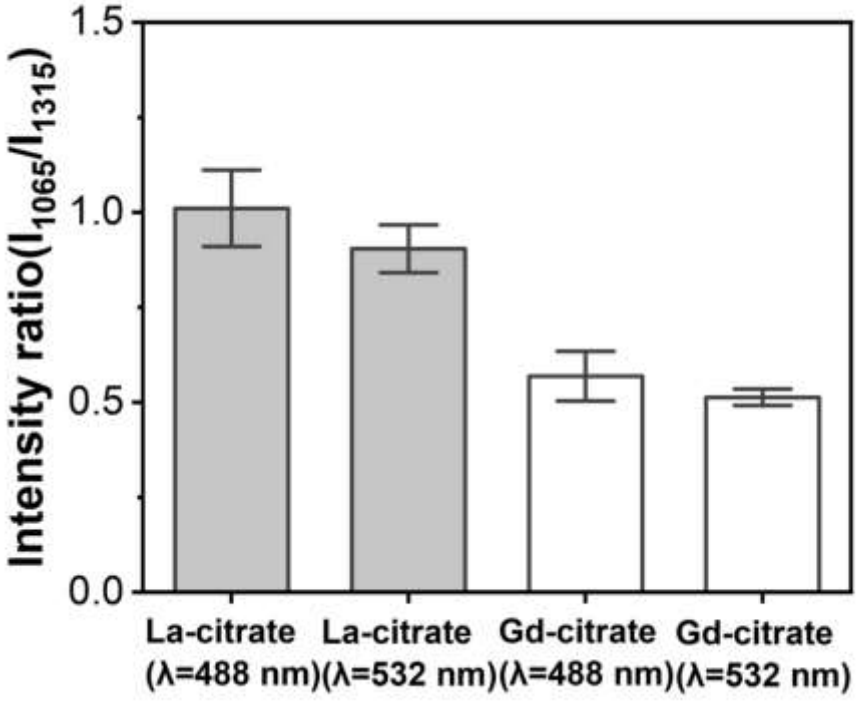

Figure 3.15. Ratios of intensities of characteristic peaks around 1065 cm^{-1} and 1315 cm^{-1} under different wavelength lasers' excitations for ion classification. the numbers of data analyzed were 9, 8, 9 and 8 for La-citrate (488 nm), La-citrate (532 nm), Gd-citrate (488 nm) and Gd-citrate (532 nm), respectively. Error bars are ± SD.

In this figure, the I_{1065}/I_{1315} ratios of La-citrate and Gd-citrate are approximately 1 and 0.55, respectively, enabling us to classify La^{3+} and Gd^{3+} ions by SERS measurements.

In comparison to Figures 3.14 and 3.15, Figures 3.16 and 3.17 show a negative description of the changes in the SERS spectra in the region of 1200 − 1800 cm^{-1} for the addition of La^{3+} and Gd^{3+} ions to citrate@AgNPs under laser excitation at different wavelengths.

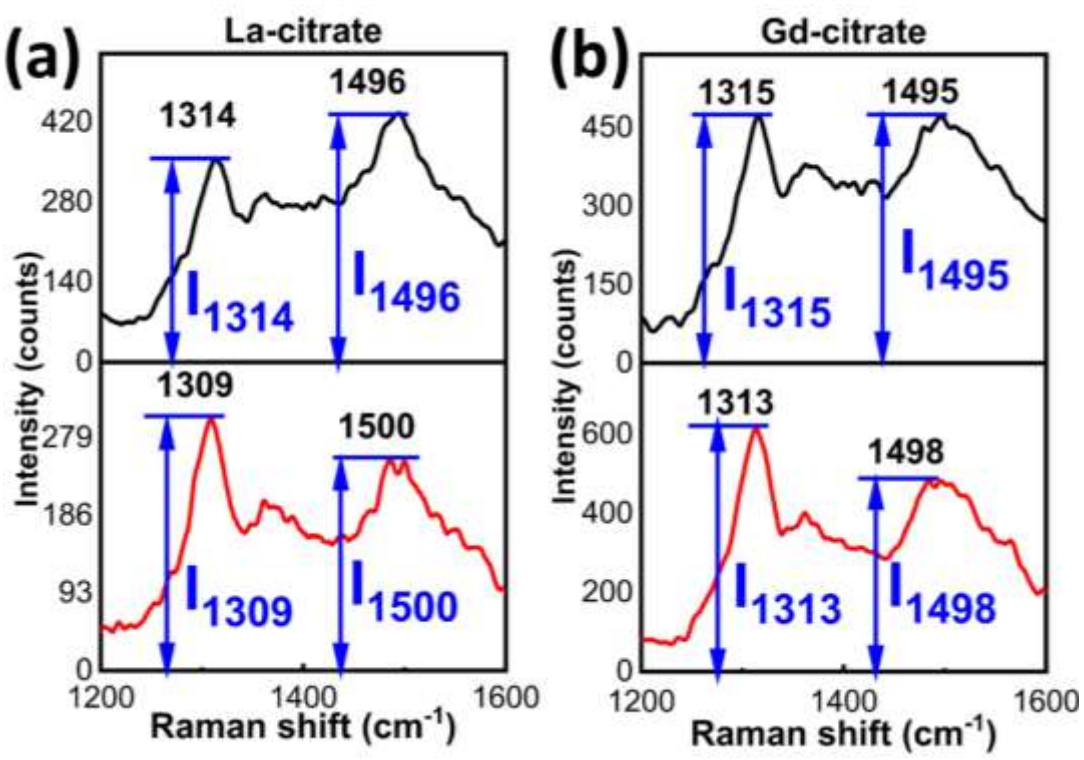

Figure 3.16. SERS spectra in the region of 1200 − 1600 cm^{-1} excited at 488 nm (black line) and 532 nm (red line) of (a)La-citrate and (b)Gd-citrate.

There are two characteristic peaks in this region, at around 1315 cm^{-1} and 1495 cm^{-1}, when the Ln-citrate@AgNPs were excited at 488 nm and 532 nm. Moreover, the relative intensity ratios I_{1495}/I_{1315} of Ln-citrate shown in Figure 3.17 did not exhibit a clear difference between the La^{3+} and Gd^{3+} ions.

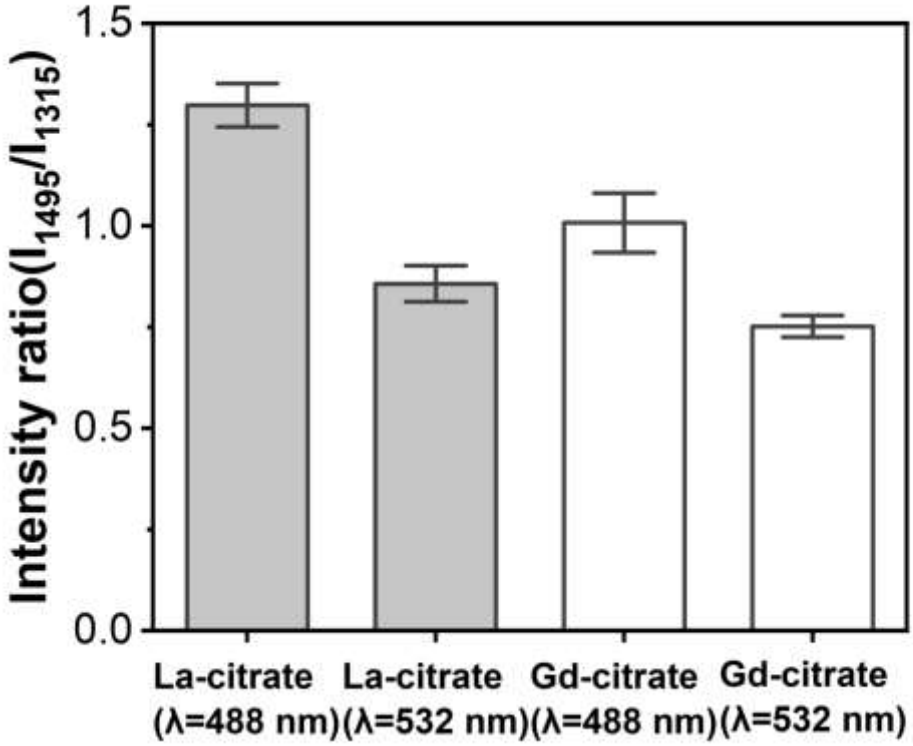

Figure 3.17. Ratios of intensities of characteristic peaks around 1315 cm^{-1} and 1495 cm^{-1} under different wavelength lasers' excitations for ion classification. the numbers of data analyzed were 9, 8, 9 and 8 for La-citrate (488 nm), La-citrate (532 nm), Gd-citrate (488 nm) and Gd-citrate (532 nm), respectively. Error bars are ± SD.

3.7.3 Analysis of spectral variation mechanisms

Here, we discussed how different Ln^{3+} ions, La^{3+} and Gd^{3+}, can be classified using SERS measurements, even though these ions have similar chemical properties and outer electronic configurations. We referred to previous studies[12][13] and found that the differences between the intensity ratios of these SERS characteristic peaks are related to the spin state difference of the ions. Theoretically, the difference in unpaired electrons in the 4f orbital of La^{3+} (electronic configuration: $[Xe]4f^0$, no spin) and Gd^{3+} (electronic configuration: $[Xe]4f^7$, highest spin) ions results in a significant spin disparity. When the Ln^{3+} ion and citrate coordinate to form a complex, the 4f orbital of the Ln^{3+} ion is the inner orbital, and such spin difference between La^{3+} and Gd^{3+} can still be maintained. For each Ln-citrate complex system at pH = 7, the spin multiplicity depends on the

number of unpaired electrons of Ln^{3+}. Thus, the La-citrate complex is the low-spin state complex and the Gd-citrate complex is the high-spin state complex. Additionally, reference 54 reported on the ESR measurements of La-citrate and Gd-citrate complexes, with only the signal of the Gd-citrate complex being observed. The experimental results qualitatively indicate that Gd-citrate is high-spin compared to La-citrate. This is consistent with our theoretical predictions. Therefore, we focused on the effect of spin differences on the relative intensities of characteristic peaks for the classification of La^{3+} and Gd^{3+} ions.

On another hand, Raman scattering is produced by the induced dipole moment, which is the change of the polarizability around the equilibrium nuclear coordinates[11]. By combining our simulation results and theoretical calculation methods[55], we found that the higher electron density in the coordination region results in increased resistance to polarization, which results in a lower Raman intensity[11][55]. In our present Ln-complex@AgNP simulations, the vibrational modes of each Ln-complex were similar in the range of 600−1800 cm^{-1}. However, La^{3+} and Gd^{3+} ions have a huge difference in the number of unpaired electrons in their 4f orbitals, which affects the induced dipole moment. Thus, the SERS spectra of Ln-citrate complexes have intensity differences for the peaks at similar positions. This suggests that the spin population can characterize the distribution of unpaired electrons which indirectly shows the condition of electron density difference[56]. Citrate molecule has one hydroxyl (-OH) group and three carboxyl (COO^-) groups. For our Ln-citrate complexes ($LnCit^-$ at pH=7), the (C-O···Ln) and (COO-Ln) bands were generated by the coordination of Ln^{3+} ions with the C-O bond and two COO^- groups of citrates. These two bands exhibit differences, especially the electron density difference caused by the spin difference between La^{3+} and Gd^{3+} ions. This was confirmed by corresponding the relative intensities of SERS peaks

around 1065 cm^{-1} and 1315 cm^{-1}. Thus, combining the results of Figure 3.16Figure(c), the relative intensity differences between these two bands around 1065 cm^{-1} and 1315 cm^{-1} in the SERS spectrum are mainly attributed to the electron density difference caused by the spin state difference of La^{3+} and Gd^{3+} ions. Moreover, this relationship of the relative intensity differences between these two bands around 1065 cm^{-1} and 1315 cm^{-1} in the SERS spectrum can be used for the classification of La^{3+} and Gd^{3+} ions.

We also used DFT calculation results to analyze the sources of the differences between these two vibration bands. To obtain simulated Raman spectra, the Raman activity of each vibrational mode should be converted to the Raman intensity of each vibrational mode by the equation (2.6) [57].

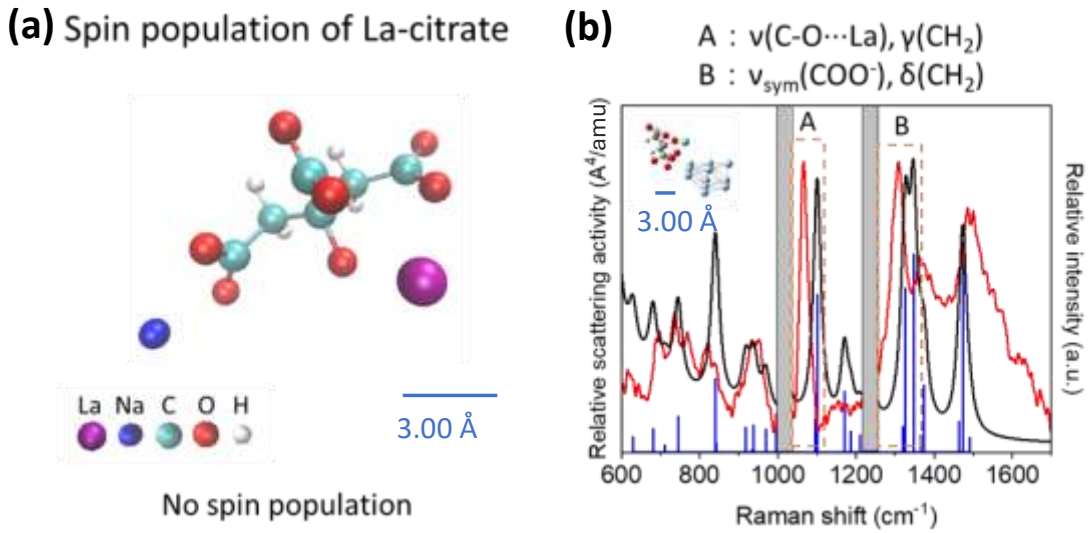

Figure 3.18. (a) Structure and spin population of La-citrate. (b) Experimental SERS spectrum excited at 532 nm (red line), simulated SERS spectrum (black line) and an estimated structure of La-citrate adsorbed on silver surface.

Figure 3.18(a) shows the structure and spin population of the La-citrate complex. This complex does not contain unpaired electrons, and thus its spin population is zero. Figure 3.18(b) shows a comparison of the scaled simulated SERS spectrum and the experimental spectrum under 532 nm excitation of La-citrate. The main characteristic peaks of the (C-O···La) and (COO^-) bands were well matched, the intensity of the ν(C-

O···La) was close to that of the $\nu_{sym}(COO^-)$, while the intensity of the $\nu_{sym}(COO^-)$ was stronger than that of $\nu_{asym}(COO^-)$ both in simulated and experimental spectra; thus, the spectral shapes were also basically the same. There are some discrepancies between the simulated and experimental spectra, which may be due to the mixture of binding modes of actual citrate, resulting in the inability of a single simplified model to simulate the full details[47] and the effects of mixed basis sets. These discrepancies were acceptable after scaling using suitable scaling factors[39][40].

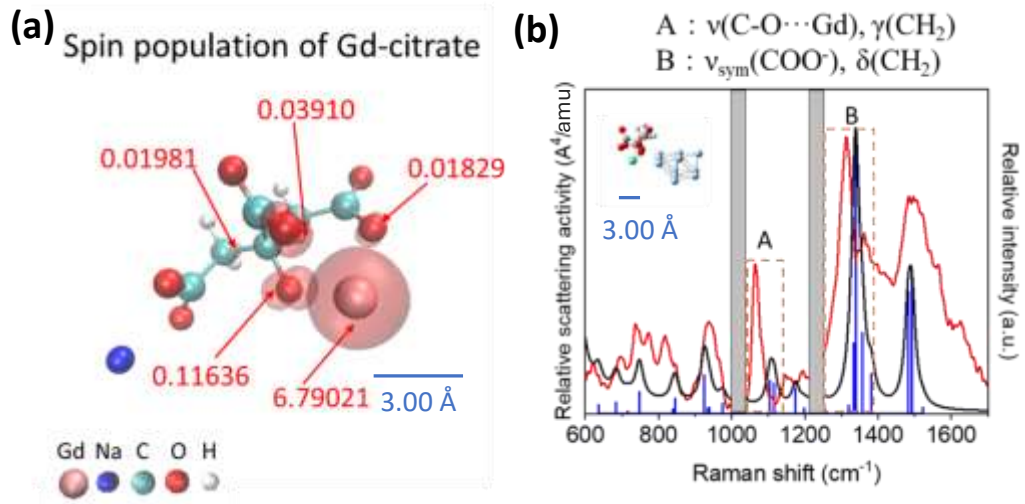

Figure 3.19. (a) Structure and spin population of Gd-citrate. (b) Experimental SERS spectrum excited at 532 nm (red line), simulated SERS spectrum (black line) and an estimated structure of Gd-citrate adsorbed on silver surface.

Figure 3.19(a) shows the structure and spin population of Gd-citrate. The spin population of the C-O bond and COO^- groups coordinated with the Gd^{3+} ion was not 0, which was because the Gd^{3+} ion has seven unpaired electrons in the 4f orbital. Thus, combining the results of La-citrate, the (C-O···Ln) and the (COO^-) bands were affected by the Ln^{3+} ion's spin state and can be considered spin-state-related bands in the SERS spectrum. Figure 3.19(b) shows a comparison of the scaled simulated SERS spectrum and the experimental spectrum under 532 nm laser excitation of Gd-citrate. Although there were some differences between the simulated and experimental spectra, the

intensity of the ν(C-O···Gd) was lower than that of $\nu_{sym}(COO^-)$, while the intensity of the $\nu_{sym}(COO^-)$ was stronger than that of the $\nu_{asym}(COO^-)$ both in simulated and experimental spectra. Thus, this relative intensity feature was similar to the experimental SERS spectrum excited at 532 nm and was also exhibited by the DFT calculation results.

The effect of the binding condition of citrate and silver clusters on the simulated SERS spectra has been investigated by Ahuja, T et al[2]. Based on our experimental data, the shapes of the SERS spectra obtained after the addition of Ln^{3+} ions were different. This may be related to the adsorption state of different Ln-citrate complexes with silver clusters. We also verified this idea with DFT calculations.

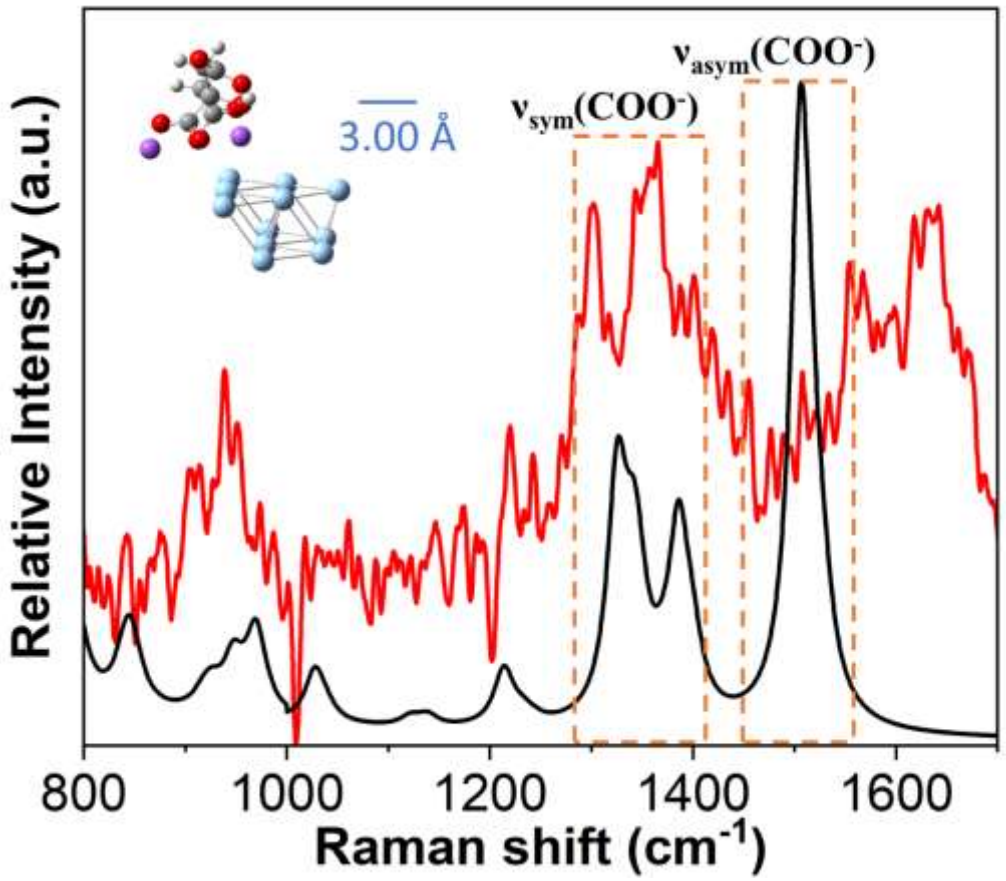

Figure 3.20. Experimental SERS spectrum excited at 532 nm (red line), simulated SERS spectrum (black line) and an estimated structure of citrate adsorbed on silver surface. The simulated SERS spectrum in the region of 1000 − 1700 cm^{-1} was scaled by scaling factor 0.956.

We compared the adsorption relationship and simulated SERS spectra of citrate and Ln-citrate with silver clusters shown in Figure 3.20, Figure 3.18 (b) and Figure 3.19 (b), respectively. We found that due to the addition of Ln^{3+} ions, the adsorption states of Ln-citrate complexes with silver clusters change compared to that of citrate, leading to a significant difference in the simulated SERS spectra. Among them, the adsorption states of Ln-citrate complexes with silver clusters are similar.

In Figure 3.18(a) and Figure 3.19(a), we compared the electronic structures of citrate regions around different Ln^{3+} ions by spin population. The symmetry relationship of the electronic structure was roughly shown in the spin population. The Gd-citrate has 7 more unpaired electrons than La-citrate resulting in the spin population of it was not 0. Especially at the C-O bond where citrate coordinates with Gd^{3+} ions, indicating that the electron density in this part was higher. Hence, the polarization of C-O···Gd is comparatively more difficult than that of C-O···La when subjected to laser light of identical wavelengths, thereby leading to a reduced Raman intensity. In addition, we also considered the mass effect of ions. For the Ln-citrate complexes, the frequencies of COO^- coordinated to Ln^{3+} ions, e.g. near 940, 1315 and 1495 cm^{-1}, are significantly lower than the frequencies of COO^- for citrate in Table 2, e.g. at 956, 1390 and 1580 cm^{-1}. This is because La and Gd atoms are much heavier than H atoms. In contrast, comparing the experimental SERS spectra of Ln-citrate complexes, the positions of characteristic SERS peaks were similar in the range of 600−1800 cm^{-1}. This was due to the vibrational contribution of Ln^{3+} being too weak as studied by DFT simulations. In addition, based on the mass effect, characteristic bands of Ln^{3+} should be in the lower frequency region. However, we are unable to assign characteristic bands of Ln^{3+} due to the lack of isotopic Ln elements and citrate molecules.

Such experimental and computational results indicate that a large spin difference

between the Ln^{3+} ions, La^{3+} and Gd^{3+}, can be observed in the relative intensities of the characteristic peaks of their SERS spectra. When Ln^{3+} ions coordinate with the C-O bond and COO^- groups of citrate molecules, the corresponding SERS characteristic peaks are around 1065 cm^{-1} and 1315 cm^{-1}, and can be considered as spin-related bands. The presence of these spin-related bands in the SERS spectrum could be used for marking the spin state of the complex based on the relative intensity relationship of spin-state-related peaks. This method is similar to that reported by Kitahama et al[12]. The relative intensity ratio of the two spin-state-related bands is not affected by the laser wavelength, thus it can be used to classify La^{3+} and Gd^{3+} ions based on their SERS spectra.

3.8 Summary

In this study, we found that the SERS spectra of Ln-citrate complexes (Ln: La, Gd) could be used for the qualitative classification of La^{3+} and Gd^{3+} ions, possibly because of the spin-related bands in the SERS spectrum. By evaluating the spectral relationship of sample solutions with and without citrate@AgNPs, we confirmed that the SERS spectrum of Ln-citrate complexes could be obtained by adding a small amount of Ln^{3+} solution to citrate@AgNPs. In the SERS spectra, the positions of the SERS characteristic peaks of La-citrate and Gd-citrate were similar, and these peak positions did not change significantly with the change in excitation wavelength. However, the intensities of the SERS characteristic peaks were different, especially in the interval from 1000 to 1800 cm^{-1}. Three characteristic peaks around 1065, 1315, and 1495 cm^{-1} were used to explore the differences in the SERS spectra of the different Ln-citrate complexes. Combined with DFT calculations, the characteristic SERS peaks near 1065 cm^{-1} and 1315 cm^{-1} were assigned to spin-state-related bands (C-O···Ln) and (COO^-), respectively. Their relative intensity changes were related to the electron density in the

region coordinated by Ln^{3+} ions. Moreover, the relative intensity relationship of the SERS peaks near 1065 cm^{-1} and 1315 cm^{-1} can be used to classify La^{3+} and Gd^{3+} ions. The ratios of I_{1065}/I_{1315} for La-citrate and Gd-citrate were in the range of approximately 1 and 0.55, respectively. The results of the present study show that using the physical properties of Ln elements, such as the spin state, Ln-citrate complexes can be constructed as target molecules to study the differences in their SERS spectra, thus enabling the classification of different Ln^{3+} ions via SERS, as well as examining the effects of Ln^{3+} ions on SERS. In future studies, we will investigate the effects of the physical properties of other Ln^{3+} ions, such as Pr^{3+} and Nd^{3+} ions, on the SERS spectra, and DFT SERS simulations of Ln-molecule complexes.

3.9 References

(1)Rainer Pöttgen; Jüstel, T.; Strassert, C. A.*Rare Earth Chemistry*; Walter de Gruyter GmbH & Co KG, 2020,83-98.

(2) Eliseeva, S. V.; Bünzli, J.-C. G. Lanthanide Luminescence for Functional Materials and Bio-Sciences. *Chem. Soc. Rev.* 2010, 39 (1), 189-227.

(3) Wang, G.; Peng, Q.; Li, Y. Lanthanide-Doped Nanocrystals: Synthesis, Optical-Magnetic Properties, and Applications. *Accounts of Chemical Research* 2011, 44 (5), 322–332.

(4) Huang, C.-H. *Rare Earth Coordination Chemistry*; John Wiley & Sons, 2011, 335-472.

(5) Kotyk, C. M.; Weber, J. E.; Hyre, A. S.; McNeely, J.; Monteiro, J. H. S. K.; Domin, M.; Balaich, G. J.; Rheingold, A. L.; de Bettencourt-Dias, A.; Doerrer, L. H. Luminescence of Lanthanide Complexes with Perfluorinated Alkoxide Ligands. *Inorganic Chemistry* 2020, 59 (14), 9807–9823.

(6) Lee, H. Y.; Jee, H. W.; Seo, S. M.; Kwak, B. K.; Khang, G.; Cho, S. H.

Diethylenetriaminepentaacetic Acid−Gadolinium (DTPA-Gd)-Conjugated Polysuccinimide Derivatives as Magnetic Resonance Imaging Contrast Agents. *Bioconjugate Chemistry* 2006, *17* (3), 700–706.

(7) Martínez-Pérez, M. J.; Cardona-Serra, S.; Schlegel, C.; Moro, F.; Alonso, P. J.; Prima-García, H.; Clemente-Juan, J. M.; Evangelisti, M.; Gaita-Ariño, A.; Sesé, J. et al. Gd-Based Single-Ion Magnets with Tunable Magnetic Anisotropy: Molecular Design of Spin Qubits. *Physical Review Letters* 2012, 108 (24), 247213.

(8) Skripka A, Karabanovas V, Jarockyte G, et al. Decoupling theranostics with rare earth doped nanoparticles. *Advanced Functional Materials* 2019, 29(12): 1807105.

(9) Serrano, D.; Kuppusamy, S. K.; Heinrich, B.; Fuhr, O.; Hunger, D.; Ruben, M.; Goldner, P. Ultra-Narrow Optical Linewidths in Rare-Earth Molecular Crystals. *Nature* 2022, 603 (7900), 241–246.

(10) Liu, Y.; Chang, Z.; Yuan, H.; Fales, A. M.; Vo-Dinh, T. Quintuple-Modality (SERS-MRI-CT-TPL-PTT) Plasmonic Nanoprobe for Theranostics. *Nanoscale* 2013, 5 (24), 12126.

(11) Colthup, N. B.; Daly, L. H.; Wiberley, S. E. *Introduction to Infrared and Raman Spectroscopy*; Academic Press: San Diego, Calif., 1998,60-65.

(12) Kitahama, Y.; Egashira, M.; Suzuki, T.; Tanabe, I.; Ozaki, Y. Sensitive Marker Bands for the Detection of Spin States of Heme in Surface-Enhanced Resonance Raman Scattering Spectra of Metmyoglobin. *The Analyst* 2014, 139 (24), 6421–6425.

(13) Ozaki, Y.; Kitagawa, T.; Kyogoku, Y. Raman Study of the Acid-Base Transition of Ferric Myoglobin; Direct Evidence for the Existence of Two Molecular Species at Alkaline PH. *FEBS Letters* 1976, 62 (3), 369–372.

(14) Nie S; Emory SR. Probing Single Molecules and Single Nanoparticles by Surface-Enhanced Raman Scattering. *Science* 1997, 275 (5303), 1102–1106.

(15) Fleischmann, M.; Hendra, P. J.; McQuillan, A. J. Raman Spectra of Pyridine Adsorbed at a Silver Electrode. *Chemical Physics Letters* 1974, 26 (2), 163–166.

(16) Albrecht, M. G.; Creighton, J. A. Anomalously Intense Raman Spectra of Pyridine at a Silver Electrode. *J. Am. Chem. Soc*. 1977, 99, 5215−5217.

(17) Jeanmaire, D. L.; Van Duyne, R. P. Surface Raman Spectroelectrochemistry: Part I. Heterocyclic, Aromatic, and Aliphatic Amines Adsorbed on the Anodized Silver Electrode. *J. Electroanal.Chem*. 1977, 84, 1−20.

(18) Link, S.; El-Sayed, M. A. Spectral Properties and Relaxation Dynamics of Surface Plasmon Electronic Oscillations in Gold and Silver Nanodots and Nanorods. *The Journal of Physical Chemistry B* 1999, 103 (40), 8410–8426.

(19) Yamamoto, Y. S.; Itoh, T. Why and How Do the Shapes of Surface-Enhanced Raman Scattering Spectra Change? Recent Progress from Mechanistic Studies. *Journal of Raman Spectroscopy* 2016, *47* (1), 78–88.

(20) Itoh, T.; Procházka, M.; Dong, Z.-C.; Ji, W.; Yamamoto, Y. S.; Zhang, Y.; Ozaki, Y. Toward a New Era of SERS and TERS at the Nanometer Scale: From Fundamentals to Innovative Applications. *Chemical Reviews* 2023, *123* (4), 1552–1634.

(21) Yang, S.; Yao, J.; Quan, Y.; Hu, M.; Su, R.; Gao, M.; Han, D.; Yang, J. Monitoring the Charge-Transfer Process in a Nd-Doped Semiconductor Based on Photoluminescence and SERS Technology. *Light: Science & Applications* 2020, 9 (1), 1143-1149.

(22) Runowski, M.; Goderski, S.; Paczesny, J.; Księżopolska-Gocalska, M.; Ekner-Grzyb, A.; Grzyb, T.; Rybka, J. D.; Giersig, M.; Lis, S. Preparation of Biocompatible, Luminescent-Plasmonic Core/Shell Nanomaterials Based on Lanthanide and Gold Nanoparticles Exhibiting SERS Effects. *The Journal of Physical Chemistry C* 2016, 120 (41), 23788–23798.

(23) Derom, S.; Berthelot, A.; Pillonnet, A.; Benamara, O.; Jurdyc, A. M.; Girard, C.; Colas des Francs, G. Metal Enhanced Fluorescence in Rare Earth Doped Plasmonic Core–Shell Nanoparticles. *Nanotechnology* 2013, 24 (49), 495704.

(24) Wang, J.; Huang, H.; Zhang, D.; Chen, M.; Zhang, Y.; Yu, X.; Zhou, L.; Wang, Q. Synthesis of Gold/Rare-Earth-Vanadate Core/Shell Nanorods for Integrating Plasmon Resonance and Fluorescence. *Nano Research* 2015, 8 (8), 2548–2561.

(25) López-Neira, J. P.; Galicia-Hernández, J. M.; Reyes-Coronado, A.; Pérez, E.; Castillo-Rivera, F. Surface Enhanced Raman Scattering of Amino Acids Assisted by Gold Nanoparticles and Gd^{3+} Ions. *The Journal of Physical Chemistry A* 2015, *119 (18), 4127–4135.*

(26) Carnall, W. T. The Absorption and Fluorescence Spectra of Rare Earth Ions in Solution. *Handbook on the Physics and Chemistry of Rare Earths*, Vol. 3, 1979, 171-208.

(27) Munro, C. H.; Smith, W. E.; Garner, M.; Clarkson, J.; White, P. C. Characterization of the Surface of a Citrate-Reduced Colloid Optimized for Use as a Substrate for Surface-Enhanced Resonance Raman Scattering. *Langmuir* 1995, *11* (10), 3712–3720.

(28) Lee, P. C.; Meisel, D. Adsorption and Surface-Enhanced Raman of Dyes on Silver and Gold Sols. *The Journal of Physical Chemistry* 1982, *86* (17), 3391–3395.

(29) Ivanova, V. Yu.; Shurygin, I. D.; Chevela, V. V.; Ajsuvakova, O. P.; Semenov, V. E.; Bezryadin, S. G. New Aspects of Complex Formation in the Gadolinium(III)–Citric Acid System in Aqueous Solution. *Comments on Inorganic Chemistry* 2021, *42* (2), 109–144.

(30) Grimme, S.; Antony, J.; Ehrlich, S.; Krieg, H. A Consistent and Accurate Ab Initio Parametrization of Density Functional Dispersion Correction (DFT-D) for the 94 Elements H-Pu. *The Journal of Chemical Physics* 2010, *132* (15), 154104.

(31) Paier, J.; Marsman, M.; Kresse, G. Why Does the B3LYP Hybrid Functional Fail for Metals? *The Journal of Chemical Physics* 2007, *127* (2), 024103.

(32) Adamo, C.; Barone, V. Toward Reliable Density Functional Methods without Adjustable Parameters: The PBE0 Model. *The Journal of Chemical Physics* 1999, *110* (13), 6158–6170.

(33) Grimme, S.; Ehrlich, S. and Goerigk, L. Effect of the damping function in dispersion corrected density functional theory. *J. Comput. Chem.* 2011, 32: 1456-1465.

(34) Chen, X.; Chen, T.-T.; Li, W.-L.; Lu, J.-B.; Zhao, L.-J.; Jian, T.; Hu, H.-S.; Wang, L.-S.; Li, J. Lanthanides with Unusually Low Oxidation States in the PrB3- and PrB4- Boride Clusters. *Inorganic Chemistry* 2019, *58* (1), 411–418.

(35) Brémond, É.; Savarese, M.; Su, N. Q.; Pérez-Jiménez, Á. J.; Xu, X.; Sancho-García, J. C.; Adamo, C. Benchmarking Density Functionals on Structural Parameters of Small-/Medium-Sized Organic Molecules. *Journal of Chemical Theory and Computation* 2016, *12* (2), 459–465.

(36) Dunning, T. H. Gaussian Basis Sets for Use in Correlated Molecular Calculations. I. The Atoms Boron through Neon and Hydrogen. *The Journal of Chemical Physics* 1989, *90* (2), 1007–1023.

(37) Andrae, D.; Häußermann U.; Dolg, M.; Stoll, H.; Preuß, H. Energy-Adjustedab Initio Pseudopotentials for the Second and Third Row Transition Elements. *Theoretica Chimica Acta* 1990, *77* (2), 123–141.

(38) Dolg, M.; Stoll, H.; Savin, A.; Preuss, H. Energy-Adjusted Pseudopotentials for the Rare Earth Elements. *Theoretica Chimica Acta* 1989, *75* (3), 173–194.

(39) Dolg, M.; Stoll, H.; Preuss, H. A Combination of Quasirelativistic Pseudopotential and Ligand Field Calculations for Lanthanoid Compounds. *Theoretica Chimica Acta* 1993, *85* (6), 441–450.

(40) Rappoport, D. Property-Optimized Gaussian Basis Sets for Lanthanides. *The Journal of Chemical Physics* 2021, *155* (12), 124102.

(41) Kashinski, D. O.; Chase, G. M.; Nelson, R. G.; Di Nallo, O. E.; Scales, A. N.; VanderLey, D. L.; Byrd, E. F. C. Harmonic Vibrational Frequencies: Approximate Global Scaling Factors for TPSS, M06, and M11 Functional Families Using Several Common Basis Sets. *The Journal of Physical Chemistry. A* 2017, *121* (11), 2265–2273.

(42) Straßner, A.; Wiehn, C.; Klein, M. P.; Fries, D. V.; Dillinger, S.; Mohrbach, J.; Prosenc, M. H.; Armentrout, P. B.; Gereon Niedner-Schatteburg. Cryo Spectroscopy of N2 on Cationic Iron Clusters. The Journal of Chemical Physics 2021, 155 (24). (43) Weigend, F.; Ahlrichs, R. Balanced Basis Sets of Split Valence, Triple Zeta Valence and Quadruple Zeta Valence Quality for H to Rn: Design and Assessment of Accuracy. *Physical Chemistry Chemical Physics* 2005, *7* (18), 3297.

(44) Lu, T.; Chen, F. Multiwfn: A Multifunctional Wavefunction Analyzer. *Journal of Computational Chemistry* 2011, *33* (5), 580–592.

(45) Humphrey, W.; Dalke, A.; Schulten, K. VMD: Visual Molecular Dynamics. *Journal of Molecular Graphics* 1996, *14* (1), 33–38.

(46) Park, J.-W.; Shumaker-Parry, J. S. Structural Study of Citrate Layers on Gold Nanoparticles: Role of Intermolecular Interactions in Stabilizing Nanoparticles. *Journal of the American Chemical Society* 2014, *136* (5), 1907–1921.

(47) Ahuja, T.; Chaudhari, K.; Paramasivam, G.; Ragupathy, G.; Mohanty, J. S.; Pradeep, T. Toward Vibrational Tomography of Citrate on Dynamically Changing Individual Silver Nanoparticles. *The Journal of Physical Chemistry C* 2021, *125* (6), 3553–3566.

(48) Vanhoyland, G.; Pagnaer, J.; D'Haen, J.; Mullens, S.; Mullens, J. Characterization and Structural Study of Lanthanum Citrate Trihydrate [La(C6H5O7) (H2O)2]·H2O.

Journal of Solid State Chemistry 2005, *178* (1), 166–171.

(49) Yon, M.; Pibourret, C.; Marty, J.-D.; Ciuculescu-Pradines, D. Easy Colorimetric Detection of Gadolinium Ions Based on Gold Nanoparticles: Key Role of Phosphine-Sulfonate Ligands. *Nanoscale Advances* 2020, *2* (10), 4671–4681.

(50) Yamamoto, Y. S.; Ozaki, Y.; Itoh, T. Recent Progress and Frontiers in the Electromagnetic Mechanism of Surface-Enhanced Raman Scattering. *Journal of Photochemistry and Photobiology C: Photochemistry Reviews* 2014, *21*, 81–104.

(51) Xu, H.; Wang, X.-H.; Persson, M. P.; Xu, H. Q.; Käll, M.; Johansson, P. Unified Treatment of Fluorescence and Raman Scattering Processes near Metal Surfaces. *Physical Review Letters* 2004, *93* (24), 243002.

(52) Kerker, M.; Siiman, O.; Bumm, L. A.; Wang, D.-S.Y. Surface Enhanced Raman Scattering (SERS) of Citrate Ion Adsorbed on Colloidal Silver. *Applied Optics* 1980, *19* (19), 3253.

(53) Nakabayashi, T.; Kosugi, K.; Nishi, N. Liquid Structure of Acetic Acid Studied by Raman Spectroscopy and Ab Initio Molecular Orbital Calculations. *The Journal of Physical Chemistry A* 1999, *103* (43), 8595–8603.

(54) Baggio, R.; Calvo, R.; María Teresa Garland; O. Peña; Perec, M.; Alberto Claudio Rizzi. Gadolinium and neodymium citrates: Evidence for weak ferromagnetic exchange between gadolinium (III) cations. *Inorganic chemistry* 2005, 44 (24) , 8979-8987.

(55) Porezag D; Pederson M R. Infrared intensities and Raman-scattering activities within density-functional theory. *Physical Review B*, 1996, 54(11): 7830-7836.

(56) Boguslawski, K.; Jacob, C. R.; Reiher, M. Can DFT accurately predict spin densities? Analysis of discrepancies in iron nitrosyl complexes. *Journal of Chemical Theory and Computation*, 2011, 7(9): 2740-2752.

(57) Liu, Z.; Lu, T.; Chen, Q. Vibrational Spectra and Molecular Vibrational Behaviors

of All-Carboatomic Rings, Cyclo[18]Carbon and Its Analogues. *Chemistry – An Asian Journal* 2020, *16* (1), 56–63.

Chapter 4: SERS and DFT Study of 7 Lanthanide Ions

4.1 Chapter overview

In this study, we combined the surface-enhanced Raman scattering (SERS) with density functional theory (DFT) calculations to investigate the SERS spectra of lanthanide (Ln)-citrate complexes (Ln = La, Ce, Pr, Nd, Sm, Eu, and Gd) under 488, 532, and 660 nm laser excitations, with the aim of elucidating how variations in 4f electronic structure influence their spectral response. Detailed vibrational analysis and peak assignments were performed based on SERS spectra simulated using an optimized DFT setting, in which small-core effective core potentials (ECPs) in the def2-tzvpd basis set were replaced by large-core ECPs. Characteristic SERS peaks appeared at 1065, 1315, and 1485 cm^{-1} were assigned to the $\gamma(CH_2) + \nu(C\text{-}O\cdots Ln)$, $\nu_{sym}(COO^-) + \gamma(CH_2)$, and $\nu_{asym}(COO^-) + \gamma(CH_2)$ vibrational bands, respectively. SERS intensity ratios were obtained by normalizing the peak intensity I near 1065 or 1485 cm^{-1} to that near 1315 cm^{-1}. I_{1065}/I_{1315} depended solely on the type of Ln^{3+} ion and was independent of the excitation wavelength. In contrast, I_{1485}/I_{1315} increased with decreasing excitation wavelength, indicating additional enhancement by charge-transfer. Additionally, as the number of unpaired 4f electrons increased, Ln^{3+} in the coordination region attracted oxygen negative charges more strongly, reducing the electric dipole moment of the C-O bond and altering its symmetry.

4.2 Background and research objectives

Lanthanides (Ln), comprising 15 elements with atomic numbers from 57 (La) to 71 (Lu), are crucial rare earth elements [1]. As the atomic number increases, electrons gradually fill the 4f orbitals of Ln [1]. Owing to the electronic configuration of Ln^{3+} ions, which can be expressed as $[Xe]4f^n$ (n=0−14). Lanthanides exhibit similar chemical

properties while possessing abundant energy levels and high-spin states. This unique electronic configuration results in exceptional optical and magnetic properties[1-7], which have led to the widespread use of Ln^{3+} ions and their small molecular complexes in scientific research. For instance, they not only play an important role in functional materials developments, such as the synthesis of luminescent materials [2,3], biomedical probes [3,4], and magnetic resonance imaging (MRI) contrast agents [5], but are also used in quantum computing [6] and spin detection [7]. Furthermore, they are utilized to explore special enhancement phenomena, such as magneto-chiral dichroism enhancement [8] in circularly polarized luminescence [9]. Additionally, lanthanides exhibit a significant characteristic wherein increasing the atomic number enhances the attraction between the nuclear charge and outer electrons due to the weak shielding effect of f-electrons, causing a gradual decrease in the ionic radius of Ln^{3+}, known as lanthanide contraction [1,10,11].

High-performance measurement methods are required to measure the characteristic signals of Ln^{3+} ions effectively. However, measuring low-concentration ($<10^{-5}$M) samples and rapidly obtaining structural information about Ln-molecule complexes using conventional techniques such as nuclear magnetic resonance (NMR)[12], fluorescence [2-4], and electron spin resonance (ESR) spectroscopy [13], remain challenging. Therefore, developing more sensitive and efficient techniques for measuring the characteristic signals of Ln^{3+} ions, particularly in low-concentration($<10^{-5}$M) samples, is an important research focus. Raman spectroscopy is a non-destructive technique that provides molecular fingerprints [14] and vibrational information [15] on Ln-molecule complexes. When a molecule is adsorbed on a noble metal surface, its Raman intensity is enhanced by electromagnetic or chemical effects, such as charge-transfer (CT).[16] This phenomenon known as surface-enhanced Raman scattering

(SERS) [16-18], enables the detection of low concentrations ($<10^{-5}$M) and even single molecules [18]. Thus, SERS is a valuable method for measuring the characteristic signals of Ln^{3+} ions and can be integrated with other standard techniques for multimodal measurement.

However, due to the similar chemical properties of Ln^{3+} ions, their molecular complexes also exhibit similar chemical structures, rendering their vibrational spectra difficult to distinguish [19]. Moreover, because the 4f orbitals are shielded by the 5s and 5p orbitals, they provide a wealth of energy levels while not directly participating in bonding [1]. Consequently, certain Ln^{3+} ions with multiple energy levels [20], such as Pr^{3+}, Nd^{3+}, and Eu^{3+}, may exhibit fluorescence interference in Raman measurements [21,22] or induce resonance Raman effects due to energy absorption [23], further complicating the analysis of Ln-molecule complexes. Thus, the application of SERS to Ln-molecule complexes is limited to some extent, primarily focusing on individual Ln^{3+} ions. Examples include, investigating the effect of Nd^{3+} ions on semiconductor SERS substrates [24], exploring SERS enhancement mechanisms in Gd-complexes [25], and developing MRI-SERS multimodal Gd-fluorescent probes [26]. Our previous research successfully classified La^{3+} and Gd^{3+} ions, which have significant spin differences, using SERS technique [19]. However, the feasibility of using SERS to distinguish other Ln^{3+} ions, particularly those with smaller differences in electronic configuration, such as Pr^{3+} and Nd^{3+}, remains unverified. Additionally, because of the complex 4f electronic configuration of Ln^{3+} ions and pronounced relativistic effects [27], conventional density functional theory (DFT) methods face significant challenges in simulating the SERS spectra of Ln-molecule complexes, although we partly succeeded in simulating the SERS spectra of La-citrate and Gd-citrate complexes [19]. Therefore, simpler and more efficient SERS simulation methods must be developed to assist in the analysis of

experimental SERS spectra and advance the study of Ln-molecule complexes.

In this study, we investigated the relationships between the characteristic peaks in the SERS spectra of Ln-citrate complexes using a combined experimental and computational approach, with a primary focus on understanding how the electronic structure of Ln^{3+} ions governs their spectral behavior, rather than aiming at precise ion identification. Ln with 0-7 (excluding 4) unpaired 4f electrons, representing La, Ce, Pr, Nd, Sm, Eu and Gd, respectively, were selected for this study. Pm, with 4 unpaired 4f electrons, was excluded from the study because of its radioactivity and instability. The SERS spectra of the Ln-citrate complexes were obtained using citrate-capped silver nanoparticle (citrate@AgNP) colloids containing the corresponding Ln^{3+} ions added. Using DFT-simulated SERS spectra for peak assignment, we conducted a detailed analysis of the differences in the SERS spectra and possible mechanisms underlying these differences. These results provide fundamental insights into how the 4f electronic configuration of Ln^{3+} ions indirectly affects their SERS spectral behavior. This understanding lays a foundation for developing more informed approaches to SERS measurement and simulation of Ln-molecular complexes, and for advancing the broader exploration of SERS and coordination chemistry in Ln-molecule complexes.

4.3 Experimental methods and data processing

Chemicals. Six different lanthanide oxides were used to prepare Ln^{3+} solutions. La_2O_3, Pr_6O_{11}, Nd_2O_3, and Gd_2O_3 were sourced from Fujifilm Wako Pure Chemical Corporation (Japan), while Sm_2O_3 and Eu_2O_3 were obtained from Kanto Chemical Co., Inc (Japan). All lanthanide oxides had a purity of > 99%. Ultrapure water from a Direct-Q® UV 3 system (Millipore, USA) was used as the solvent. $Ln(NO_3)_3$ (Ln: La, Pr, Nd, Sm, Eu, and Gd) solutions with a concentration of 0.2 M were prepared by dissolving the corresponding lanthanide oxides in 1 M HNO_3 (Fujifilm Wako Pure Chemical

Corporation, Japan) under heating. These mother solutions were then diluted with ultrapure water to obtain 2×10^{-3} M $Ln(NO_3)_3$ solutions. A 0.2 M $Ce(NO_3)_3$ solution was prepared by dissolving $Ce(NO_3)_3$ crystals (99%, Fujifilm Wako Pure Chemical Corporation, Japan) in ultrapure water. Citrate@AgNPs, colloidal AgNPs dispersed in water and stabilized by surface-bound citrate molecules, were prepared using a modified Lee & Meisel method as described in our previous study[19].

Characterization. Samples for SERS measurements were prepared by adding 50 μL of the 2×10^{-3} M $Ln(NO_3)_3$ solution to 1 mL of citrate@AgNPs, obtaining a concentration of 1×10^{-4} M for each Ln-citrate@AgNPs sample. The samples were stored at room temperature for 12 hours prior to spectroscopic measurements.

For the ultraviolet-visible (UV-Vis) measurements, each SERS sample was diluted 10-fold with ultrapure water, and the measurements were conducted using a UV-Vis-NIR spectrometer (V-770, JASCO, Japan) with a 1 cm path-length polystyrene cuvette. Ultrapure water was used as the blank liquid.

SERS measurements were conducted using clean soda glass capillaries (1.1 ×75 mm, DWK Life Sciences, USA) to hold the sample solutions, which were allowed to stabilize for approximately 8-12 hours before measurement. SERS spectra were then measured using a Raman microscope (T64000, Horiba Scientific, Japan) equipped with a 90X objective using 488, 532 and 660 nm laser at power levels of 50, 50, and 100 mW, respectively. The corresponding energy powers at the sampling points were 101, 85, and 110 mW μm^{-2}, respectively. To avoid sample damage from high-power laser exposure and ensure repeatability, the exposure time for the SERS measurements was set to 30 seconds with 2 accumulations. Raman shift correction was performed using indene.

Spectral analysis was carried out using OriginPro 2022 (OriginLab Corporation,

Northampton, MA, USA.). Baseline removal from the raw spectra was achieved using the interpolation mode, followed by noise reduction using the Savitzky-Golay method applied twice with an 11-point window and polynomial order of 1.

4.4 Improved simulation methods and validation

The simulated SERS spectra of the Ln-citrate complexes on a silver surface were calculated using a simplified model based on our previous work[19]. The Ln-citrate complexes were modeled as $LnCit^-$ using the trisodium citrate structure, which was obtained from the Cambridge Crystallographic Data Centre (CCDC, http://www.ccdc.cam.ac.uk, deposition number: 1478188). To represent the silver surface, a cluster of 11 Ag atoms, approximating the size of the $LnCit^-$ complex, was extracted from a bulk Ag crystal along the (111) plane[28].

Geometry optimization and vibrational spectra calculations were performed using DFT with accurate Hessian matrices in the Gaussian 16 software (Revision C.01, Gaussian, Inc., Wallingford CT, USA)[29]. Vibrational and structural analysis of the optimized systems were performed using the GaussView software (Version 6, Semichem Inc., Shawnee Mission, KS, USA)[30]. The commonly used B3LYP functional is not suitable for transition metals[31,32] and lanthanides[33,34]; the PBE0 functional[35] has been reported to provide better results for Ln-molecule complexes[36] and small molecules[37]. Thus, we employed the PBE0 functional with DFT-D3(BJ) dispersion correction[38] to accurately describe the Ln elements. The solvent environment was modeled as water using the SMD model[39]to replicate the experimental conditions. Considering the significant influence of basis sets on the geometry optimization of trisodium citrate and the Ln-citrate-Ag_{11} complexes, the aug-cc-pvdz basis set[40] was used for C, H, O, and Na, and def2-svpd[41] and def2-tzvpd basis sets[42] for Ag and Ln, respectively. Due to convergence difficulties with some

Ln-citrate complexes, large-core relativistic effective core potentials (ECPs)[43] were consistently used for all Ln^{3+} ions. A large-core ECP replaces all electrons of the ion except for other valence electrons in the 6s, 5s, 5p and 5d orbitals. Thus, based on the number of inner electrons of the Ln^{3+} ion replaced by the ECP, the scalar relativistic large-core ECPs MWB47, MWB48, MWB49, MWB51, MWB52, MWB53, and MWB54 were employed for Ce^{3+}, Pr^{3+}, Nd^{3+}, Sm^{3+}, Eu^{3+}, and Gd^{3+}, respectively, to replace the corresponding small-core ECPs in the def2-tzvpd basis set. The simulated Raman spectra of Ln-citrate-Ag_{11} (simulated SERS spectra of Ln-citrate) were obtained by converting the Raman scattering activity of each vibrational mode to the Raman intensity *I* using the equation (2.6)[44].

The Raman shifts in the simulated SERS spectra were scaled by scaling factors of 0.956 and 0.971 for PBE0-D3(BJ)/aug-cc-pvdz and PBE0-D3(BJ)/def2-tzvpd, respectively, as obtained from the literature [45,46]. The Raman shifts in the region of 1000−1700 cm^{-1} were scaled by a factor of 0.956, and then those in the region of 1000−1250 cm^{-1} (after the first scaling) were scaled by a factor of 0.971 to account for the effects of the Ln^{3+} ions. The full width at half maximum of all simulated SERS spectra was set to 25 cm^{-1} to approximate the experimental spectra.

Additionally, energy calculations of the Ln-citrate-Ag_{11} complexes (Ln: La and Gd) were performed at the PBE0-D3(BJ)/def2-tzvpp [47] level the small- and large-core ECPs to determine the effect of ECP-size on energy. The all-electron basis, x2c-tzvppall [48] were also used for those energy calculations with DKH4 Hamiltonian [49]. All DFT calculation results were analyzed using the Multiwfn software [50,51] (3.8-dev version, Beijing Kein Research Center for Natural Sciences, China).

Due to the complex 4f electronic configuration of lanthanide elements, DFT calculations often struggle with SCF convergence, leading to failed computations. In

this study, we used DFT-based simulations to explore how complexes adsorb onto silver clusters and to perform frequency analysis. According to Xiaoyan Cao' s research [52], energy calculation errors mainly stem from mismatches between the valence basis set and the effective core potential (ECP). Additionally, M. Wang et al. [53] found that while metal complexes are more sensitive to basis set choices than organic molecules, these variations do not cause significant discrepancies.

To investigate this, we analyzed Gd-citrate-Ag_{11} as a case study, comparing frequency calculations using the default def2-tzvpd valence basis set with different ECP sizes for various adsorption conditions (modes), as shown in Figure 4.1. Figures 4.1(a)-(e) illustrate how ECP size affects adsorption between the Gd-citrate complex and the Ag_{11} cluster. We also compared experimental spectra with simulated spectra from five adsorption modes to assess limitations in single-molecule SERS simulations.

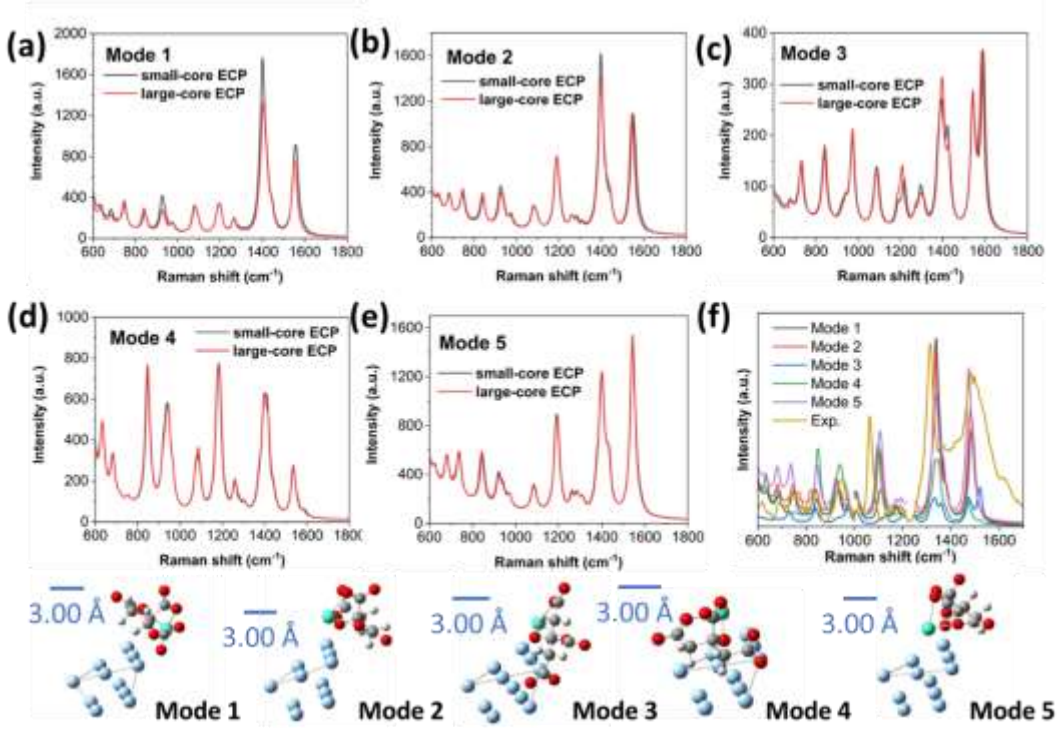

Figure 4.1. Frequency calculations of different adsorption modes between Gd-citrate and the Ag_{11} cluster with different ECP size

Figure 4.1(f) suggests that the experimental spectrum includes signals from

multiple adsorption modes, consistent with real measurements involving high Gd-citrate concentrations. Despite differences in adsorption modes, the same vibrational patterns appear in the experimental spectrum. The effects of ECP size variations on frequency calculation results are minor and acceptable.

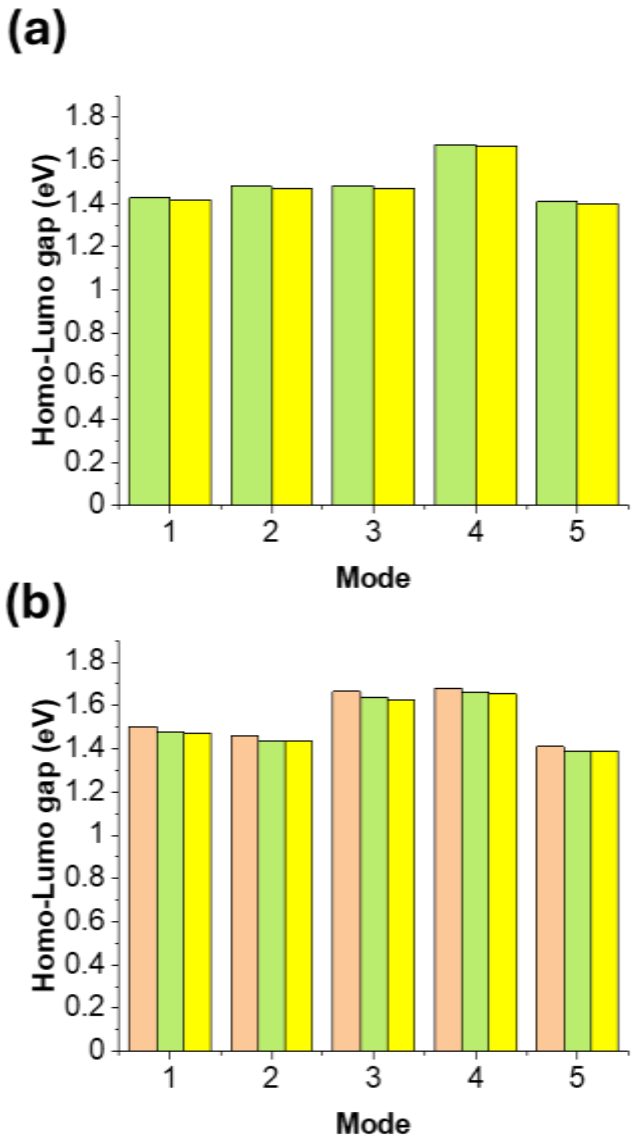

Figure 4.2. HOMO-LUMO energy gap of (a) La-citrate and (b) Gd-citrate from different calculations. Orange: calculated using the def2-tzvpp valence basis set + small-core ECP, Green: calculated using the def2-tzvpp valence basis set + large-core ECP, Yellow: calculated using the all electron basis set x2c-tzvppall.

We also examined La-citrate-Ag_{11} and Gd-citrate-Ag_{11} to evaluate how different ECP sizes affect HOMO-LUMO energy calculations, comparing the results to those

obtained with an all-electron basis set (Figure 4.2). The results show that using a large-core ECP with the same valence basis set produces values closer to those from the more accurate all-electron calculations. This finding confirms that the simplified calculation method used for Ln-citrate in this study is reliable.

4.5 Analysis of experimental SERS spectra

We first compared the SERS spectra (Figures 4.3-4.9) of different samples loaded in capillaries under 488, 532, and 660 nm laser excitation in the range of 450–2000 cm^{-1}. To improve spectral clarity, all spectra were preprocessed by baseline correction and noise reduction. However, cosmic ray spikes were not removed to avoid unintended modification of narrow peak features. All spectra exhibited stable SERS peaks near 737, 940, 1065, 1315, and 1485 cm^{-1}, though the exact peak intensities and profiles varied depending on the sample type and excitation wavelength. Additionally, since the spectra were measured at different measurement points, some spectra displayed extra SERS peaks that were not consistently observed. These variations are attributed to differences in Ag nanoparticle aggregation at different measurement points, leading to spatial variations in hotspot distribution. Such variations also contributed to noticeable differences in the absolute SERS intensity.

Even for the stable peaks at 940, 1065, and 1315 cm^{-1}, their relative intensities varied depending on the measurement point. These differences arose not only from hotspot distribution but also from manual focusing and instrumental fluctuations during signal collection. These factors could also cause slight shifts in peak positions, such as the SERS peak near 940 $cm^{-1,}$ even when the full width at half maximum (FWHM) remained similar.

For a single sample under a single excitation wavelength, the SERS spectra showed only minor variations, and the peaks near 1065, 1315, and 1485 cm^{-1} were

stable and reproducible in terms of Raman shift. The relative intensity ratio between the 1065 and 1315 cm^{-1} peaks exhibited a clear trend that depended on the type of Ln^{3+} ion and was largely unaffected by the excitation wavelength. In contrast, the relative intensity ratio between the 1485 and 1315 cm^{-1} peaks varied with the excitation wavelength and showed weak dependence on the Ln^{3+} species. These trends became more evident after normalization to the 1315 cm^{-1} peak and are consistent with our previous findings. A detailed analysis of these trends is presented in the following section.

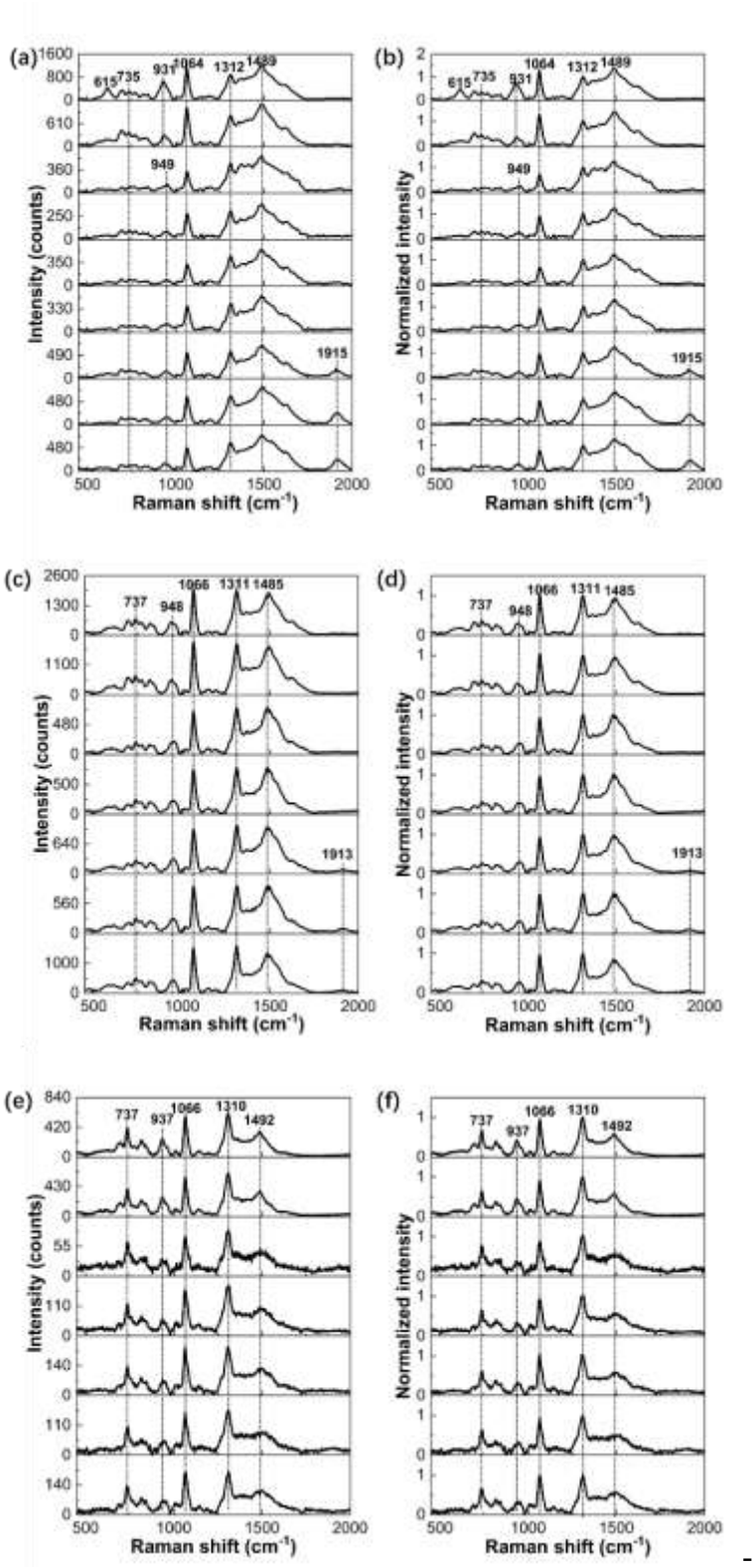

Figure 4.3 (a) and (b): (a)SERS spectra of La-citrate complexes under 488 nm excitation and (b) spectra normalized to the 1312 cm^{-1} peak.(c) and (d): (c)SERS spectra under 532 nm excitation and (d) spectra normalized to the 1311 cm^{-1} peak.(e) and (f): (e)SERS spectra under 660 nm excitation and (f) spectra normalized to the 1310 cm^{-1} peak.

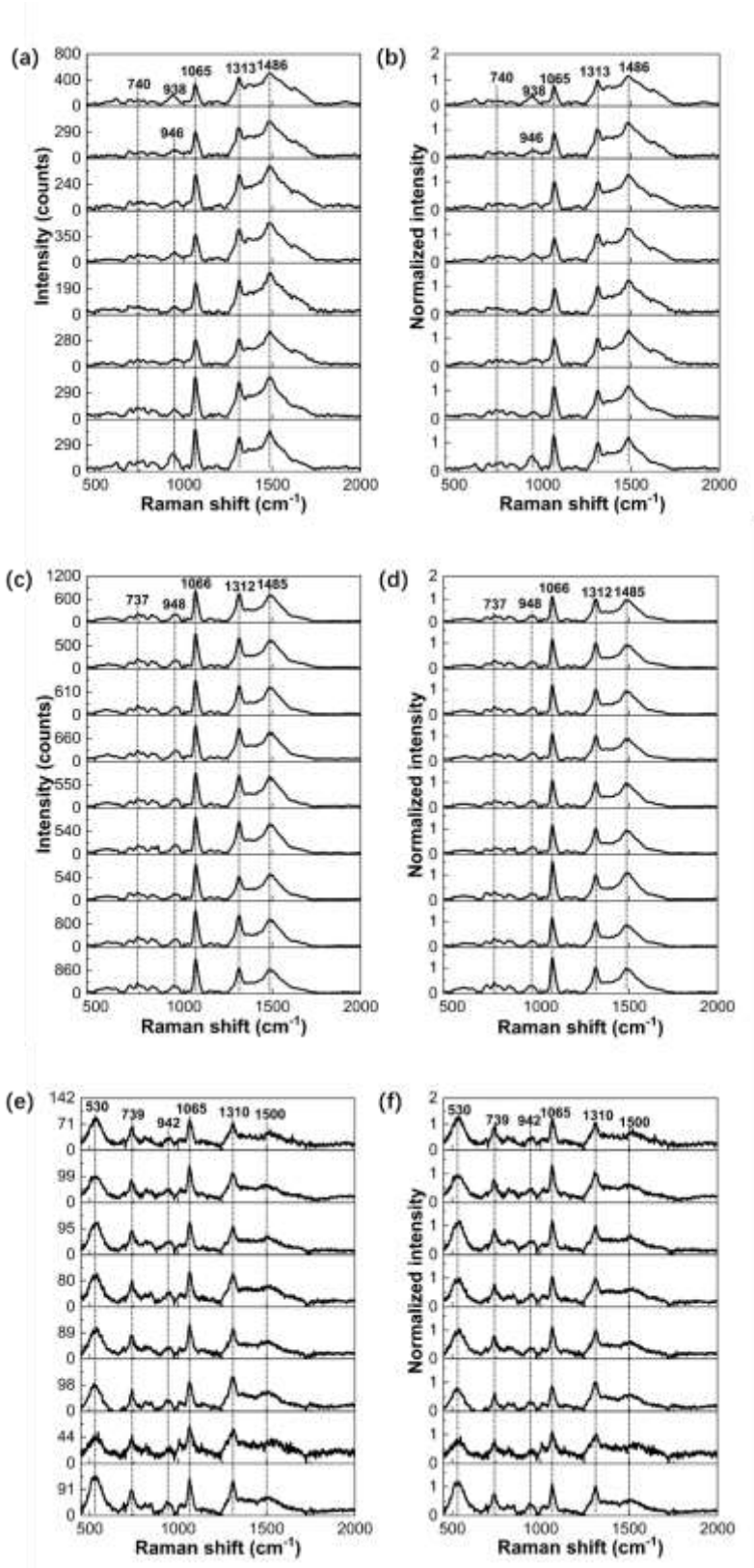

Figure 4.4 (a) and (b): (a)SERS spectra of Ce-citrate complexes under 488 nm excitation and (b) spectra normalized to the 1313 cm^{-1} peak.(c) and (d): (c)SERS spectra under 532 nm excitation and (d) spectra normalized to the 1312 cm^{-1} peak.(e) and (f): (e)SERS spectra under 660 nm excitation and (f) spectra normalized to the 1310 cm^{-1} peak.

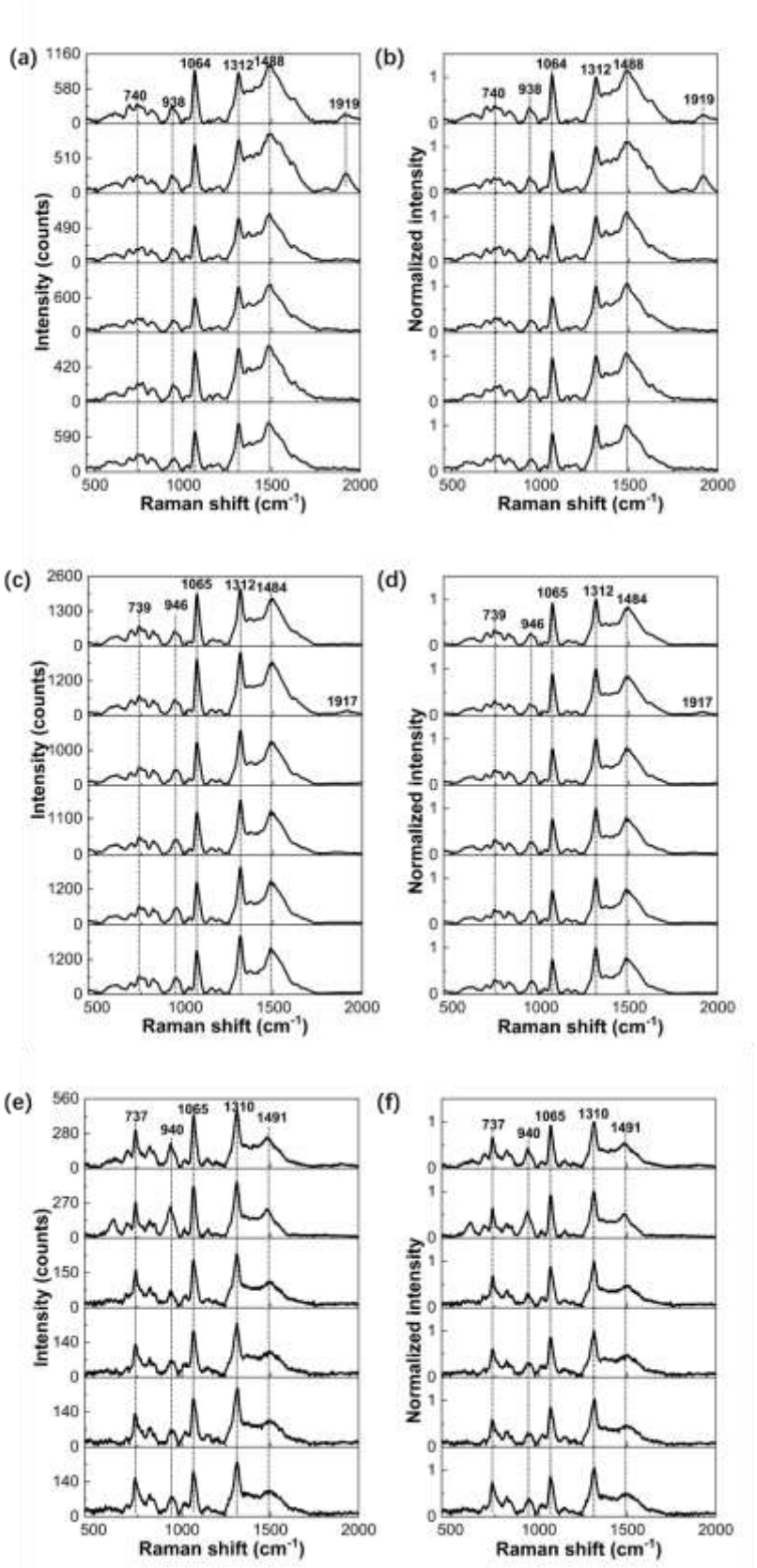

Figure 4.5 (a) and (b): (a)SERS spectra of Pr-citrate complexes under 488 nm excitation and (b) spectra normalized to the 1312 cm^{-1} peak.(c) and (d): (c)SERS spectra under 532 nm excitation and (d) spectra normalized to the 1312 cm^{-1} peak.(e) and (f): (e)SERS spectra under 660 nm excitation and (f) spectra normalized to the 1310 cm^{-1} peak.

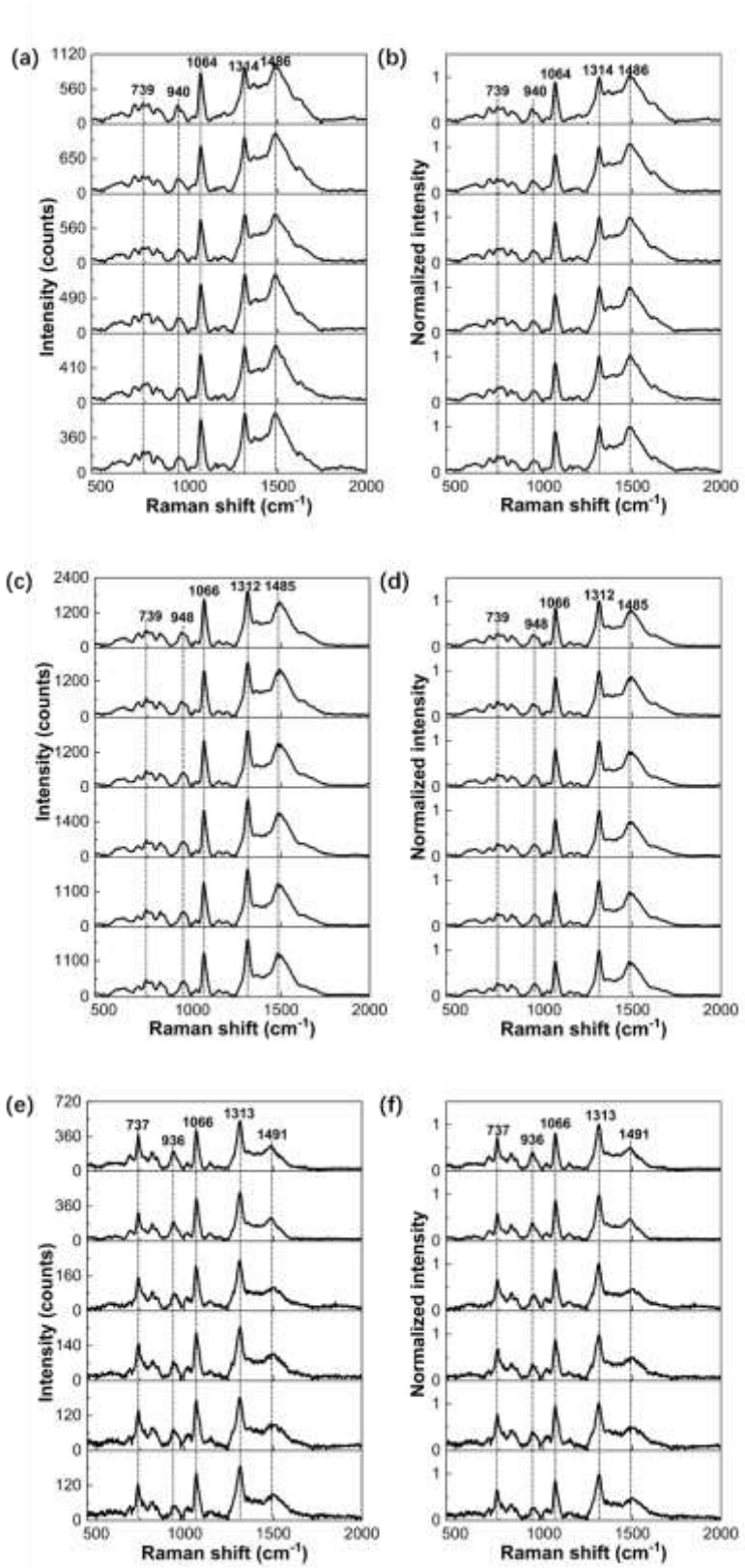

Figure 4.6 (a) and (b): (a)SERS spectra of Nd-citrate complexes under 488 nm excitation and (b) spectra normalized to the 1314 cm^{-1} peak.(c) and (d): (c)SERS spectra under 532 nm excitation and (d) spectra normalized to the 1312 cm^{-1} peak.(e) and (f): (e)SERS spectra under 660 nm excitation and (f) spectra normalized to the 1313 cm^{-1} peak.

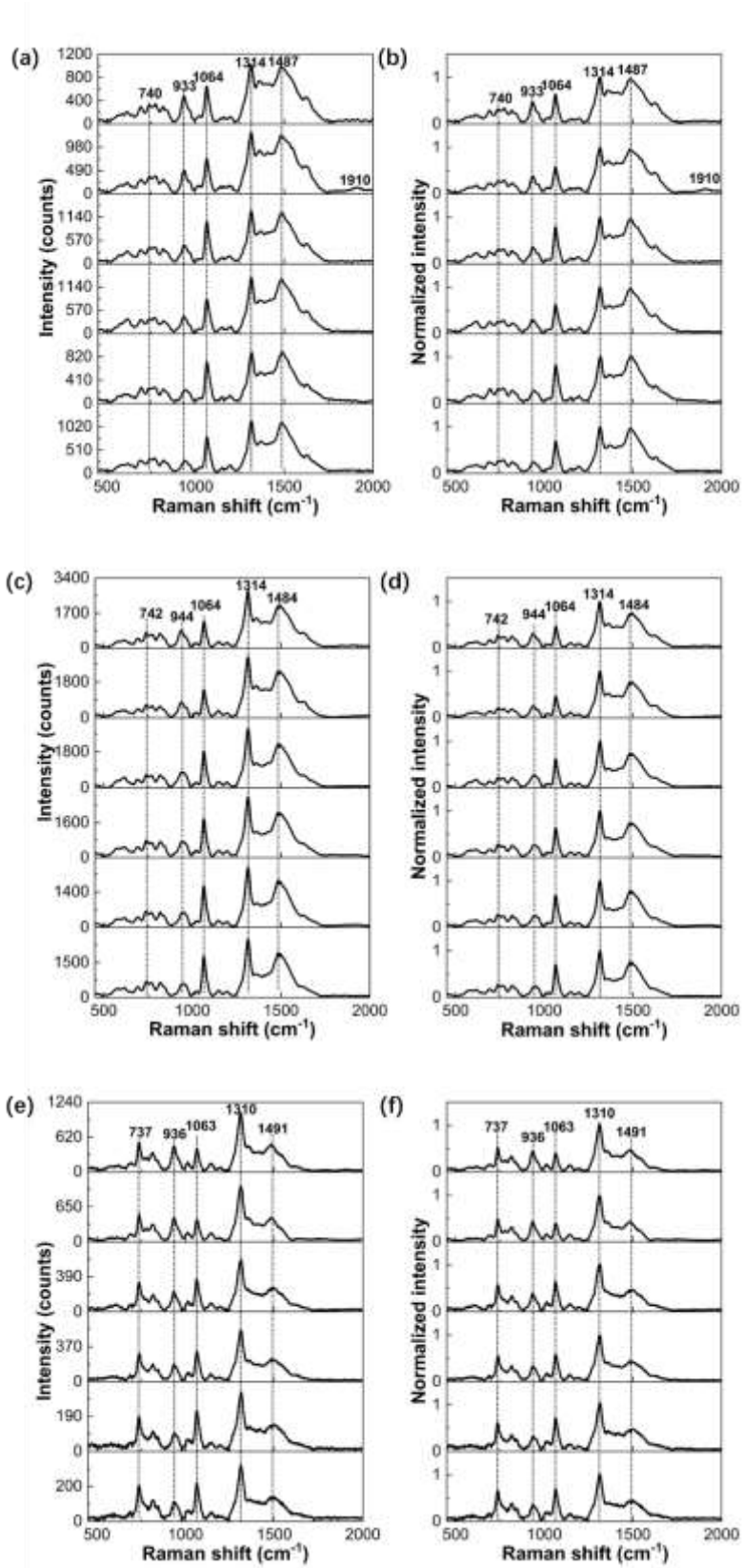

Figure 4.7 (a) and (b): (a)SERS spectra of Sm-citrate complexes under 488 nm excitation and (b) spectra normalized to the 1314 cm^{-1} peak.(c) and (d): (c)SERS spectra under 532 nm excitation and (d) spectra normalized to the 1314 cm^{-1} peak.(e) and (f): (e)SERS spectra under 660 nm excitation and (f) spectra normalized to the 1310 cm^{-1} peak.

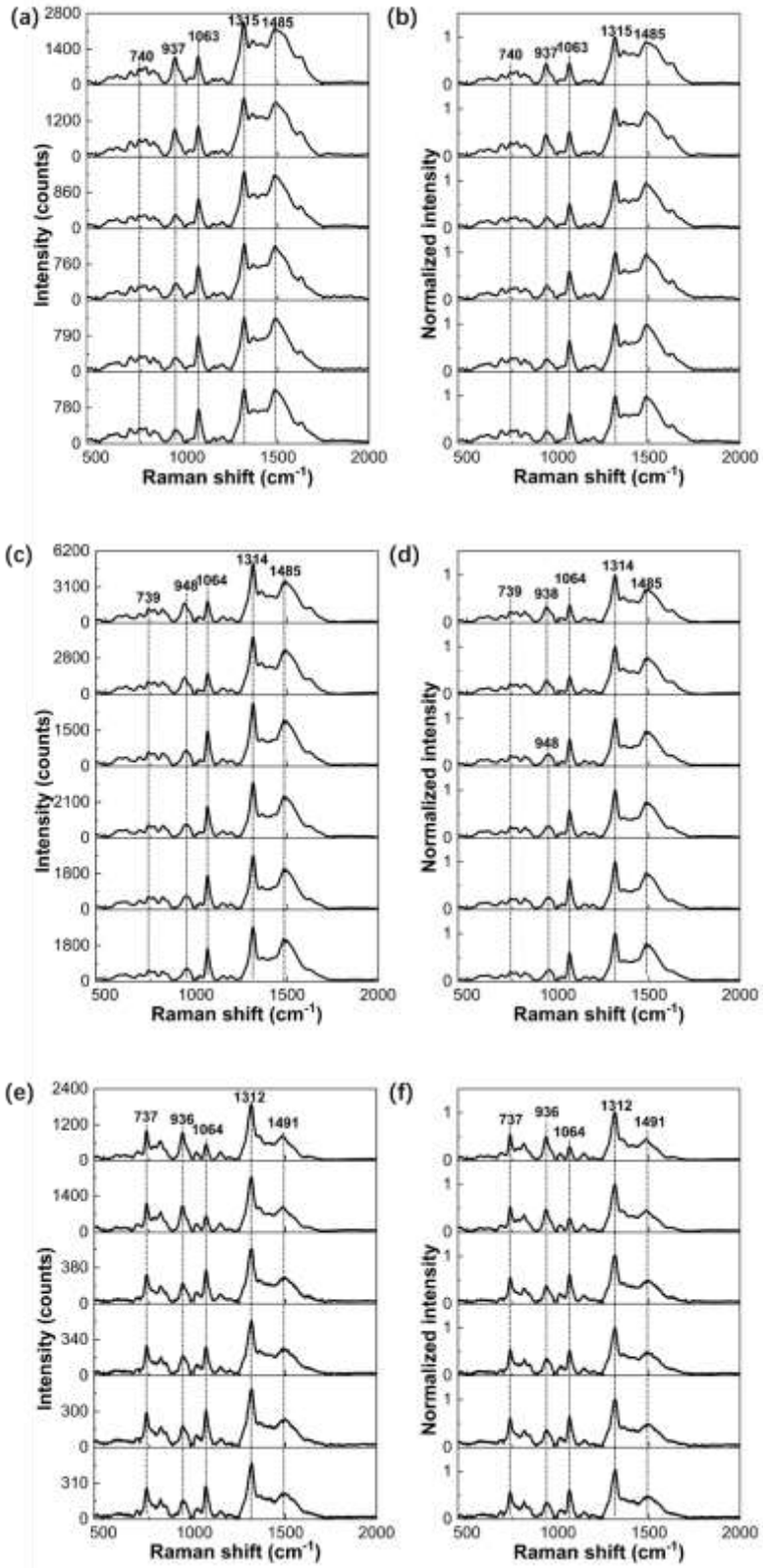

Figure 4.8 (a) and (b): (a)SERS spectra of Eu-citrate complexes under 488 nm excitation and (b) spectra normalized to the 1315 cm^{-1} peak.(c) and (d): (c)SERS spectra under 532 nm excitation and (d) spectra normalized to the 1314 cm^{-1} peak.(e) and (f): (e)SERS spectra under 660 nm excitation and (f) spectra normalized to the 1312 cm^{-1} peak.

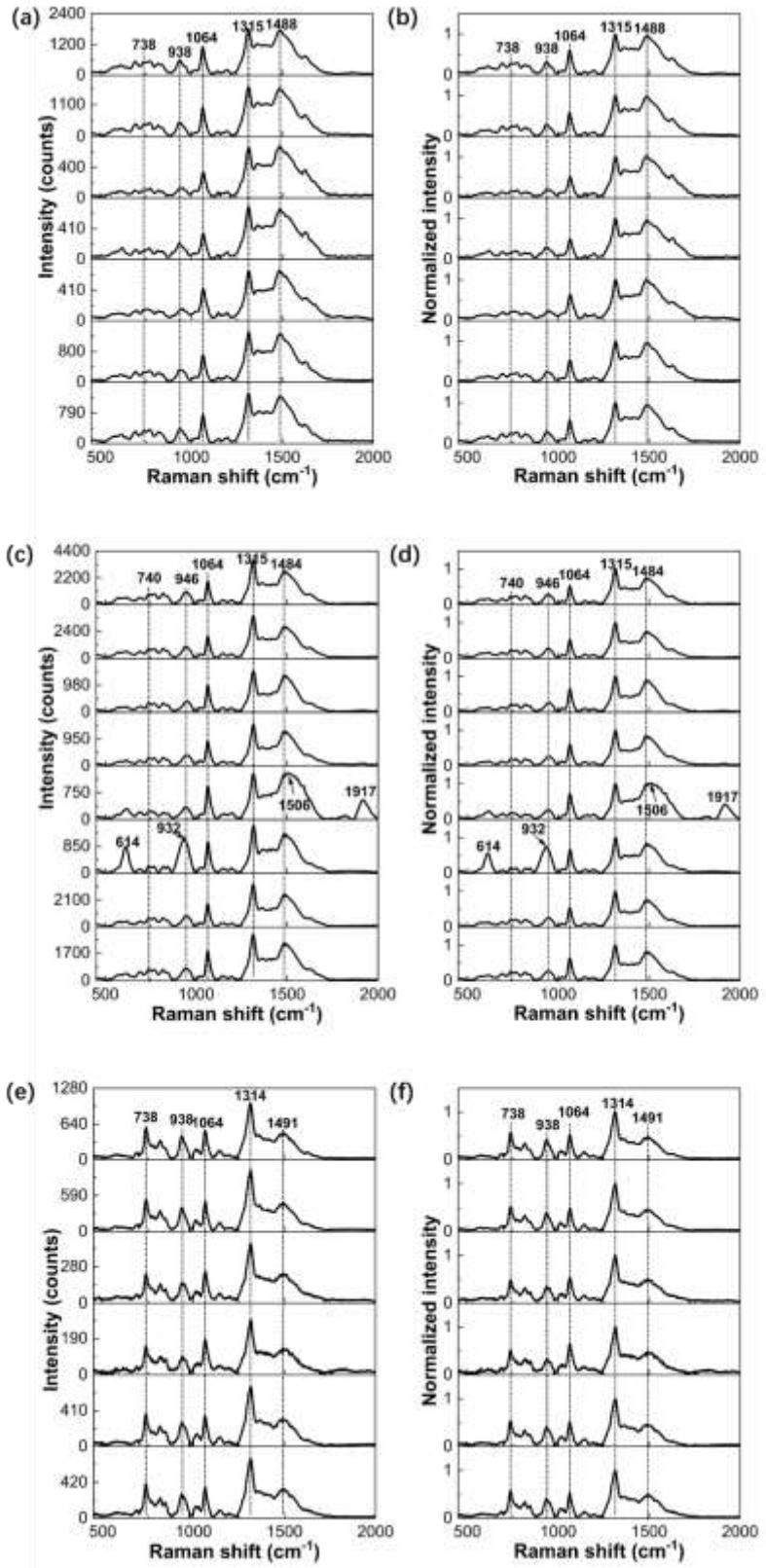

Figure 4.9 (a) and (b): (a)SERS spectra of Gd-citrate complexes under 488 nm excitation and (b) spectra normalized to the 1315 cm^{-1} peak.(c) and (d): (c)SERS spectra under 532 nm excitation and (d) spectra normalized to the 1315 cm^{-1} peak.(e) and (f): (e)SERS spectra under 660 nm excitation and (f) spectra normalized to the 1314 cm^{-1} peak.

4.6 Peak assignment and spectral features analysis

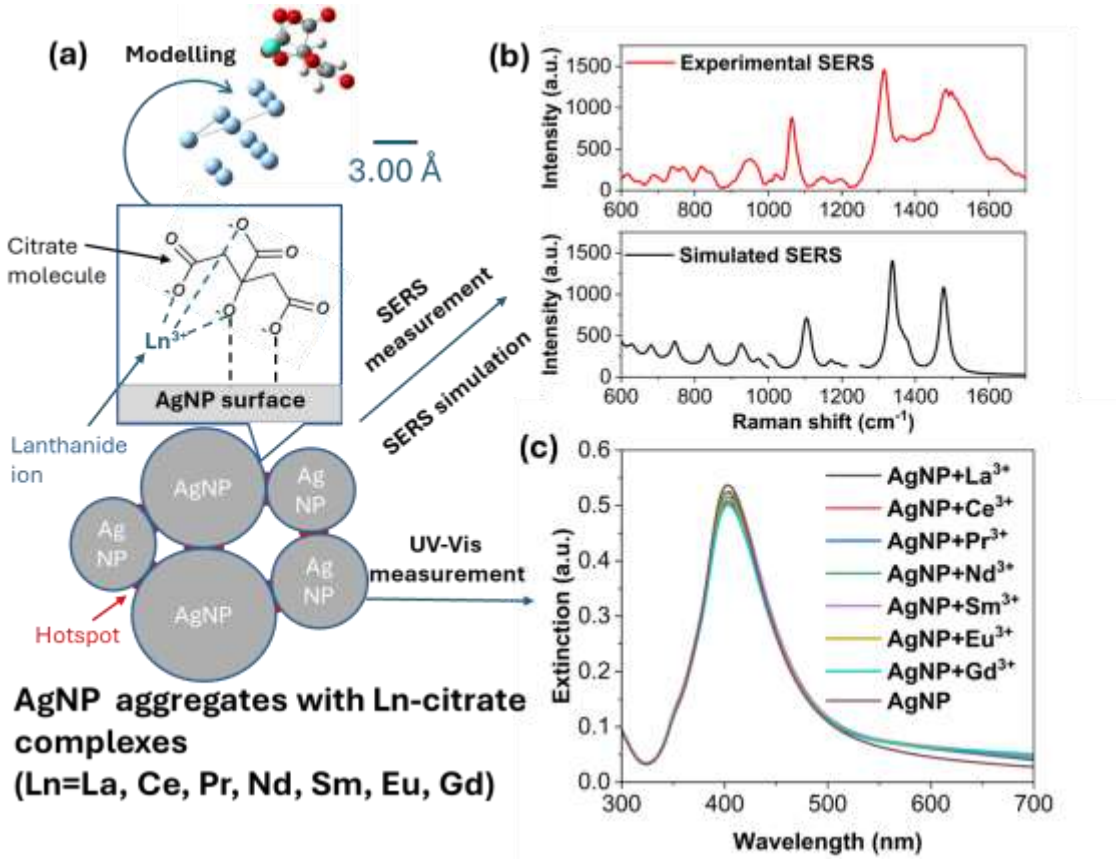

Figure 4.10. (a) Schematic of the research methods used in this study. (b) Experimental and simulated SERS spectra of Gd-citrate. (c) UV-Vis extinction spectra of original citrate@AgNP and Ln-citrate@AgNP samples.

Figure 4.10a shows a schematic diagram of the research methods used in this study. When individual Ln^{3+} ions are added to citrate-capped AgNP colloids, they coordinate to the citrate molecules on the AgNP surface to form Ln-citrate complexes (denoted as Ln-citrate@AgNP, where AgNP serves as the core and Ln-citrate as the shell). Simultaneously, the addition of individual Ln^{3+} ions induces the aggregation of AgNPs. In these aggregates, a strong electromagnetic field is generated by the localized surface plasmon resonance (LSPR) effect when the distance between the AgNPs becomes sufficiently small. The regions with such intense electromagnetic fields are referred to as "hotspots."[16-18] When Ln-citrate complexes are located within these hotspots, their Raman signals are significantly enhanced. To investigate the difference between

the SERS of the Ln-citrate complexes, we performed SERS measurement, UV-Vis measurements, and SERS simulations The SERS spectra were simulated by computer modeling of simplified Ln-citrate@AgNP structures (Ln-citrate-Ag_{11} complexes). As an example, the simulated and experimental SERS spectra of Gd-citrate is shown in Figure 4.3b. The close resemblance between the two spectra enabled the use of the simulated spectrum for vibrational mode analysis and peak assignment. The UV-Vis extinction spectra were also measured to check both the absorption and scattering of light by the AgNPs. Figure 4.10c shows the UV-Vis extinction spectra of the SERS samples diluted 10-fold with ultrapure water. The strong extinction at approximately 400 nm is primarily due to LSPR, where free electrons collectively oscillate in response to light[16]. Thus, the gradual decrease in extinction can be explained by the aggregation of AgNPs as Ln^{3+} ions are added. Table 4.1 summarizes the absorption[54], and emission wavelengths[21] of the different Ln^{3+} ions, along with their electronic configuration, ionic radii, and spin[1].

Table 4.1. Basic information on Ln^{3+}[1,21,54]

Type of Ln^{3+}	Electronic configuration	Ionic radius (pm)	Total spin S	Absorption wavelength (nm)	Emission wavelength (nm)
La^{3+}	$[Xe]4f^0$	103.2	0	None	None
Ce^{3+}	$[Xe]4f^1$	101	1/2	215, 240, 257, 273	320, 339
Pr^{3+}	$[Xe]4f^2$	99	1	442, 590	482, 607, 614, 641
Nd^{3+}	$[Xe]4f^3$	98.3	3/2	355, 455, 525, 580, 680	864, 895, 1053, 1330
Sm^{3+}	$[Xe]4f^5$	95.8	5/2	343, 405, 522	560, 596, 606, 644, 653, 702
Eu^{3+}	$[Xe]4f^6$	94.7	3	316, 396	573, 580, 588, 616, 630, 640, 690, 700
Gd^{3+}	$[Xe]4f^7$	93.8	7/2	275, 308	305, 312

We also analyzed the simulated SERS spectra of selected Ln-citrate (Ln: La, Ce, Pr, Nd, Sm, Eu, and Gd) to assign the SERS peaks based on each vibrational mode (Tables 4.2-4.8). All tables used the same symbols for peak assignment: ν indicates

stretching, ν_{sym} is symmetric stretching, ν_{asym} is asymmetric stretching, δ is in-plane bending and rocking, and γ is out-of-plane wagging and twisting. The calculated SERS frequencies were scaled by using scaling factors.

Table 4.2. The vibrational modes contained in each simulated SERS peak of La-citrate

Simulated SERS peak (cm^{-1})	Vibrational mode (number)	Frequency (cm^{-1})	Assignment
627	32	629	$\delta(COO^-)$
681	33	681	$\delta(COO^-)$
712	34	712	$\delta(COO^-)+\gamma(COO^-)$
745	35	745	$\delta(COO^-)+\gamma(COO^-)$
840	36	840	ν(CCCC-O)
	37	842	ν(CCCC-O)
919	38	917	$\nu(C\text{-}COO^-)$
937	39	934	$\delta(CH_2)$
	40	939	$\delta(CH_2)$
970	41	970	$\nu(C\text{-}COO^-)$
1011	42	996	$\gamma(CH_2)$
	43	1013	$\gamma(CH_2)$
1101	44	1096	$\gamma(CH_2)$
	45	1102	ν(C-O···La)
1170	46	1170	$\gamma(CH_2)$
	47	1187	$\gamma(CH_2)$
1121	48	1211	$\gamma(CH_2)$
1328, 1345	49	1320	$\nu_{sym}(COO^-)$, $\delta(CH_2)$
	50	1326	$\nu_{sym}(COO^-)$, $\delta(CH_2)$
	51	1347	$\nu_{sym}(COO^-)$, $\delta(CH_2)$

	52	1365	$\nu_{sym}(COO^-)$, $\delta(CH_2)$
	53	1375	$\nu_{sym}(COO^-)$, $\delta(CH_2)$
1473	54	1463	$\nu_{asym}(COO^-)$, $\gamma(CH_2)$
	55	1474	$\nu_{asym}(COO^-)$, $\gamma(CH_2)$
	56	1492	$\nu_{asym}(COO^-)$, $\gamma(CH_2)$

Table 4.3. The vibrational modes contained in each simulated SERS peak of Ce-citrate

Simulated SERS peak (cm^{-1})	Vibrational mode (number)	Frequency (cm^{-1})	Assignment
629	32	631	$\delta(COO^-)$
681	33	681	$\delta(COO^-)$
710	34	710	$\delta(COO^-)+ \gamma(COO^-)$
744	35	744	$\delta(COO^-)+ \gamma(COO^-)$
841	36	840	ν(CCCC-O)
	37	842	ν(CCCC-O)
922, 938	38	920	ν(C-COO^-)
	39	936	$\delta(CH_2)$
	40	942	$\delta(CH_2)$
967	41	967	ν(C-COO^-)
1007	42	1001	$\gamma(CH_2)$
	43	1013	$\gamma(CH_2)$
1102	44	1097	$\gamma(CH_2)$
	45	1104	ν(C-O···Ce)
1171	46	1171	$\gamma(CH_2)$

	47	1190	$\gamma(CH_2)$
1250	48	1250	$\gamma(CH_2)$
1343	49	1323	$\nu_{sym}(COO^-)$, $\delta(CH_2)$
	50	1333	$\nu_{sym}(COO^-)$, $\delta(CH_2)$
	51	1346	$\nu_{sym}(COO^-)$, $\delta(CH_2)$
	52	1362	$\nu_{sym}(COO^-)$, $\delta(CH_2)$
	53	1377	$\nu_{sym}(COO^-)$, $\delta(CH_2)$
1478	54	1477	$\nu_{asym}(COO^-)$, $\gamma(CH_2)$
	55	1478	$\nu_{asym}(COO^-)$, $\gamma(CH_2)$
	56	1504	$\nu_{asym}(COO^-)$, $\gamma(CH_2)$

Table 4.4. The vibrational modes contained in each simulated SERS peak of Pr-citrate

Simulated SERS peak (cm^{-1})	Vibrational mode (number)	Frequency (cm^{-1})	Assignment
627	32	629	$\delta(COO^-)$
680	33	681	$\delta(COO^-)$
740	34	713	$\delta(COO^-)+ \gamma(COO^-)$
	35	742	$\delta(COO^-)+ \gamma(COO^-)$
839	36	837	ν(CCCC-O)
	37	840	ν(CCCC-O)
923	38	921	ν(C-COO^-)

	39	935	$\delta(CH_2)$
	40	939	$\delta(CH_2)$
972	41	972	$\nu(C\text{-}COO^-)$
1006	42	1003	$\gamma(CH_2)$
	43	1016	$\gamma(CH_2)$
1106	44	1104	$\gamma(CH_2)$
	45	1111	$\nu(C\text{-}O\cdots Pr)$
1172, 1194	46	1172	$\gamma(CH_2)$
	47	1194	$\gamma(CH_2)$
1254	48	1254	$\gamma(CH_2)$
1339	49	1318	$\nu_{sym}(COO^-)$, $\delta(CH_2)$
	50	1333	$\nu_{sym}(COO^-)$, $\delta(CH_2)$
	51	1339	$\nu_{sym}(COO^-)$, $\delta(CH_2)$
	52	1356	$\nu_{sym}(COO^-)$, $\delta(CH_2)$
1377	53	1377	$\nu_{sym}(COO^-)$, $\delta(CH_2)$
1484	54	1483	$\nu_{asym}(COO^-)$, $\gamma(CH_2)$
	55	1488	$\nu_{asym}(COO^-)$, $\gamma(CH_2)$
	56	1511	$\nu_{asym}(COO^-)$, $\gamma(CH_2)$

Table 4.5. The vibrational modes contained in each simulated SERS peak of Nd-citrate

Simulated SERS	Vibrational mode	Frequency (cm^{-1})	Assignment

peak (cm^{-1})	(number)		
627	32	629	$\delta(COO^-)$
680	33	681	$\delta(COO^-)$
741	34	713	$\delta(COO^-)+ \gamma(COO^-)$
	35	742	$\delta(COO^-)+ \gamma(COO^-)$
840	36	836	ν(CCCC-O)
	37	840	ν(CCCC-O)
922	38	921	$\nu(C\text{-}COO^-)$
	39	934	$\delta(CH_2)$
	40	938	$\delta(CH_2)$
971	41	971	$\nu(C\text{-}COO^-)$
1007	42	1003	$\gamma(CH_2)$
	43	1016	$\gamma(CH_2)$
1105	44	1104	$\gamma(CH_2)$
	45	1111	ν(C-O···Nd)
1172, 1194	46	1172	$\gamma(CH_2)$
	47	1194	$\gamma(CH_2)$
1254	48	1254	$\gamma(CH_2)$
1338	49	1317	$\nu_{sym}(COO^-)$, $\delta(CH_2)$
	50	1332	$\nu_{sym}(COO^-)$, $\delta(CH_2)$
	51	1339	$\nu_{sym}(COO^-)$, $\delta(CH_2)$
	52	1354	$\nu_{sym}(COO^-)$, $\delta(CH_2)$
1378	53	1378	$\nu_{sym}(COO^-)$, $\delta(CH_2)$
1485	54	1483	$\nu_{asym}(COO^-)$,

			$\gamma(CH_2)$
	55	1490	$\nu_{asym}(COO^-)$, $\gamma(CH_2)$
	56	1512	$\nu_{asym}(COO^-)$, $\gamma(CH_2)$

Table 4.6. The vibrational modes contained in each simulated SERS peak of Sm-citrate

Simulated SERS peak (cm^{-1})	Vibrational mode (number)	Frequency (cm^{-1})	Assignment
632	32	632	$\delta(COO^-)$
680	33	680	$\delta(COO^-)$
712	34	712	$\delta(COO^-)+ \gamma(COO^-)$
747	35	747	$\delta(COO^-)+ \gamma(COO^-)$
842	36	839	ν(CCCC-O)
	37	842	ν(CCCC-O)
925	38	922	ν(C-COO^-)
	39	934	$\delta(CH_2)$
	40	941	$\delta(CH_2)$
970	41	970	ν(C-COO^-)
1004	42	1003	$\gamma(CH_2)$
	43	1015	$\gamma(CH_2)$
1107	44	1103	$\gamma(CH_2)$
	45	1113	ν(C-O···Sm)
1173, 1195	46	1173	$\gamma(CH_2)$
	47	1195	$\gamma(CH_2)$
1254	48	1254	$\gamma(CH_2)$
1338, 1378	49	1317	$\nu_{sym}(COO^-)$, $\delta(CH_2)$
	50	1335	$\nu_{sym}(COO^-)$,

			$\delta(CH_2)$
	51	1338	$\nu_{sym}(COO^-)$, $\delta(CH_2)$
	52	1355	$\nu_{sym}(COO^-)$, $\delta(CH_2)$
	53	1381	$\nu_{sym}(COO^-)$, $\delta(CH_2)$
1480	54	1478	$\nu_{asym}(COO^-)$, $\gamma(CH_2)$
	55	1493	$\nu_{asym}(COO^-)$, $\gamma(CH_2)$
	56	1519	$\nu_{asym}(COO^-)$, $\gamma(CH_2)$

Table 4.7. The vibrational modes contained in each simulated SERS peak of Eu-citrate

Simulated SERS peak (cm^{-1})	Vibrational mode (number)	Frequency (cm^{-1})	Assignment
626	32	628	$\delta(COO^-)$
683	33	683	$\delta(COO^-)$
742	34	719	$\delta(COO^-)+ \gamma(COO^-)$
	35	744	$\delta(COO^-)+ \gamma(COO^-)$
847	36	839	ν(CCCC-O)
	37	848	ν(CCCC-O)
930	38	920	$\nu(C\text{-}COO^-)$
	39	934	$\delta(CH_2)$
	40	944	$\delta(CH_2)$
963	41	965	$\nu(C\text{-}COO^-)$
1000	42	1000	$\gamma(CH_2)$
	43	1014	$\gamma(CH_2)$

1101	44	1096	$\gamma(CH_2)$
	45	1108	ν(C-O···Eu)
1167, 1190	46	1167	$\gamma(CH_2)$
	47	1190	$\gamma(CH_2)$
1251	48	1251	$\gamma(CH_2)$
1334	49	1317	$\nu_{sym}(COO^-)$, $\delta(CH_2)$
	50	1331	$\nu_{sym}(COO^-)$, $\delta(CH_2)$
	51	1338	$\nu_{sym}(COO^-)$, $\delta(CH_2)$
	52	1351	$\nu_{sym}(COO^-)$, $\delta(CH_2)$
	53	1369	$\nu_{sym}(COO^-)$, $\delta(CH_2)$
1476	54	1475	$\nu_{asym}(COO^-)$, $\gamma(CH_2)$
	55	1493	$\nu_{asym}(COO^-)$, $\gamma(CH_2)$
	56	1520	$\nu_{asym}(COO^-)$, $\gamma(CH_2)$

Table 4.8. The vibrational modes contained in each simulated SERS peak of Gd-citrate

Simulated SERS peak (cm^{-1})	Vibrational mode (number)	Frequency (cm^{-1})	Assignment
630	32	630	$\delta(COO^-)$
682	33	682	$\delta(COO^-)$
745	34	722	$\delta(COO^-)+\gamma(COO^-)$
	35	746	$\delta(COO^-)+\gamma(COO^-)$

839	36	838	ν(CCCC-O)
	37	840	ν(CCCC-O)
927	38	925	ν(C-COO^-)
	39	935	δ(CH_2)
	40	938	δ(CH_2)
974	41	974	ν(C-COO^-)
1002	42	1000	γ(CH_2)
	43	1015	γ(CH_2)
1104	44	1101	γ(CH_2)
	45	1111	ν(C-O···Gd)
1171, 1192	46	1171	γ(CH_2)
	47	1192	γ(CH_2)
1253	48	1253	γ(CH_2)
1338	49	1318	ν_{sym}(COO^-), δ(CH_2)
	50	1333	ν_{sym}(COO^-), δ(CH_2)
	51	1339	ν_{sym}(COO^-), δ(CH_2)
	52	1363	ν_{sym}(COO^-), δ(CH_2)
	53	1379	ν_{sym}(COO^-), δ(CH_2)
1477	54	1475	ν_{asym}(COO^-), γ(CH_2)
	55	1484	ν_{asym}(COO^-), γ(CH_2)
	56	1512	ν_{asym}(COO^-), γ(CH_2)

We combined experimental measurements with DFT-based peak assignments to analyze the SERS spectra of Ln-citrate complexes. Figures 4.11-4.13 show the experimental SERS spectra collected at 488, 532, and 660 nm, respectively, over the 450-2000 cm^{-1} range, with most signals originating from citrate.

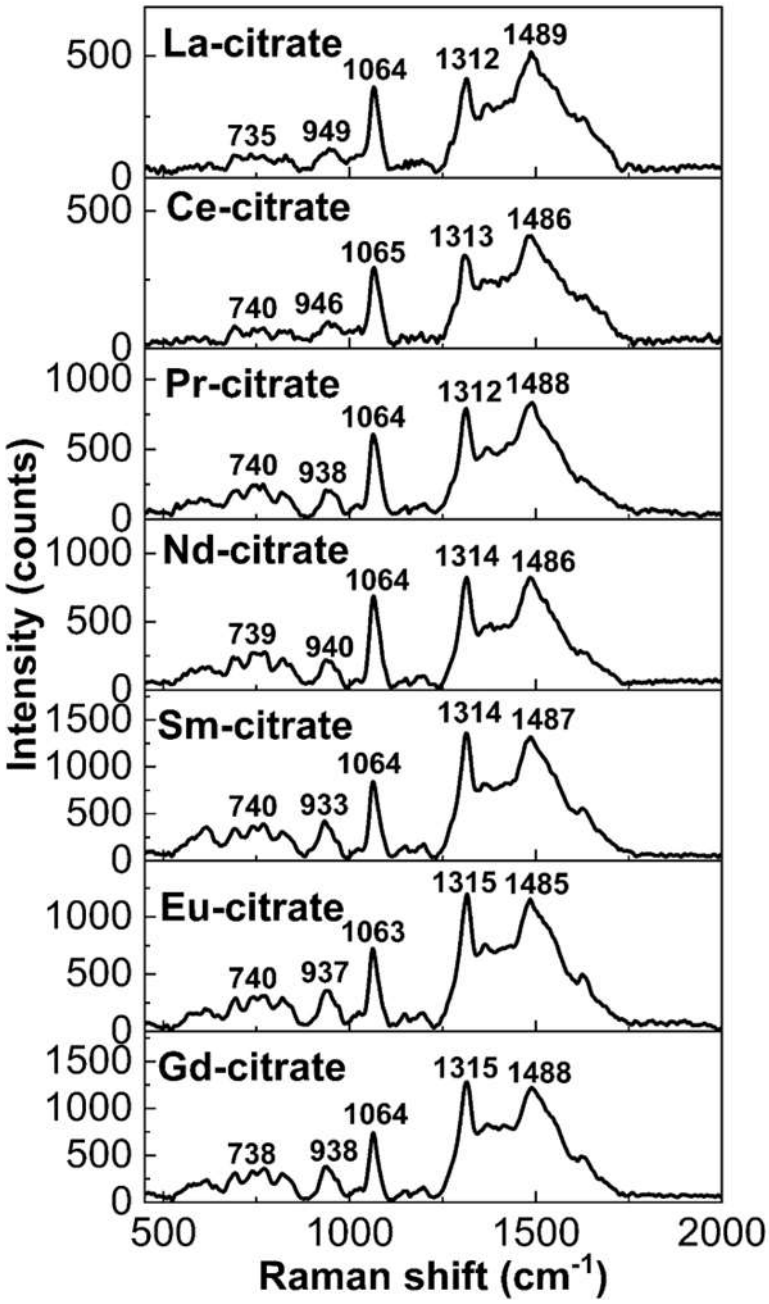

Figure 4.11 SERS spectra of Ln-citrate complexes under excitation at 488 nm.

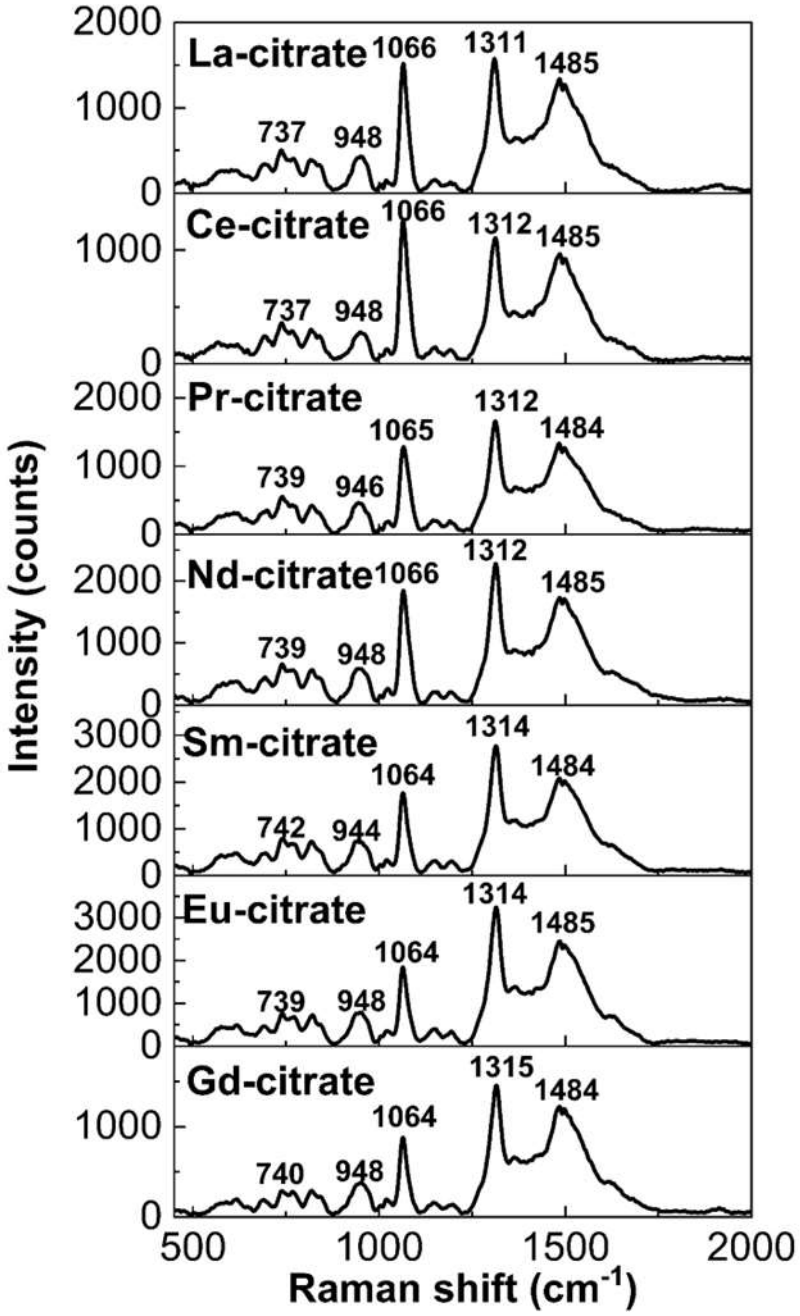

Figure 4.12 SERS spectra of Ln-citrate complexes under excitation at 532 nm.

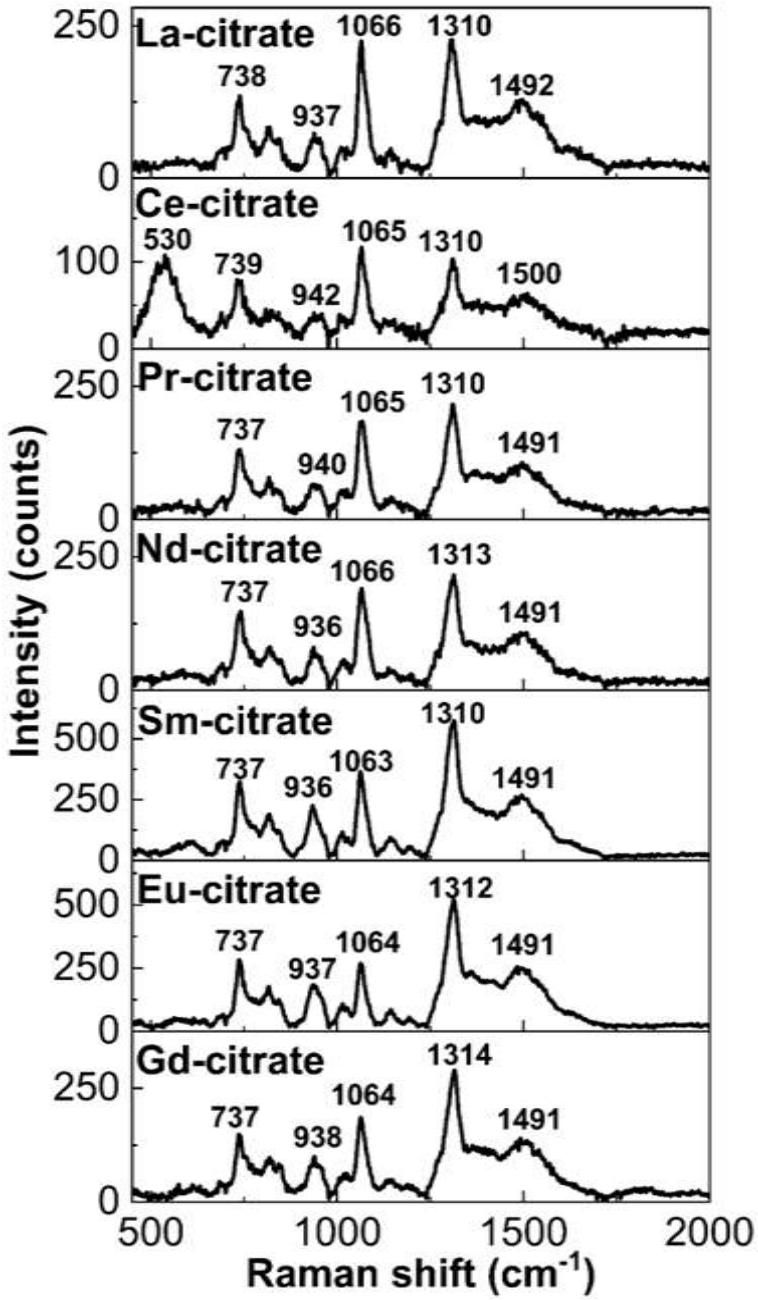

Figure 4.13 SERS spectra of Ln-citrate complexes under excitation at 660 nm.

Although Nd-citrate and Pr-citrate might exhibit pre-resonance Raman effects[23] at 488 nm and 532 nm, respectively (Table 4.1), their spectra did not changes, likely because the resonance in the coordination region was not pronounced. Similarly, the absence of fluorescence for Sm^{3+} and Eu^{3+} can be attributed to quenching[55,56] on the

AgNP surface. Consistent with our previous study[19], the overall similarity in the spectral profiles of the Ln-citrate complexes is attributed to their similar structures. Detailed peak assignments were performed with the aid of DFT simulations (Figure 4.14 and Table 4.9). In the 450-1000 cm^{-1} region (Figures 4.11-4.13), the small peaks around 620 and 700 cm^{-1} were assigned to different $\delta(COO^-)$, peaks around 740,820 and 945 cm^{-1} were assigned to $\delta(COO^-) + \gamma(COO^-)$, ν(CCCC-O) and $\nu(C\text{-}COO^-) + \delta(CH2)$, respectively. Under 488 and 532 nm excitation, the relative intensity differences among these peaks were not significant; however, under 660 nm excitation, the peak near 740 cm^{-1} exhibited a significantly higher relative intensity than the other peaks in this region. In the 1000-1700 cm^{-1} region, the large peaks at approximately 1065, 1315, and 1485 cm^{-1} were ascribed to $\gamma(CH_2) + \nu(C\text{-}O\cdots Ln)$, $\nu_{sym}(COO^-) + \delta(CH_2)$, and $\nu_{asym}(COO^-) + \gamma(CH_2)$, respectively. The peak positions slightly varied depending on both the Ln^{3+} species and excitation wavelength. This can be attributed to a secondary enhancement effect arising from electromagnetic (plasmon resonance variations) and chemical (CT related bond orientation) contributions[16,17,19].

Table 4.9. Peak assignments of Ln-citrate complexes

Type of Ln-citrate	Raman shift (cm^{-1})						
	620, 700	740	820	937, 945	1065	1315	1485(1491*)
La-citrate	δ(COO^-)	δ(COO^-), γ(COO^-)	ν(CCCC–O)	ν(C–COO^-), δ(CH_2)	ν(C–O···La), γ(CH_2)	ν_{sym}(COO^-), δ(CH_2)	ν_{asym}(COO^-), γ(CH_2)
Ce-citrate	δ(COO^-)	δ(COO^-), γ(COO^-)	ν(CCCC–O)	ν(C–COO^-), δ(CH_2)	ν(C–O···Ce), γ(CH_2)	ν_{sym}(COO^-), δ(CH_2)	ν_{asym}(COO^-), γ(CH_2)
Pr-citrate	δ(COO^-)	δ(COO^-), γ(COO^-)	ν(CCCC–O)	ν(C–COO^-), δ(CH_2)	ν(C–O···Pr), γ(CH_2)	ν_{sym}(COO^-), δ(CH_2)	ν_{asym}(COO^-), γ(CH_2)
Nd-citrate	δ(COO^-)	δ(COO^-), γ(COO^-)	ν(CCCC–O)	ν(C–COO^-), δ(CH_2)	ν(C–O···Nd), γ(CH_2)	ν_{sym}(COO^-), δ(CH_2)	ν_{asym}(COO^-), γ(CH_2)
Sm-citrate	δ(COO^-)	δ(COO^-), γ(COO^-)	ν(CCCC–O)	ν(C–COO^-), δ(CH_2)	ν(C–O···Sm), γ(CH_2)	ν_{sym}(COO^-), δ(CH_2)	ν_{asym}(COO^-), γ(CH_2)
Eu-citrate	δ(COO^-)	δ(COO^-), γ(COO^-)	ν(CCCC–O)	ν(C–COO^-), δ(CH_2)	ν(C–O···Eu), γ(CH_2)	ν_{sym}(COO^-), δ(CH_2)	ν_{asym}(COO^-), γ(CH_2)
Gd-citrate	δ(COO^-)	δ(COO^-), γ(COO^-)	ν(CCCC–O)	ν(C–COO^-), δ(CH_2)	ν(C–O···Gd), γ(CH_2)	ν_{sym}(COO^-), δ(CH_2)	ν_{asym}(COO^-), γ(CH_2)

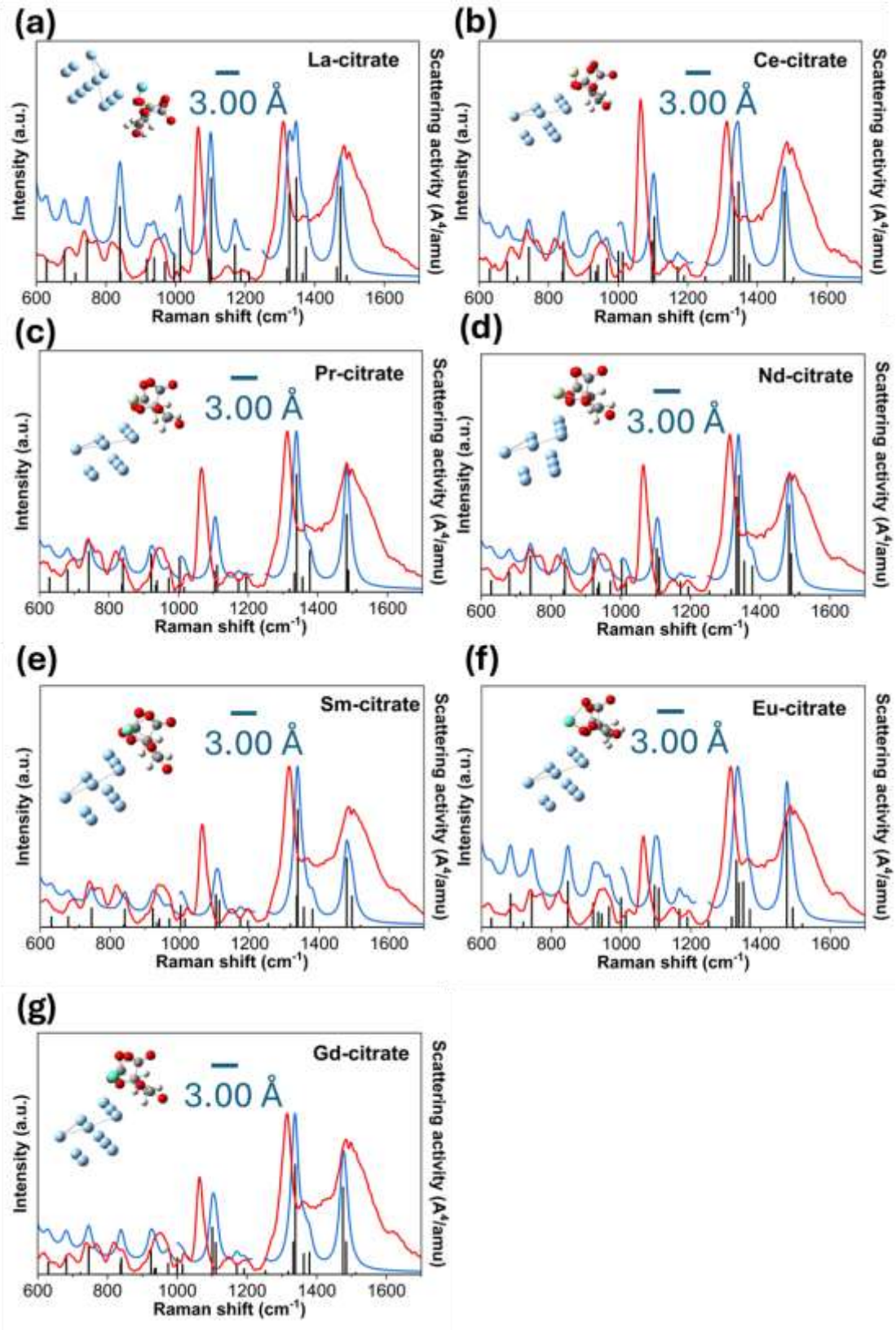

Figure 4.14. Experimental SERS spectra (red curves) at 1×10^{-4} M, calculated vibrational modes (black curves), and simulated SERS spectra (blue curves) for (a) La-citrate, (b) Ce-citrate, (c) Pr-citrate, (d) Nd-citrate, (e) Sm-citrate, (f) Eu-citrate, and (g) Gd-citrate. As shown in the structures, all simulations were based on a single-

molecule SERS model. Some regions between 1000 cm^{-1} and 1213-1250 cm^{-1} were missing due to double scaling when the spectra were exported to Multiwfn. However, this has no effect on the results because there are no vibrational modes in these missing regions.

Complementarily, Figure 4.14 presents the experimental SERS spectra of the Ln-citrate complexes under 532 nm excitation, alongside their simulated spectra and the optimized structures of Ln-citrate-Ag_{11} clusters. The simulated spectra accurately reproduced the principal peaks observed experimentally beyond 1000 cm^{-1}, despite some discrepancies in the other regions. These differences can be attributed to several factors: (i) Experimental SERS signals arise from multiple enhancement mechanisms and are influenced by the laser frequency, whereas simulated spectra are computed under a static external field (zero frequency)[57] representing the ground-state CT effect[16,17]; (ii) The simulation considers only a single Ln-citrate adsorption mode on the Ag_{11} cluster, which does not capture the complexity of the multi-molecular adsorption modes present in experiments(Figure 4.1). (iii) Inherent limitations of the DFT approach, including influences from the solvent environment and basis set selection, may lead to Raman shift errors that can be scaled using frequency scaling factors[19,58,59]. In addition, the effect of the ECP-size on the simulation results was verified to be at acceptable levels (Figures 4.1 and 4.2). Thus, although the absolute intensities from the DFT-calculated SERS spectra may not be directly comparable to the experimental values, the scaled Raman shifts provide a reliable basis for accurate peak assignment.

We also analyzed the effect of the excitation wavelength on the SERS spectrum of each individual Ln-citrate complex. The relative intensity of the peaks at approximately 1065 and 1315 cm^{-1} under 488 nm excitation was similar to that under 532 nm excitation. However, the relative intensity of the peaks at approximately 1315 and 1485

cm^{-1} differed significantly at these two excitation wavelengths. This is consistent with our previous study[19], which indicated that as the excitation wavelength moves further away from the LSPR peak (around 400 nm), the peak around 1315 cm^{-1} becomes stronger relative to the peak near 1485 cm^{-1}. Furthermore, at an excitation wavelength of 660 nm, the signal-to-noise ratio decreased, leading to a reduction in spectral quality while the relationship of relative intensities of each peaks became even more pronounced. The characteristic peak around 1485 cm^{-1} shifted to 1491 cm^{-1}, and its relative intensity is lower than that of the peak near 690 cm^{-1}. This significantly lower SERS peak intensity under 660 nm excitation compared with those under 488 and 532 nm excitation can be explained by two reasons. The first reason is that the 660 nm laser has a lower frequency, resulting in a lower Raman scattering intensity than those at excitation wavelengths of 488 nm and 532 nm. The Raman scattering intensity I_{mn}, corresponding to the transition from state m to state n, is described by equations (2.4) and (2.5)[60,61]:

Equation (2.4) indicates that the Raman scattering intensity is proportional to the fourth power of the scattered light frequency $v_i \pm v_{mn}$. As $v_i \gg v_{mn}$, the Raman scattering intensity is considered proportional to the fourth power of the incident light frequency v_i.The second reason is that under 660 nm excitation, the LSPR intensity in the range corresponding to the Raman shift is lower compared to that under 488 nm and 532 nm excitation, resulting in a lower SERS intensity. Notably, only the SERS spectrum of Ce-citrate exhibited a broad peak near 527 cm^{-1} under 660 nm excitation, although the mechanism responsible for its appearance remains unclear.

4.7 Ion-dependent spectral variations and mechanistic analysis

Furthermore, we compared the relative intensities of the peaks around 1065, 1315

and 1485 cm^{-1} in the experimental SERS spectra of various Ln-citrate complexes at different excitation wavelengths (Figures 4.15 and 4.16). The relative intensities of the SERS peaks, SERS intensity ratios, were obtained by normalizing the peak intensity around 1065 or 1485 cm^{-1} to the peak near 1315 cm^{-1}. Notably, due to limitations in our experimental conditions, SERS detection of Pm^{3+} was not performed. However, to facilitate analysis of the effect of the number of unpaired 4f electrons of Ln^{3+} on the SERS spectra, Pm^{3+} was included as a blank reference.

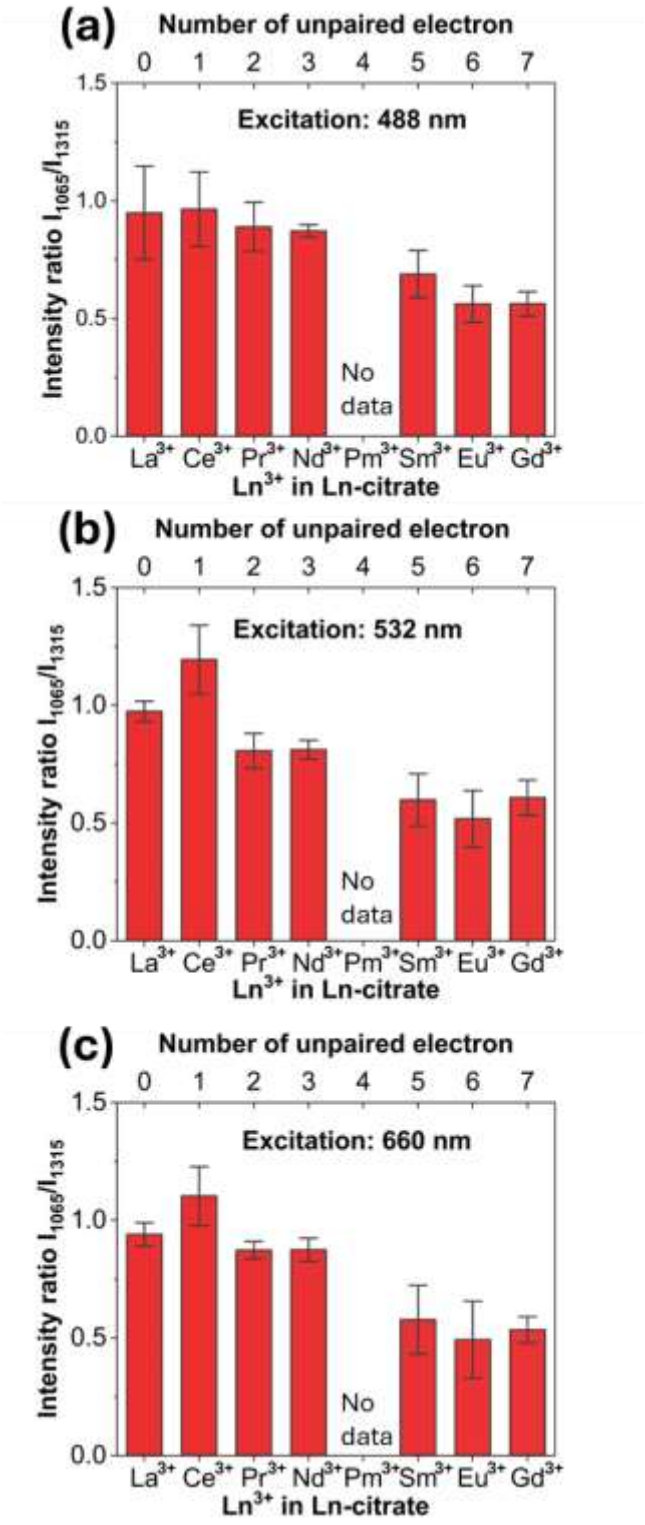

Figure 4.15. SERS intensity ratio I_{1065}/I_{1315} under excitation at (a) 488 nm, (b) 532 nm, and (c) 660 nm. The SERS intensity ratios were obtained by normalizing the peak intensity around 1065 or 1485 cm^{-1} to that near 1315 cm^{-1}. The measurement times (N) for La–citrate through Gd–citrate were N = 9, 8, 6, 6, 6, 6, and 7, respectively, under 488 nm excitation. N = 7, 9, 6, 6, 6, 6, and 8, respectively, under 532 nm excitation; and N = 7, 8, 6, 6, 6, 6, and 6, respectively, under 660 nm excitation. Error bars indicate ± SD.

Figures 4.15 show the values of the SERS intensity ratio I_{1065}/I_{1315} under 488, 532, and 660 nm excitation, respectively. I_{1065}/I_{1315} did not vary with the excitation wavelengths. Conversely, except for an anomaly with Ce^{3+}, which will be discussed later, I_{1065}/I_{1315} decreased with increasing number of unpaired 4f electrons, particularly when that number exceeded 4. Thus, I_{1065}/I_{1315} contains information on the type of Ln^{3+} ion. However, I_{1065}/I_{1315} is nearly identical for Ln^{3+} ions with similar electronic configurations, limiting its use to distinguishing only ions with significantly different electronic configurations, i.e. La^{3+} and Gd^{3+}[19].

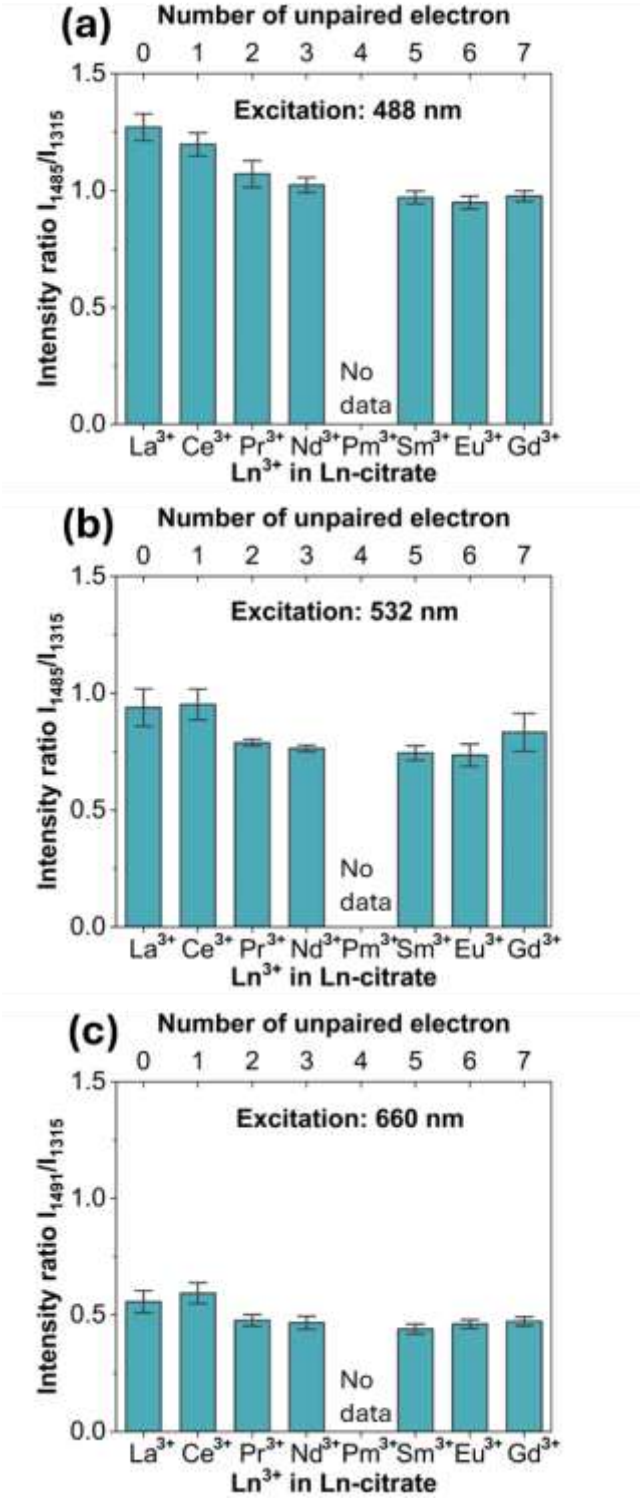

Figure 4.16. SERS intensity ratio of I_{1485}/I_{1315} under laser excitation at (a) 488 nm, (b) 532 nm, and (c) 660 nm. Notably, when the excitation wavelength is 660 nm, the peak around 1485 cm^{-1} shifted to 1491 cm^{-1}. The SERS intensity ratios were obtained by normalizing the peak intensity around 1065 or 1485 cm^{-1} to that near 1315 cm^{-1}. The measurement times (N) for La–citrate through Gd–citrate were N = 9, 8, 6, 6, 6, 6, and 7, respectively, under 488 nm excitation. N = 7, 9, 6, 6, 6, 6, and 8, respectively, under 532 nm excitation; and N = 7, 8, 6, 6, 6, 6, and 6, respectively, under 660 nm excitation. Error bars indicate ± SD.

Figures 4.16 show the values of the SERS intensity ratio I_{1485}/I_{1315} under 488, 532, and 660 nm laser excitation, respectively. I_{1485}/I_{1315} increased as the excitation wavelength decreased. The trends I_{1065}/I_{1315} and I_{1485}/I_{1315} are consistent with those observations in our previous work. As mentioned earlier, the SERS peaks around 1065, 1315 and 1485 cm^{-1} were assigned as $\gamma(CH_2)+\nu(C\text{-}O\cdots Ln)$, $\nu_{sym}(COO^-)+\gamma(CH_2)$, and $\nu_{asym}(COO^-)+\gamma(CH_2)$, respectively. According to the CT mechanistic model[16,17], all three SERS peaks reflect excitation energy dependency. I_{1065}/I_{1315} and I_{1485}/I_{1315} illustrate the relationship between peak intensities at approximately 1065 and 1485 cm^{-1} and that around 1315 cm^{-1} as the excitation wavelength changes. Notably, only the peak around 1485 cm^{-1} exhibited a significant response to wavelength variation, with its intensity increasing as the wavelength decreased. This trend was consistently observed for the SERS spectra of all Ln-citrate complexes; thus, it can be considered to originate from the intrinsic vibrational characteristics of citrate. As citrate does not exhibit absorption near 488 nm [62] and $\nu_{asym}(COO^-)$ includes the asymmetric vibrational mode of COO^- coordinated to Ag[19,58], the wavelength-dependent variation of I_{1485}/I_{1315} can be attributed to the additional enhancement of $\nu_{asym}(COO^-)$ + $\gamma(CH_2)$ due to the CT effect. In addition, at all excitations, I_{1485}/I_{1315} generally decreased as the number of unpaired 4f electrons in Ln^{3+} ions increased. However, this trend did not hold for Ce-citrate under 532 and 660 nm excitation, and Gd-citrate under 488, 532, and 660 nm excitation.

At all excitation wavelengths, Ce-citrate exhibited the highest I_{1065}/I_{1315}, surpassing that of La-citrate. However, under 488 nm excitation, this ratio did not show a significant increase compared with those under 532 and 660 nm excitations. Although statistical variations may exist because of the limited number of spectra, at least six

measurements confirmed that the I_{1065}/I_{1315} of Ce-citrate is wavelength-dependent. This suggests that Ce-citrate exhibits an additional response to non-resonant wavelengths. However, due to experimental constraints, the underlying mechanism remains unclear and will be explored in future studies.

To explore the possible mechanism underlying the ion-dependent variation of I_{1065}/I_{1315} and I_{1485}/I_{1315} in the SERS spectra, we further analyzed the influence of the Ln^{3+} ions by comparing the variation with "lanthanide contraction." [1]. Figures 4.17 and 4.18, compare the relationship between lanthanide contraction and I_{1065}/I_{1315} or I_{1485}/I_{1315}, respectively, under different excitation wavelengths. Notably, due to the lack of experimental data for Pm^{3+}, its probable trend is represented by a dashed line.

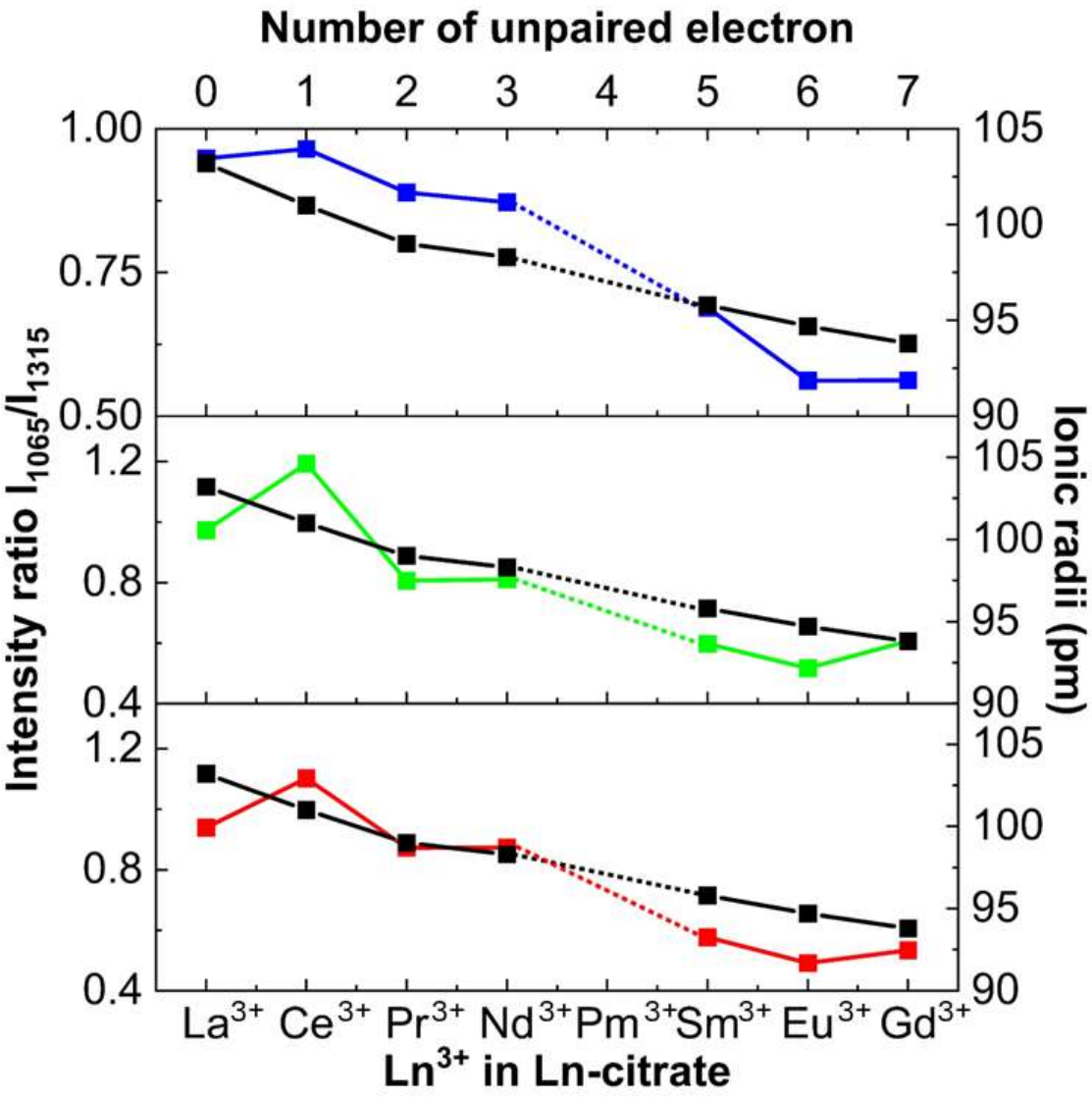

Figure 4.17. Comparison of lanthanide contraction (black line) with the SERS intensity ratios I_{1065}/I_{1315}, measured under 488 nm (blue line), 532 nm (green line), and 660 nm (red line) excitation.

As shown in Figure 4.17, except for Ce^{3+}, I_{1065}/I_{1315} decreased with an increase in the number of unpaired 4f electrons in the Ln^{3+} ion. This trend was similar to lanthanide contraction and was not affected by the excitation wavelength. The main vibration in v(C-O···Ln) contributing to the peak around 1065 cm^{-1} originated from the C-O bond. Therefore, except for Ce^{3+}, the variation in I_{1065}/I_{1315} induced by the coordination of the C-O bond to different Ln^{3+} ions. This trend can be explained by two complementary

mechanisms grounded in the molecular electronic structure. (i) As lanthanide contraction progresses with increasing 4f electron count, the Ln^{3+} ion exhibits stronger electrostatic attraction toward coordinating oxygen atoms. This pulls electron density from the C–O bond toward the metal center, thereby reducing the charge separation and the effective electric dipole of the C–O···Ln. In the context of equations 2.4 and 2.5, formalism for Raman scattering, the transition electric dipole moment between the ground and virtual electronic states plays a key role in determining the polarizability. A decrease in transition electric dipole moment weakens the equation 2.5 contribution to the polarizability tensor and reduces the Raman intensity of the ν(C–O···Ln) mode near 1065 cm^{-1}. (ii) Concurrently, the increased coordination strength and structural compaction caused by lanthanide contraction lead to reduced molecular symmetry in the coordination environment. As a result, the vibrational mode involving the C–O bond experiences a diminished polarizability derivative ($\partial\alpha/\partial Q$), further suppressing its Raman activity. Although symmetry breaking may activate certain vibrational modes, the specific combination of stronger metal–ligand interaction and lower anisotropic electron cloud distribution generally reduces the magnitude of the polarizability change during vibration. The combined effect of the reduced transition dipole moment and the diminished polarizability derivative ($\partial\alpha/\partial Q$) leads to a lower Raman intensity at 1065 cm^{-1}. Consequently, the intensity ratio I_{1065}/I_{1315} decreases progressively with increasing 4f electron occupancy. These two effects reduction in transition dipole moment and suppression of $\partial\alpha/\partial Q$ which act synergistically to lower the Raman intensity at 1065 cm^{-1} relative to the internal symmetric COO^- mode near 1315 cm^{-1}, thereby explaining the observed decrease in the I_{1065}/I_{1315} ratio with increasing 4f occupancy.

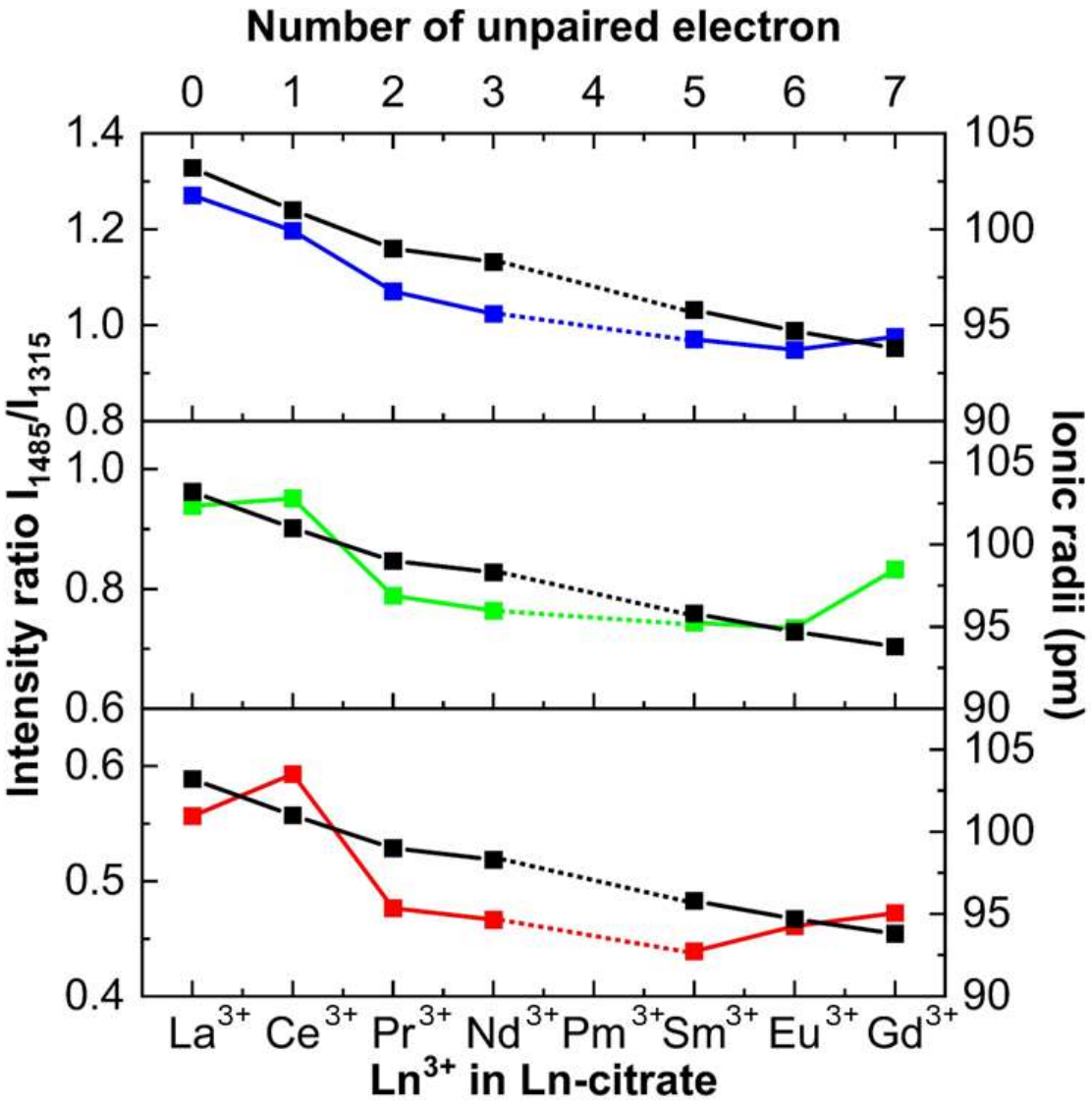

Figure 4.18. Comparison of lanthanide contraction (black line) with the SERS intensity ratios I_{1485}/I_{1315}, measured under 488 nm (blue line), 532 nm (green line), and 660 nm (red line) excitation.

Under 488 nm excitation, the trend in I_{1485}/I_{1315} was almost consistent with lanthanide contraction, with a slight increase for all ions except Gd^{3+} (Figure 4.18). However, under 532 nm excitation, the I_{1485}/I_{1315} values of Ce^{3+} and Gd^{3+} were higher than those of the preceding Ln^{3+} ions. Under 660 nm excitation, the I_{1485}/I_{1315} values of Ce^{3+}, Eu^{3+}, and Gd^{3+} were also higher than those of the previous Ln^{3+} ions. Therefore, at these two excitation wavelengths, the trend in I_{1485}/I_{1315} differed completely from

lanthanide contraction. Two of the three COO^- groups in citrate are coordinated to Ln^{3+}; hence, the attraction between Ln^{3+} and the negative charge on oxygen increases with the number of unpaired 4f electrons. This results in a lower dipole moment of the C-O bond and reduces the symmetry of the COO^- electron cloud. Therefore, except for some Ln^{3+} ions, I_{1485}/I_{1315} generally decreases as the number of unpaired electrons increases. However, because the peaks near 1315 and 1485 cm^{-1} represent overlapping SERS signals from the three COO groups of citrate and the peak near 1485 cm^{-1} is additionally enhanced by the CT effect, the influence of Ln^{3+} ions is irregular and showed weak variability.

Although the variation in the relative intensity ratios of characteristic SERS peaks is not directly governed by the lanthanide contraction, it indirectly reflects the extent of electronic structure differences among Ln^{3+} ions. For instance, Pr^{3+} and Nd^{3+} exhibit electronic configurations of $[Xe]4f^2$ and $[Xe]4f^3$, respectively, and differ in ionic radius around only 0.7 pm. Consistently, their I_{1065}/I_{1315} ratios are nearly identical. A similar trend is observed for Eu^{3+} ($[Xe]4f^6$) and Gd^{3+} ($[Xe]4f^7$), which show a radius difference of 0.9 pm and exhibit comparable I_{1065}/I_{1315} values around 0.5. In contrast, La^{3+} ($[Xe]4f^0$) and Gd^{3+} ($[Xe]4f^7$) differ markedly in both 4f electron occupation and ionic radius (9.4 pm), with their I_{1065}/I_{1315} ratio differing by approximately 4.5.

These findings suggest that while relative peak intensity ratios such as I_{1065}/I_{1315} may not suffice for unequivocal identification of closely related Ln^{3+} ions, they are sensitive to broader differences in 4f electron configuration and ionic character. This spectral sensitivity offers a useful foundation for the development of future SERS-based strategies aimed at probing and classifying lanthanide ions based on their electronic structure.

In addition, although Ln^{3+} ions have significant mass differences, their impact on

the vibrational modes of the peaks at approximately 1065,1315 and 1485 cm^{-1} is minimal. Therefore, the mass difference does not significantly affect the SERS spectra.

4.8 Summary

This work aims to uncover how variations in the 4f electron configuration of Ln^{3+} ions modulate their vibrational spectral behavior, rather than to develop a classification method. We successfully measured the SERS spectra of selected Ln-citrate complexes (Ln: La, Ce, Pr, Nd, Sm, Eu, and Gd) at a concentration of 1×10^{-4} M under excitation wavelengths of 488, 532, and 660 nm. The experimental spectra showed three major SERS peaks at approximately 1065, 1315, and 1485 cm^{-1}, with no detectable resonance Raman effect or fluorescence signal, despite theoretical predictions. The simulated SERS spectra of the Ln-citrate complexes were successfully calculated using an optimized DFT computational method that directly replaced the small-core ECPs in the def2-tzvpd basis set with large-core ECPs, enabling detailed vibrational analysis and peak assignment. SERS intensity ratios were obtained by normalizing the peak intensity I at 1065 or 1485 cm^{-1} to the that near 1315 cm^{-1}. I_{1065}/I_{1315} was not affected by the excitation wavelength but depended on the type of Ln^{3+} ion. In contrast, I_{1485}/I_{1315} increased with decreasing excitation wavelength, reflecting additional enhancement by the CT effect. Both I_{1065}/I_{1315} and I_{1485}/I_{1315} decreased as the number of unpaired 4f electrons in the Ln^{3+} ion increased, except for Ce^{3+}, Eu^{3}, and Gd^{3+}. Although this trend was similar to lanthanide contraction, the mechanism was different. Analysis of the Ln^{3+} coordination region suggested that as the number of unpaired 4f electrons increases, Ln^{3+} becomes more strongly attracted to the negative charges on oxygen. Thus, the electric dipole moment of the C-O bond and its symmetry decrease. Because of current experimental limitations, we did not specifically study the unique peak of Ce-citrate or

the potential SERRS effect of Nd-citrate. These topics will be investigated in our future work. The findings of the present study provide effective guidance and reference for the vibrational spectroscopy studies of other lanthanides and even actinides.

4.9 References

(1) Simon Cotton. *Lanthanide and Actinide Chemistry*; John Wiley & Sons, Ltd, 2006; pp 9– 102.

(2)Kotyk, C. M.; Weber, J. E.; Hyre, A. S.; McNeely, J.; Monteiro, J. H. S. K.; Domin, M.; Balaich, G. J.; Rheingold, A. L.; de Bettencourt-Dias, A.; Doerrer, L. H. Luminescence of Lanthanide Complexes with Perfluorinated Alkoxide Ligands. I*norg. Chem.* 2020, 59 (14), 9807– 9823

(3)Eliseeva, S. V.; Bünzli, J.-C. G. Lanthanide Luminescence for Functional Materials and Bio-Sciences. *Chem. Soc. Rev.* 2010, 39 (1), 189– 227

(4)Wang, G.; Peng, Q.; Li, Y. Lanthanide-Doped Nanocrystals: Synthesis, Optical-Magnetic Properties, and Applications. *Acc. Chem. Res.* 2011, 44 (5), 322– 332

(5)Lee, H. Y.; Jee, H. W.; Seo, S. M.; Kwak, B. K.; Khang, G.; Cho, S. H. Diethylenetriaminepentaacetic Acid–Gadolinium (DTPA-Gd)-Conjugated Polysuccinimide Derivatives as Magnetic Resonance Imaging Contrast Agents. *Bioconjugate Chem.* 2006, 17 (3), 700– 706

(6)Serrano, D.; Kuppusamy, S. K.; Heinrich, B.; Fuhr, O.; Hunger, D.; Ruben, M.; Goldner, P. Ultra-Narrow Optical Linewidths in Rare-Earth Molecular Crystals. *Nature* 2022, 603 (7900), 241– 246

(7)Sushkov, A. O.; Chisholm, N.; Igor Lovchinsky; Kubo, M.; Lo, P.-C.; Bennett, S.; Hunger, D.; Akimov, A. V.; Walsworth, R. L.; Park, H.; Lukin, M. D. All-Optical Sensing of a Single-Molecule Electron Spin. *Nano Letters* 2014, 14 (11), 6443–6448

(8)Li, C.-Y.; Langit Cahya Adi; Paillot, K.; Breslavetz, I.; Long, L.-S.; Zheng, L.-S.; Geert L. J. A. Rikken; Train, C.; Kong, X.-J.; Matteo Atzori. Enhancement of Magneto-Chiral Dichroism Intensity by Chemical Design: The Key Role of Magnetic-Dipole Allowed Transitions. *Journal of the American Chemical Society* 2024, 146 (24), 16389–16393

(9)Lunkley, J. L.; Dai Shirotani; Kazuaki Yamanari; Sumio Kaizaki; Muller, G. Extraordinary Circularly Polarized Luminescence Activity Exhibited by Cesium Tetrakis(3-Heptafluoro-Butylryl-(+)-Camphorato) Eu(III) Complexes in EtOH and $CHCl_3$ Solutions. *Journal of the American Chemical Society* 2008, 130 (42), 13814–13815

(10)Geoffroy Ferru; Reinhart, B.; Bera, M. K.; Olvera, M.; Qiao, B.; Ellis, R. J. The Lanthanide Contraction beyond Coordination Chemistry. *Chemistry–A European Journal* 2016, 22(20), 6899-6904.

(11)Seitz, M.; Oliver, A. G.; Raymond, K. N. The Lanthanide Contraction Revisited. *Journal of the American Chemical Society* 2007, 129 (36), 11153–11160

(12)Ivanova, V. Yu.; Shurygin, I. D.; Chevela, V. V.; Ajsuvakova, O. P.; Semenov, V. E.; Bezryadin, S. G. New Aspects of Complex Formation in the Gadolinium(III)–Citric Acid System in Aqueous Solution. *Comments on Inorganic Chemistry* 2022, 42 (2), 109– 144

(13)Baggio, R.; Calvo, R.; Garland, M. T.; Peña, O.; Perec, M.; Rizzi, A. C. Gadolinium and neodymium citrates: Evidence for weak ferromagnetic exchange between gadolinium (III) cations. *Inorg. Chem.* 2005, 44 (24), 8979– 8987

(14)Cao, Y. C. Nanoparticles with Raman Spectroscopic Fingerprints for DNA and RNA Detection. *Science* 2002, 297 (5586), 1536–1540.

(15)Rudolph, W. W.; Irmer, G. Raman Spectroscopic Characterization of Light Rare

Earth Ions: La^{3+}, Ce^{3+}, Pr^{3+}, $Nd^{3+}$and Sm^{3+}– Hydration and Ion Pair Formation. *Dalton Transactions* 2017, 46 (13), 4235–4244.

(16)Itoh, T.; Procházka, M.; Dong, Z.-C.; Ji, W.; Yamamoto, Y. S.; Zhang, Y.; Ozaki, Y. Toward a New Era of SERS and TERS at the Nanometer Scale: From Fundamentals to Innovative Applications. *Chem. Rev.* 2023, 123 (4), 1552– 1634

(17)Yamamoto, Y. S.; Itoh, T. Why and How Do the Shapes of Surface-Enhanced Raman Scattering Spectra Change? Recent Progress from Mechanistic Studies. *Journal of Raman Spectroscopy* 2016, 47 (1), 78–88.

(18)Nie, S.; Emory, S. R. Probing Single Molecules and Single Nanoparticles by Surface-Enhanced Raman Scattering. *Science* 1997, 275 (5303), 1102– 1106

(19)Jin, H.; Itoh, T.; Yamamoto, Y. S. Classification of La^{3+} and Gd^{3+} Rare-Earth Ions Using Surface-Enhanced Raman Scattering. *The Journal of Physical Chemistry C* 2024, 128 (13), 5611–5620.

(20)Peijzel, P. S.; Meijerink, A.; Wegh, R. T.; Reid, M. F.; Burdick, G. W. A Complete $4f^n$ Energy Level Diagram for All Trivalent Lanthanide Ions. *Journal of Solid State Chemistry* 2005, 178 (2), 448–453.

(21)Hagemann, H.; Ayoubipour, S.; Delgado, T.; Schnyder, C.; Gnos, E. Probing Luminescence of Rare Earth Ions in Natural Pink Fluorites Using Raman Microscopes. *Journal of Raman Spectroscopy* 2022, 53 (8), 1464–1470.

(22)Lenz, C.; Nasdala, L.; Talla, D.; Hauzenberger, C.; Seitz, R.; Kolitsch, U. Laser-Induced REE^{3+} Photoluminescence of Selected Accessory Minerals — an "Advantageous Artefact" in Raman Spectroscopy. Chemical Geology 2015, 415, 1–16.

(23)Albrecht, A. On the Theory of Raman Intensities. *Journal of Chemical Physics* 1961, 34 (5), 1476–1484.

(24)Yang, S.; Yao, J.; Quan, Y.; Hu, M.; Su, R.; Gao, M.; Han, D.; Yang, J. Monitoring

the Charge-Transfer Process in a Nd-Doped Semiconductor Based on Photoluminescence and SERS Technology. *Light: Sci. Appl.* 2020, 9 (1), 117

(25)López-Neira, J. P.; Galicia-Hernández, J. M.; Reyes-Coronado, A.; Pérez, E.; Castillo-Rivera, F. Surface Enhanced Raman Scattering of Amino Acids Assisted by Gold Nanoparticles and Gd^{3+} Ions. *J. Phys. Chem. A* 2015, 119 (18), 4127– 4135,

(26)Liu, Y.; Chang, Z.; Yuan, H.; Fales, A. M.; Vo-Dinh, T. Quintuple-Modality (SERS-MRI-CT-TPL-PTT) Plasmonic Nanoprobe for Theranostics. *Nanoscale* 2013, 5 (24), 12126

(27)Seth, M.; Dolg, M.; Fulde, P.; Schwerdtfeger, P. Lanthanide and Actinide Contractions: Relativistic and Shell Structure Effects. *Journal of the American Chemical Society* 1995, 117 (24), 6597–6598

(28)Grimme, S.; Antony, J.; Ehrlich, S.; Krieg, H. A Consistent and Accurate Ab Initio Parametrization of Density Functional Dispersion Correction (DFT-D) for the 94 Elements H-Pu. *J. Chem. Phys.* 2010, 132 (15), 15410

(29)Gaussian 16, Revision C.01, Frisch, M. J.; Trucks, G. W.; Schlegel, H. B.; Scuseria, G. E.; Robb, M. A.; Cheeseman, J. R.; Scalmani, G.; Barone, V.; Petersson, G. A.; Nakatsuji, H. et al . Gaussian, Inc., Wallingford CT, 2016.

(30)GaussView, Version 6.1, Roy Dennington, Todd A. Keith, and John M. Millam, Semichem Inc., Shawnee Mission, KS, 2016.

(31)Paier, J.; Marsman, M.; Kresse, G. Why Does the B3LYP Hybrid Functional Fail for Metals?. *J. Chem. Phys.* 2007, 127 (2), 024103

(32)Minenkov, Y.; Singstad, Å.; Occhipinti, G.; Jensen, V. R. The Accuracy of DFT-Optimized Geometries of Functional Transition Metal Compounds: A Validation Study of Catalysts for Olefin Metathesis and Other Reactions in the Homogeneous Phase. *Dalton Transactions* 2012, 41 (18), 5526.

(33)Martins, C.; Jorge, F. E.; Franco, M. L.; Ferreira, I. B. All-Electron Gaussian Basis Sets of Double Zeta Quality for the Actinides. *Journal of chemical physics* 2016, 145 (24).

(34)Roca-Sabio, A.; Regueiro-Figueroa, M.; Esteban-Gómez, D.; de Blas, A.; Rodríguez-Blas, T.; Platas-Iglesias, C. Density Functional Dependence of Molecular Geometries in Lanthanide(III) Complexes Relevant to Bioanalytical and Biomedical Applications. *Computational and Theoretical Chemistry* 2012, 999, 93–104.

(35)Adamo, C.; Barone, V. Toward Reliable Density Functional Methods without Adjustable Parameters: The PBE0Model. *J. Chem. Phys.* 1999, 110 (13), 6158– 6170

(36)Chen, X.; Chen, T.-T.; Li, W.-L.; Lu, J.-B.; Zhao, L.-J.; Jian, T.; Hu, H.-S.; Wang, L.-S.; Li, J. Lanthanides with Unusually Low Oxidation States in the PrB3- and PrB4- Boride Clusters. *Inorg. Chem.* 2019, 58 (1), 411– 418

(37)Brémond, É.; Savarese, M.; Su, N. Q.; Pérez-Jiménez, Á. J.; Xu, X.; Sancho-García, J. C.; Adamo, C. Benchmarking Density Functionals on Structural Parameters of Small- /Medium-Sized Organic Molecules. *J. Chem. Theory Comput.* 2016, 12 (2), 459– 465

(38)Grimme, S.; Ehrlich, S.; Goerigk, L. Effect of the damping function in dispersion corrected density functional theory. *J. Comput. Chem*. 2011, 32, 1456– 1465,

(39)Marenich, A. V.; Cramer, C. J.; Truhlar, D. G. Universal Solvation Model Based on Solute Electron Density and on a Continuum Model of the Solvent Defined by the Bulk Dielectric Constant and Atomic Surface Tensions. *The Journal of Physical Chemistry B* 2009, 113 (18), 6378–6396.

(40)Dunning, T. H. Gaussian Basis Sets for Use in Correlated Molecular Calculations. I. The Atoms Boron through Neon and Hydrogen. *J. Chem. Phys*. 1989, 90 (2), 1007–1023,

(41)Andrae, D.; Häußermann, U.; Dolg, M.; Stoll, H.; Preuß, H. Energy-Adjustedab

Initio Pseudopotentials for the Second and Third Row Transition Elements. *Theoretica Chimica Acta* 1990, 77 (2), 123– 141

(42)Rappoport, D. Property-Optimized Gaussian Basis Sets for Lanthanides. *J. Chem. Phys.* 2021, 155 (12), 124102

(43)Dolg, M.; Stoll, H.; Savin, A.; Preuss, H. Energy-Adjusted Pseudopotentials for the Rare Earth Elements. *Theor. Chim. Acta* 1989, 75 (3), 173– 194

(44)Liu, Z.; Lu, T.; Chen, Q. Vibrational Spectra and Molecular Vibrational Behaviors of All-Carboatomic Rings, Cyclo[18]Carbon and Its Analogues. *Chemistry – An Asian Journal* 2020, 16 (1), 56–63.

(45)Kashinski, D. O.; Chase, G. M.; Nelson, R. G.; Di Nallo, O. E.; Scales, A. N.; VanderLey, D. L.; Byrd, E. F. C. Harmonic Vibrational Frequencies: Approximate Global Scaling Factors for TPSS, M06, and M11 Functional Families Using Several Common Basis Sets. *Journal of Physical Chemistry. A* 2017, 121 (11), 2265– 2273

(46)Straßner, A.; Wiehn, C.; Klein, M. P.; Fries, D. V.; Dillinger, S.; Mohrbach, J.; Prosenc, M. H.; Armentrout, P. B.; Gereon Niedner-Schatteburg. Cryo Spectroscopy of N2 on Cationic Iron Clusters. *The Journal of Chemical Physics* 2021, 155 (24).

(47)Weigend, F.; Ahlrichs, R. Balanced Basis Sets of Split Valence, Triple Zeta Valence and Quadruple Zeta Valence Quality for H to Rn: Design and Assessment of Accuracy. *Phys. Chem. Chem. Phys.* 2005, 7 (18), 3297

(48) Pollak, P.; Florian Weigend. Segmented Contracted Error-Consistent Basis Sets of Double- and Triple-ζ Valence Quality for One- and Two-Component Relativistic All-Electron Calculations. *Journal of Chemical Theory and Computation* 2017, 13 (8), 3696–3705

(49) Reiher, M. Douglas–Kroll–Hess Theory: A Relativistic Electrons-Only Theory for Chemistry. *Theoretical Chemistry Accounts* 2006, 116 (1-3), 241–252.

(50)Lu, T. A Comprehensive Electron Wavefunction Analysis Toolbox for Chemists, Multiwfn. *The Journal of Chemical Physics* 2024, 161 (8).

(51)Lu, T.; Chen, F. Multiwfn: A Multifunctional Wavefunction Analyzer. *J. Comput. Chem.* 2011, 33 (5), 580–592.

(52) Dolg, M.; Cao, X. Relativistic Pseudopotentials: Their Development and Scope of Applications. *Chemical Reviews* 2011, 112 (1), 403–480.

(53) Wang, M.; He, X.; Taylor, M.; Lorpaiboon, W.; Mun, H.; Ho, J. Molecular Geometries and Vibrational Contributions to Reaction Thermochemistry Are Surprisingly Insensitive to the Choice of Basis Sets. *Journal of Chemical Theory and Computation* 2023, 19 (15), 5036‑5046.

(54) Sharma, S. K.; Behm, T.; Köhler, T.; Beyer, J.; Gloaguen, R.; Heitmann, J. Library of UV-Visible Absorption Spectra of Rare Earth Orthophosphates, LnPO4 (Ln = La-Lu, except Pm). *Crystals* 2020, 10 (7), 593.

(55) Nerambourg, N.; Werts, N.; Charlot, M.; Blanchard-Desce, M. Quenching of Molecular Fluorescence on the Surface of Monolayer-Protected Gold Nanoparticles Investigated Using Place Exchange Equilibria. *Langmuir* 2007, 23 (10), 5563–5570.

(56)Hildebrandt, P.; Stockburger, M. Surface-Enhanced Resonance Raman Spectroscopy of Rhodamine 6G Adsorbed on Colloidal Silver. *The Journal of Physical Chemistry* 1984, 88 (24), 5935–5944.

(57)Polavarapu, P. L. Ab Initio Vibrational Raman and Raman Optical Activity Spectra. *The Journal of Physical Chemistry* 1990, 94 (21), 8106–8112.

(58)Ahuja, T.; Chaudhari, K.; Paramasivam, G.; Ragupathy, G.; Mohanty, J. S.; Pradeep, T. Toward Vibrational Tomography of Citrate on Dynamically Changing Individual Silver Nanoparticles. *J. Phys. Chem. C* 2021, 125 (6), 3553– 3566

(59)Leonard, J.; Haddad, A.; Green, O.; Birke, R. L.; Kubic, T.; Kocak, A.; Lombardi,

J. R. SERS , Raman , and DFT Analyses of Fentanyl and Carfentanil: Toward Detection of Trace Samples. *Journal of Raman Spectroscopy* 2017, 48 (10), 1323–1329.

(60)Udagawa, Y.; Mikami, N.; Kaya, K.; Ito, M. Absolute Intensity Ratios of Raman Lines of Benzene and Ethylene Derivatives with 5145 Å and 3371 Å Excitation. *Journal of Raman Spectroscopy* 1973, 1 (4), 341–346.

(61)Albrecht, A. C.; Hutley, M. C. On the Dependence of Vibrational Raman Intensity on the Wavelength of Incident Light. *Journal of Chemical Physics* 1971, 55 (9), 4438–4443.

(62) Krukowski, S.; Karasiewicz, M.; Kolodziejski, W. Convenient UV-Spectrophotometric Determination of Citrates in Aqueous Solutions with Applications in the Pharmaceutical Analysis of Oral Electrolyte Formulations. *Journal of Food and Drug Analysis* 2017, 25 (3), 717–722.

Chapter 5: General Conclusions and Future Perspectives

5.1 Summary of main findings

Initial SERS measurement was conducted on La^{3+} and Gd^{3+} ions with spin differences. The results represent the first demonstration of SERS-based discrimination between La^{3+} and Gd^{3+}, and provides the foundation for developing a SERS-based classification strategy for Ln^{3+} ions. A stable SERS measurement method was established using citrate capped silver nanoparticles (citrate@AgNPs) to measure La- and Gd-citrate complexes. Although the SERS peak positions were similar, La-citrate and Gd-citrate exhibited clearly different relative SERS intensities around 1065,1315 and 1495 cm^{-1}. Via DFT simulations, these differences were attributed to vibrational modes from the coordination region. The peak intensity ratio I_{1065}/I_{1315} was approximately 1 for La^{3+} and 0.55 for Gd^{3+}, enabling qualitative classification of these two ions.

The application of this new SERS measurement method to other Ln^{3+} ions provides key spectral indicators and mechanistic insights for future SERS-based classification of Ln^{3+} ions. The SERS spectra of seven Ln-citrate complexes (La, Ce, Pr, Nd, Sm, Eu, Gd) were systematically measured under three excitation wavelengths (488, 532, and 660 nm). All complexes showed consistent peak positions near 1065, 1315, and 1485 cm^{-1}. While the peak positions were excitation-independent, the relative intensities varied with the type of Ln^{3+} ion. DFT simulations using large-core pseudopotentials enabled detailed peak assignment. A clear trend was found: except for Ce^{3+} and Gd^{3+}, both I_{1065}/I_{1315} and I_{1485}/I_{1315} decreased with increasing number of unpaired 4f electrons, that is similar to the pattern of lanthanide contraction.

5.2 Scientific contributions

The main contributions of this thesis are summarized as follows: (i) A reproducible SERS measurement platform was developed for detecting lanthanide-citrate complexes using citrate@AgNPs. (ii) A new approach for classifying La^{3+} and Gd^{3+} ions was demonstrated based on their distinct SERS intensity ratios. (iii) The SERS spectra of seven Ln^{3+} ions (Ln=La, Ce, Pr, Nd, Sm, Eu, and Gd) were systematically investigated, revealing that peak ratios (I_{1065}/I_{1315} and I_{1485}/I_{1315}) correlate with 4f electron configurations and show lanthanide contraction-like trends. (iv) A DFT-based method using large-core pseudopotentials was constructed to simulate SERS spectra and assist in vibrational peak assignment.

These findings together advance the understanding of how 4f electronic configurations of lanthanides influence their SERS behavior and provide methodological tools for future studies.

5.3 Outlook for future research

This research lays a foundation for further development of SERS -based techniques for lanthanide analysis. Future directions include: (i) Expanding SERS studies to other Ln^{3+} ions (e.g., Tm^{3+}, Er^{3+}, Dy^{3+}) to establish possible classification models based on peak ratios and spectral trends. (ii) Investigating resonance Raman or SERRS effects, such as Ce^{3+} and Nd^{3+} complexes, to explore enhancement mechanisms. (iii) Applying the developed methods to actinide elements and other 4f/5f systems to explore their physicochemical properties.

Appendix: Magnetic Response Detection of La^{3+} and Gd^{3+} via NV-centers

A-1 Chapter overview

Lanthanide (Ln) elements have unique optical and magnetic properties that arise from their special 4f electronic configuration[1]. For +3 oxidation state Ln^{3+} ions, the electronic configuration is described as $[Xe]4f^n$ (n = 0-14)[1]. Differences in the number of unpaired electrons in the 4f orbital lead to variations in the spin and orbital energy levels among different Ln^{3+} ions, resulting in distinct optical and magnetic properties[1]. In addition, the 4f orbitals are located between the nucleus and the outer electrons and are shielded by the 5s and 5p orbitals. This shielding makes the 4f electrons relatively localized and less involved in chemical bonding, which causes Ln elements to have very similar chemical properties and makes them difficult to separate[1]. Although ultraviolet-visible-visible (UV-Vis) absorption spectroscopy [2], fluorescence spectroscopy [3], and electron paramagnetic resonance (ESR) [4] can distinguish different Ln^{3+} ions based on their optical or magnetic differences, there is a requirement for the development of more sensitive methods to study individual Ln^{3+} ions as Ln-molecule complexes are used in applications such as single-molecule magnets[5] and quantum computing[6].

The nitrogen-vacancy (NV) center is a point defect in a diamond composed of a carbon vacancy and a neighboring nitrogen atom. One creation method[7] of NV-center is shown in Figure A.1(a), a (100)-oriented type IIa bulk diamond sample grown by chemical vapor deposition (CVD) was implanted with $^{14}N^+$ ions at a dose of 1.0×10^{12} /cm^2 using an incident energy of 30 keV, followed by annealing at 900 °C for 1 h. Subsequently, the sample was cleaned and oxidized in a solution of a mixture of HNO_3:H_2SO_4 = 1 (10 ml):3 (30 ml) at 220 °C for 30 min. The Schematic of a NV-center

in diamond[8] is shown in Figure 5.1(b). NV-centers can exist in three distinct charge states[9]: negatively charged (NV^-), neutral (NV^0), and positively charged (NV^+). Among these, only the NV^- state exhibits magneto-optical activity, making it the primary focus of nearly all experimental investigations. In contrast, both NV^0 and NV^+ lack spin-dependent optical transitions and are not magneto-optically active.

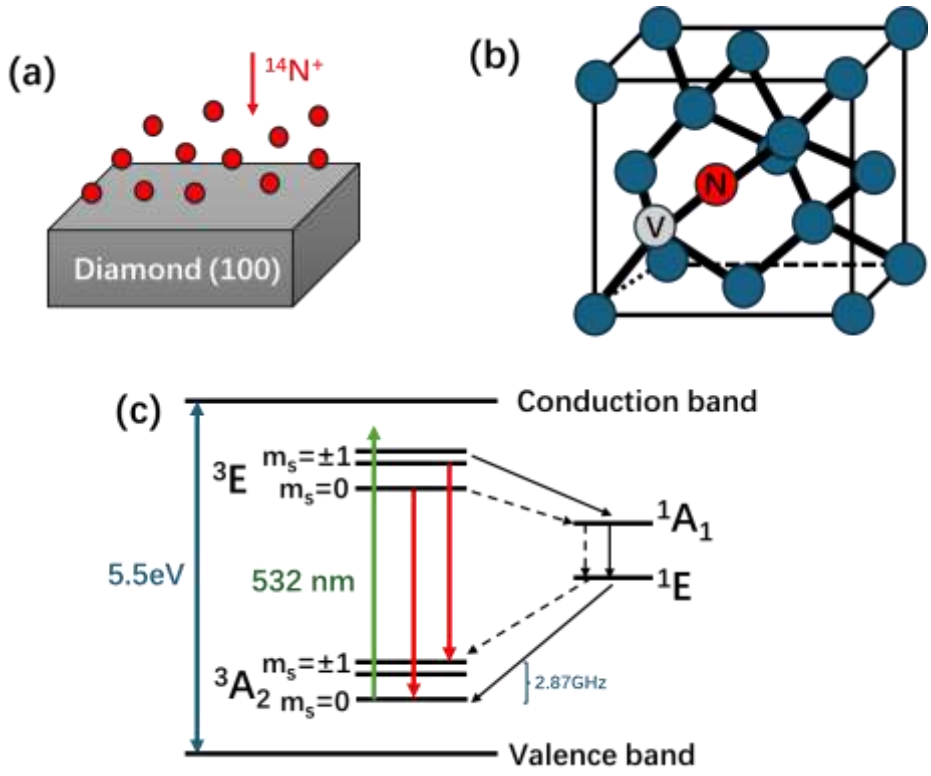

Figure A.1. (a) Schematic of the fabrication process of the NV-center; (b) Schematic of a NV-center in diamond; (c) Electronic energy level structure of the NV-center.

According to ref 9, the NV-center exhibits magneto-optically active that can be explained by its electronic structures (Figure A.1 (c)), which include a ground state of symmetry $^3A_2$, an excited state of symmetry ^3E, and a metastable singlet state composed of $^1A_1$ and ^1E levels. Both ground and excited states are spin triplet (S=1), each split into three spin sub-levels. Due to the NV-center's axial symmetry, the ms=±1 states are degenerate and energetically higher than the ms=0 states. The zero-field splitting between these sub-levels is D=2.87 GHz in the ground state and D=1.42 GHz in the excited state. Optical transitions between the triplet states are spin-conserving and

predominantly occur via a zero phonon line at 638 nm, although most of the photoluminescence (PL) signal is emitted in phonon sidebands between 630-800 nm. The NV-center can be efficiently excited by laser wavelengths below 640 nm and emits stable fluorescence at room temperature. In addition, the application of NV-center in magnetic sensing arises from the magnetic-field-induced lifting of the degeneracy between the m_s=0 and m_s=±1 spin sub-levels, which causes the m_s =±1 levels to shift in opposite directions. The transition rate between these spin sublevels is characterized by the spin-lattice relaxation time T_1

The spin-dependent optical transitions enable optically detected magnetic resonance (ODMR), where sweeping a microwave field across the ESR resonance causes transitions between m_s =0 and m_s=±1, resulting in a measurable drop in PL intensity[9]. This property makes the NV-center a powerful tool for quantum sensing. Its sensitivity to external magnetic and electric fields, as well as temperature, allows for high-resolution environmental sensing at the nanoscale.

Therefore, the NV-center is widely used for environmental sensing and imaging at the nanoscale. For some Ln^{3+} ions, such as La^{3+} (with the electronic configuration $[Xe]4f^0$, spin=0) and Gd^{3+} (with the electronic configuration $[Xe]4f^7$, spin=7/2), there is no visible fluorescence signal, but their spin differences are significant. Thus, the NV-center is an ideal platform to study the effect of spin differences of these Ln^{3+} ions on physical parameters like the T_1 relaxation time.

In this study, we used a lab-made ODMR instrument to measure the T_1 time of diamond surfaces that were partially covered with La-citrate and Gd-citrate. Our goal was to explore how the spin differences of these Ln^{3+} ions affect the T_1 time. Additionally, this work will also provide useful insights for using NV-centers to study the physical properties of other Ln^{3+} ions.

A-2 Experimental setup

Sample preparation

La_2O_3 and Gd_2O_3 (purity > 99%, Fujifilm Wako, Japan) were dissolved in 0.1 M HNO_3 (Fujifilm Wako, Japan) to prepare 0.1 M $Ln(NO_3)_3$ solutions. A 0.1 M sodium citrate solution was prepared by dissolving anhydrous sodium citrate (Fujifilm Wako, Japan) in ultrapure water. Equal volumes of the sodium citrate and $Ln(NO_3)_3$ solutions were mixed to form a 0.1 M Ln-citrate suspension with the pH around 7. A small amount of the Ln-citrate suspension was dropped onto a diamond surface covered with a carbon mesh. After heating and drying, parts of the diamond surface were covered with Ln-citrate. Finally, 1.38 g/mL HNO_3 (Kanto Chemical, Japan) was used to clean the Ln-citrate from the diamond surface.

Experiment

Pre-experiment: A lab-made ODMR instrument[10] was used to measure the diamond's PL image and ODMR spectrum. The power of microwave amplification was 35 dBm, and a 532 nm laser was used, with the power adjusted as needed.

Main experiment: Another lab-made ODMR instrument[10] was used to measure the T_1 time of diamond areas with and without Gd-citrate or La-citrate coverage. The power of microwave amplification was 36 dBm, and a 532 nm laser was used, with the power adjusted as needed.

A-3 Data analysis and results discussion

A-3.1 Optimization of T_1 measurement parameters

To optimize the T_1 measurement conditions, three parameter sets were tested at the same position. The tested conditions were: (a) 1 ms sweep time, 21 points, 32 averages; (b) 5 ms sweep time, 30 points, 100 averages; and (c) 5 ms sweep time, 50 points, 150 averages. The results are shown in Figure A.2. In Figures A.2(a)-(c), raw T_1 data (black lines) and the corresponding fitted curves (red lines) are displayed. Among the three

settings, the third condition produced the best fit. Figure A.2(d) compares all fitted curves, showing that the third parameter setting provides the most reliable T_1 estimation.

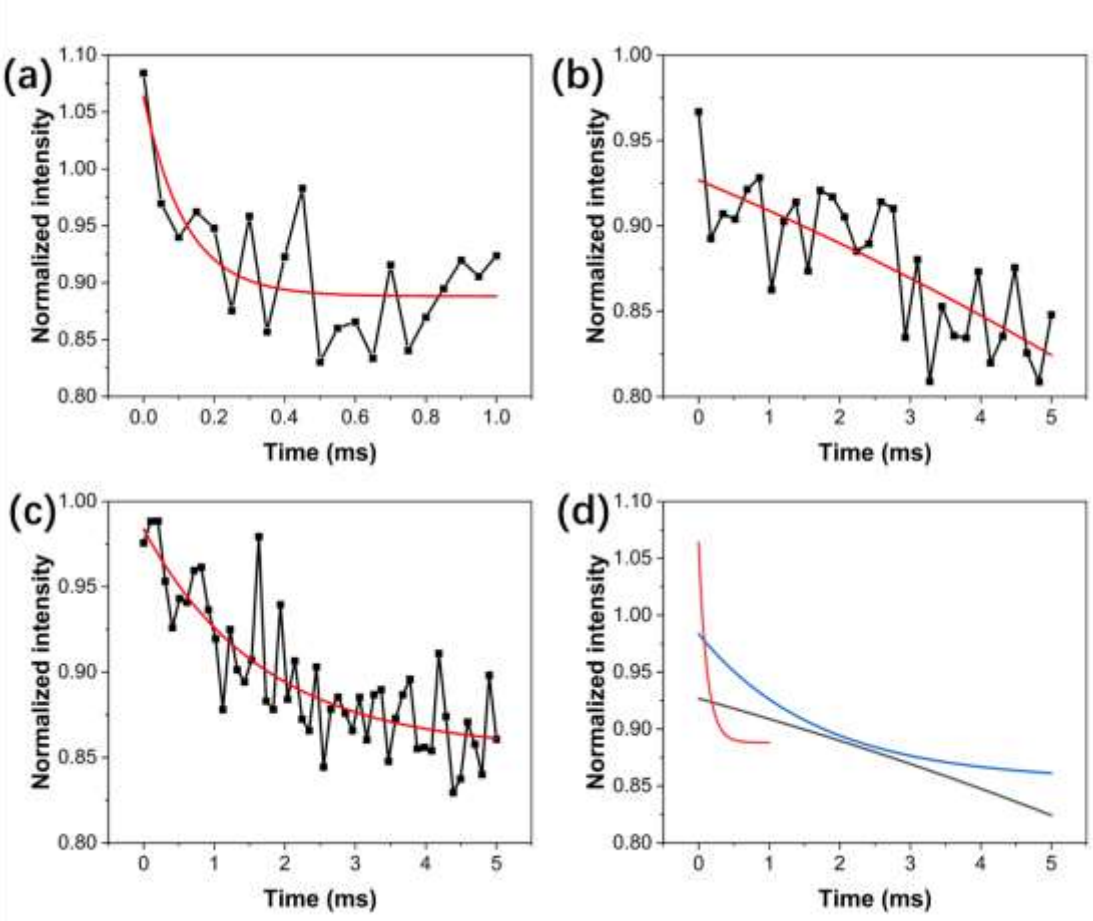

Figure A.2. T_1 measurements of diamond:(a) T_1 measurement result (black line) and its fitting curve (red line) at the measurement point (sweep time: 1 ms, 21 sweep points, averaged 32 times); (b) T_1 measurement result and fitting curve at the same measurement point (sweep time: 5 ms, 30 sweep points, averaged 100 times); (c) T_1 measurement result and fitting curve at the same measurement point (sweep time: 5 ms, 50 sweep points, averaged 150 times); (d) Comparison of T_1 times for the three measurements (first: red line, second: black line, third: blue line).

A-3.2 T_1 measurement

The method for preparing Ln-citrate covered diamond samples is illustrated in Figure A.3(a). A carbon mesh was fixed on the front side using tape, and Ln-citrate suspension was dropped onto the mesh. After drying, the mesh was removed, and the diamond was placed upside down on the Au wire for measurement. The suspension may contain $Gd(OH)_3$ precipitates, citrate ions, Na^+, $NO3^-$, and Ln^{3+} ions. The difference in

signal responses originates primarily from the magnetic and electric properties of the Ln^{3+} ions.

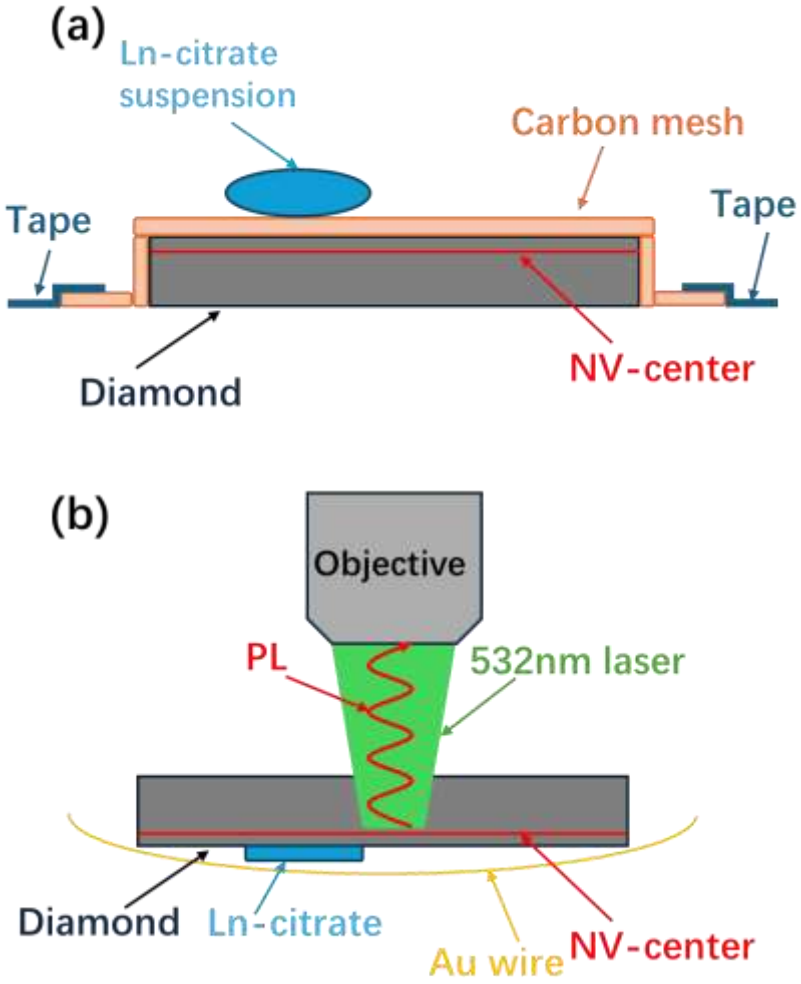

Figure A.3. (a) Schematic diagram of sample preparation; (b) Fixed measurement sample.

A direct comparison of T1 curves between Gd-citrate covered and uncovered regions is shown in Figure A.4(a). The solid line (covered) shows significantly faster decay than the dashed line (uncovered). The presence of Gd^{3+} ions with 7 unpaired 4f electrons creates magnetic field fluctuations, enhancing NV spin relaxation. Figure A.4(b) compares the average T1 times: 0.151 ms for the covered area and 2.367 ms for the uncovered area, a 15.7-fold reduction.

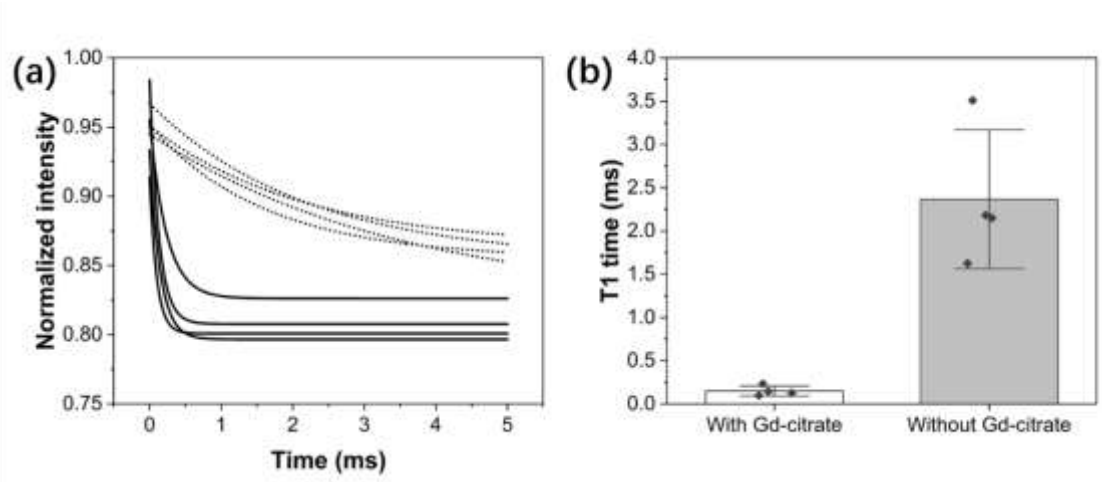

Figure A.4. (a) Comparison of the T_1 fitting curves of measurement areas with Gd-citrate (solid line) and without Gd-citrate (dashed line); (b) Comparison of the T_1 times between measurement areas with Gd-citrate and without Gd-citrate (error bars represent ±SD).

After cleaning the diamond with concentrated HNO3 (1.38 g/mL), the surface was confirmed to be clean. A La-citrate suspension was then applied and dried. T_1 measurements from three La-citrate-covered points and three La-citrate-uncovered points, respectively.

In Figure A.5(a), T_1 curves of La-citrate covered (solid line) and uncovered (dashed line) areas are compared. Both show slow decay. Figure A.5(b) shows the average T_1 times: 2.688 ms (covered) and 4.096 ms (uncovered), indicating a around 1.52-fold reduction due to local electric field effects, as La^{3+} has no unpaired electrons and thus weak magnetic influence. These results suggest the La-citrate layer slightly affects NV relaxation behavior. The decay may be influenced by changes in surface charge, local electric field, or distance from the Au wire.

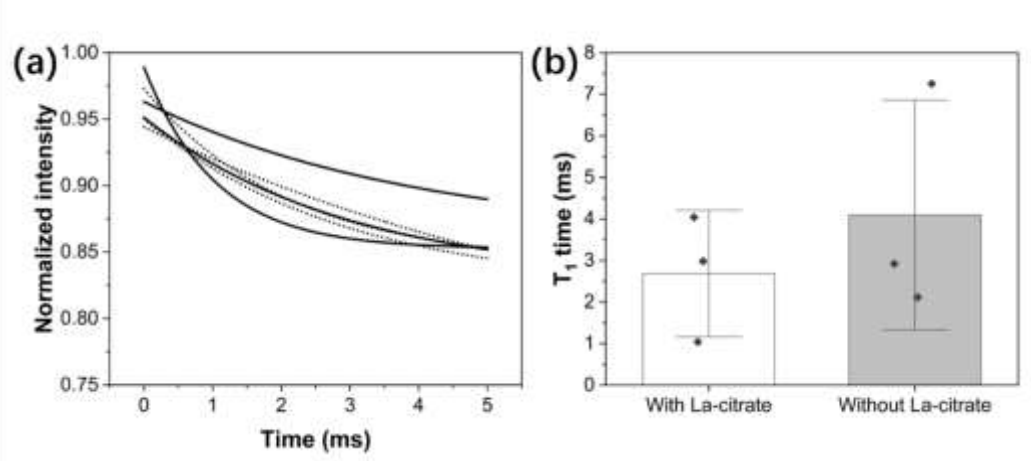

Figure A.5. (a) Comparison of the T_1 fitting curves of measurement areas with La-citrate (solid line) and without La-citrate (dashed line); (b) Comparison of the T_1 times between measurement areas with La-citrate and without La-citrate (error bars represent ±SD).

These experiments demonstrate that NV-center T_1 relaxation time is sensitive to the spin state of nearby ions and provide a potential method for distinguishing magnetic and non-magnetic lanthanide species using diamond-based quantum sensors.

A-4 Summary

In this study, we successfully demonstrated the measurement of Gd^{3+} and La^{3+} ions using NV-center-containing diamonds by measuring the T_1 relaxation time. The T_1 relaxation time was obtained by monitoring changes in PL intensity of NV-centers after a spin initialization and microwave manipulation sequence. As T_1 reflects the rate at which NV-center electron spins relax from the excited state to the ground state, its measurement provides a sensitive probe of the local magnetic environment. Notably, the T_1 signal is derived from variations in PL intensity of the NV-center, which can also be influenced by external magnetic fields, electric fields, and surface charge effects.

To reduce interference from the surface-bound lanthanide-citrate (Ln-citrate) layer, we conducted backside measurements through the diamond substrate. The Gd-citrate-covered regions exhibited significantly shortened T_1 times compared to uncovered regions, due to the magnetic fluctuations generated by Gd^{3+} ions, which possess 7-

unpaired 4f electrons. These fluctuations enhance spin relaxation and accelerate the decay of T_1. In contrast, La-citrate-covered regions showed only a minor decrease in T_1, consistent with the non-magnetic nature of La^{3+} ions, which lack unpaired electrons and primarily affect the local electric field near the NV-centers.

These findings confirm that differences in T_1 relaxation behavior correlate with the spin states of Ln^{3+} ions. Furthermore, while concentrated nitric acid (1.38 g/mL HNO_3) can remove surface Ln-citrate layers, this process may alter the diamond's surface chemical environment and affect local electric and magnetic fields, thereby impacting the NV-center's PL signal. Variations in measurement location, including proximity to conductive structures such as gold wires, may also contribute to signal changes. This work also provides a valuable reference for future studies using NV-centers to investigate other Ln^{3+} ions.

A-5 References

(1) Simon Cotton. *Lanthanide and Actinide Chemistry*; John Wiley & Sons, Ltd, 2006; pp 9-33.

(2) Sharma, S. K.; Behm, T.; Köhler, T.; Beyer, J.; Gloaguen, R.; Heitmann, J. Library of UV-Visible Absorption Spectra of Rare Earth Orthophosphates, LnPO4 (Ln = La-Lu, except Pm). *Crystals* 2020, 10 (7), 593.

(3) Wang, G.; Peng, Q.; Li, Y. Lanthanide-Doped Nanocrystals: Synthesis, Optical-Magnetic Properties, and Applications. *Accounts of Chemical Research* 2011, 44 (5), 322-332.

(4) Baggio, R.; Calvo, R.; María Teresa Garland; O. Peña; Perec, M.; Alberto Claudio Rizzi. Gadolinium and neodymium citrates: Evidence for weak ferromagnetic exchange between gadolinium (III) cations. *Inorganic chemistry* 2005, 44 (24), 8979-8987.

(5) Martínez-Pérez, M. J.; Cardona-Serra, S.; Schlegel, C.; Moro, F.; Alonso, P. J.;

Prima-García, H.; Clemente-Juan, J. M.; Evangelisti, M.; Gaita-Ariño, A.; Sesé, J. et al. Gd-Based Single-Ion Magnets with Tunable Magnetic Anisotropy: Molecular Design of Spin Qubits. *Physical Review Letters* 2012, 108 (24), 247213.

(6) Serrano, D.; Kuppusamy, S. K.; Heinrich, B.; Fuhr, O.; Hunger, D.; Ruben, M.; Goldner, P. Ultra-Narrow Optical Linewidths in Rare-Earth Molecular Crystals. *Nature* 2022, 603 (7900), 241-246.

(7) Kainuma, Yuta, Hayashi K, Tachioka C, et al. Scanning diamond NV-center magnetometer probe fabricated by laser cutting and focused ion beam milling. *Journal of Applied Physics* 2021, 130(24), 243903.

(8) Ishii S, Saiki S, Onoda S, et al. Ensemble negatively-charged nitrogen-vacancy centers in type-Ib diamond created by high fluence electron beam irradiation. *Quantum Beam Science* 2021, 6(1): 2.

(9) Schirhagl, Romana, et al. Nitrogen-vacancy centers in diamond: nanoscale sensors for physics and biology. *Annual review of physical chemistry* 2014, 65(1), 83-105.

(10) Prananto, Dwi, et al. Probing thermal magnon current mediated by coherent magnon via nitrogen-vacancy centers in diamond. *Physical Review Applied* 2021, 16(6), 064058.

Acknowledgement

I would like to express my sincere gratitude to Associate Professor Yuko S. Yamamoto at JAIST for her guidance throughout my doctoral studies, her support for my independent research interests, and her valuable assistance in my academic development.

I am deeply grateful to Professor Tamitake Itoh at AIST for his insightful guidance, generous research support, and continuous encouragement during the course of my research.

My thanks also go to Professor Emeritus Yukihiro Ozaki at Kwansei Gakuin University for his valuable academic advice and guidance.

I would like to thank Associate Professor Toshu An at JAIST for his support and supervision of my sub-research project, as well as all members of the An laboratory for their assistance with experiments.

In addition, I sincerely thank Professor Emeritus Goro Mizutani, Associate Professor Jumpei Ueda and Professor Yukiko Yamada-Takamura at JAIST for their kind support both in research and in daily life.

Finally, I would like to express my heartfelt appreciation to the JAIST staff, fellow students, and faculty members from other courses for their assistance and support throughout my doctoral program. I am also deeply grateful to my family for their unwavering encouragement and support.

List of achievements

Publications

Published Article:

1. **Hao Jin**, Tamitake Itoh, Yuko S. Yamamoto, “Classification of La^{3+} and Gd^{3+} Rare-Earth Ions Using Surface-Enhanced Raman Scattering“, *The Journal of Physical Chemistry C,* **2024,** 128 (13), 5611–5620.

To be published:

1. **Hao Jin**, Tamitake Itoh, Yuko S. Yamamoto, “Surface-enhanced Raman scattering and DFT study of selected lanthanide-citrate complexes (lanthanide: La, Ce, Pr, Nd, Sm, Eu, and Gd)”, to be published.

Presentations

International conferences:

1. Poster presentation

Hao Jin, Tamitake Itoh, Yuko S. Yamamoto, "Surface-enhanced Raman Scattering and DFT study of 7 lanthanide-citrate complexes (lanthanide: $_{57}$La, $_{58}$Ce, $_{59}$Pr, $_{60}$Nd, $_{62}$Sm, $_{63}$Eu, and $_{64}$Gd)", *The 11th International Conference on Surface Plasmon Photonics (SPP11).* May 22, **2025**, Tokyo, Japan.

2. Oral presentation

Hao Jin, Tamitake Itoh, Yuko S. Yamamoto, "SERS and DFT study of rare earth-citrate complexes ", *XXVIII International Conference on Raman Spectroscopy (ICORS2024)*. July 28, **2024**, Rome, Italy.

3. Oral presentation

Hao Jin, Tamitake Itoh, Yuko S. Yamamoto, "Rare earth-citrate complexes study using

surface-enhanced Raman scattering spectra",*12th International Conference on Advanced Vibrational Spectroscopy (ICAVS12).* August 28, **2023**, Krakow, Poland.

4. Oral presentation

Hao Jin, Tamitake Itoh, Yuko S. Yamamoto, "SERS and DFT investigation of rare earth ions-citrate complexes on silver colloids", *The 13th Asia-Pacific Conference on Near-Field Optics (APNFO13)*. July 31, **2022**, Sapporo, Japan.

Domestic conferences:

1. Invited oral presentation

Hao Jin, Tamitake Itoh, Yuko S. Yamamoto, "Surface-enhanced Raman spectroscopic study of 7 lanthanide–citrate complexes", *The 6th Youth Academic Conference of the Chinese Society of Rare Earths*. May 11, **2025**, Changsha, China.

2. Oral presentation

Hao Jin, Akito Fukuoka, Syunsuke Uesugi, Yifei Wang, Dwi Prananto, Yuko S. Yamamoto, Toshu An, "Characterization of T_1 Relaxation time and optically detected magnetic resonance spectra of non-fluorescent lanthanide ions based on nitrogen-vacancy centers", *The 6th Youth Academic Conference of the Chinese Society of Rare Earths*. May 11, **2025**, Changsha, China.

3. Oral presentation

Hao Jin, Tamitake Itoh, Yuko S. Yamamoto, "Surface-Enhanced Raman Scattering for the Detection and Classification of Rare Earth Ions", *2024 Academic Annual Conference of the Chinese Rare Earth Society*. October 26, **2024**, Chengdu, China

4. Poster presentation

Hao Jin, Tamitake Itoh, Yuko S. Yamamoto, "Spin related bands in Surface-enhanced Raman Scattering spectra for the classification of rare earth ions", *The 70th Japan Society of Applied Physics Spring Meeting 2023*. March 15, **2023**, Tokyo, Japan.

5. Poster presentation

Hao Jin, Tamitake Itoh, Yuko S. Yamamoto, “Ion monitoring and effect study of rare earth elements using SERS analysis", *The 69th Japan Society of Applied Physics Spring Meeting 2022*. March 22, **2022**, Tokyo, Japan.